Universitá degli Studi di Padova

Dipartimento di Ingegneria Civile,
Edile ed Ambientale

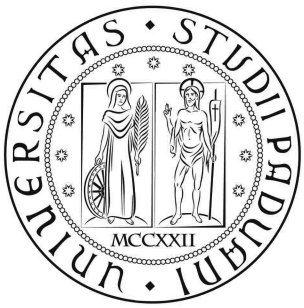

Tesi di Laurea

Numerical and Experimental Evaluation of Drag Force on Coupled Fish

Relatore: Prof. Andrea MARION

Laureando: Riccardo Callegarin

Anno Accademico 2014-2015

A tutti coloro che mi sono stati vicini in questi anni di studio,
ma in particolare a mamma e papá, grazie ai quali tutto é stato possibile,
e a Sara, che piú di tutti mi ha dato forza in questi anni di avventura
universitaria.

Abstract

Experiments highlighted that couples of minnows (*Phoxinus phoxinus*) have different behavior in quiescent and fast moving water. Fish do not show any particular pattern in standing water, while they tend to arrange in a side-by-side school when subjected to the flow. This leads to the idea that they experience a hydrodynamical benefit under these school condition.

Hence, the present work studies hydrodynamical effects of proximity on fish paired in a side-by-side pattern. In order to do this, numerical simulations and laboratory experiments were done.

Results showed that fish swimming in close proximity experience an increment of forces acting on them. Furthermore, the length of fish wake and the flow turbulence near the school increase too with the reduction of the distance among animals. No evidences of a hydrodynamic benefit arising from the proximity were found.

Instead, analyzing simulations results, the idea that fish take that school pattern in order to overcome a lack of information on the surrounding was introduced.

Contents

List of Figures

List of Tables

Introduction

Fish behavior is a complex and fascinating research topic that has inspired many scientists for decades. In particular the collective behavior emerging from fish schools has attracted the attention of biologist and physicists for the wide range of implications in science and engineering. These are:

- To enhance robotic fish swarm technology for applications in coastal defense, detection of oil spills as well as chemical and biological tracers;
- To identify bio-inspired configurations of groups of foils responding to engineering tasks such that of drag reduction;
- To improve fish' migration in proximity of hydraulic barriers in riverine systems such as weirs and hydropower plants.

The present work addresses the research question "*Is the collective behavior dictated by hydrodynamic strategies?*". The literature on the subject is rich but reports contradictory results [9, 18]. *Weish, D.* (1973) [30] started from the hypothesis that a very large school appears boundless to a fish swimming inside. He discussed how rear-lines fish could get an hydraulic benefit by synchronizing their swim with front fish in a well-defined two-dimensional diamond-shape school pattern. According to this study, hydromechanical factors can play an important role in schools behavior. That being said, the fixed distance diamond-shape pattern has been shown to occur seldom in nature [24].
Partridge and Pitcher (1979) [24] studied real schools in a circular basin in order to verify Weish's theory, but they did not observe any of the theoretical predictions listed within Weish's work, such as the phase swimming of neighboring fish or the shape of their pattern.

A more recent work by *Hemelrijk et al.* (2014)[13], investigated hydrodynamic interactions among schooling fish through a numerical model incorporating waves interacting behind individual fish. They investigated a wide range of potential swimming patterns and identified the optimal configuration that maximizes the efficiency of fish swimming.
Hemelrijk et al. (2014) [13] underlines also the need to define a general theory describing whether only the proximity among fishes, or their distribution pattern induces an energetic benefit.
In this context, the present work studies numerically how the proximity influences drag forces experienced by fishes in a shoal of two elements arranged in a side by side configuration. The distance between simulated fish is the variable of the work. The range of distances comes from a previous experimental research on couples of minnows (*Phoxinus phoxinus*) which highlighted a difference in fish behavior between two extreme conditions of quiescent and fast moving water. In particular, in standing water fish do not show preferential swimming configuration, whereas, in moving water, they tend to adjust themselves side by side at a distance of 0.3 body lengths.
Numerical simulations were carried out utilizing ANSYS® Fluent, a commercial software capable to simulate flows in both turbulent and laminar flow conditions. For the present work, the *Realizable* k-ϵ model, based on *RANS* equations, was used. Fish bodies were reproduced in the numerical simulations as slender bodies resembling wing section profiles.
Numerical simulations results need to be validated comparing them to laboratory experiments results. These experiments were made with a magnified version of fish in order to make drag forces bigger than other forces acting on the structure. However, unwonted changes in the experimental set-up influenced results.
The hypothesis behind the present work is that fish change their behavior and take a side by side configuration in moving water according to a hydrodynamic benefit they may experience. Hence, the aim of the work is to verify the presence of this benefit.
To fulfill this aim, the following objectives are identified:

- To identify the best model to investigate drag coefficients of slender bodies in a side by side configuration;

- To analyze the drag coefficient of fish variations for different distances between specimens through numerical simulation;
- To investigate wake properties of fish-couples to support the interpretation of results on drag coefficients;
- To validate numerical results with experimental evidences;
- To discuss the results in view of disentangling long standing questions concerning hydrodynamic benefit strategies in fish schools.

Chapter 1

Theoretical background

1.1 Governing equations

1.1.1 Navier-Stokes equations

Fluid dynamic problems can be theoretically solved analysing the coupled system of momentum and mass-conservation equations. As long as the problem considers an incompressible fluid, such as water in standard conditions, the continuity equation can be simplified to the kinematic condition where the velocity field is *divergence-free*. This equates to the fact that the control volume is constantly composed of the same particles. The continuity equation can be written as:

$$\nabla \cdot \boldsymbol{U} = 0 \tag{1.1}$$

Where:

- $\boldsymbol{U}$ is the velocity vector;
- $\nabla \cdot \mathbf{A}$ is the divergence of the quantity $\boldsymbol{A}$. Being $\boldsymbol{U}$ a continuous differentiable vector, the result of the operation is a scalar, sum of the derivatives of the vector components taken on their direction, $\sum_{i=x,y,z} \frac{\partial \boldsymbol{U}_i}{\partial\ i}$.

On the other hand, the *momentum equation* which is based on Newton's second law, relates particles accelerations to surface and body forces. Following *Einstain summation convention*, the equation can be written as:

$$\rho \frac{D\boldsymbol{U_j}}{Dt} = \frac{\partial \boldsymbol{\tau_{ij}}}{\partial x_i} - \rho \frac{\partial \boldsymbol{\Psi}}{\partial x_j} \tag{1.2}$$

Where:

- $\boldsymbol{U_i}$ is the velocity vector component on the i direction;
- $\boldsymbol{\tau_{ij}}(\mathbf{x}, t)$ is the *stress tensor* component belonging to the (i, j) plane. Each component represents a surface force of molecular origin. The stress tensor is symmetric ($\boldsymbol{\tau_{ij}} = \boldsymbol{\tau_{ji}}$);
- ρ is the water density;
- $\boldsymbol{\Psi}$ is the gravitational potential representing body forces. Considering a constant gravitational acceleration, $\overrightarrow{g}$, and, z, the vertical coordinate, it can be written as $\boldsymbol{\Psi} = \overrightarrow{g}z$;
- $\frac{D}{Dt}$ is the *material derivative*, or *substantial derivative*, that is defined as:

$$\frac{D}{Dt} = \frac{\partial}{\partial t} + \boldsymbol{U_i}\frac{\partial}{\partial x_i}.$$

For *constant-property Newtonian fluid*, such as water, the stress tensor becomes:

$$\boldsymbol{\tau_{ij}} = -\boldsymbol{P}\delta_{ij} + \mu\left(\frac{\partial \boldsymbol{U_i}}{\partial x_j} + \frac{\partial \boldsymbol{U_j}}{\partial x_i}\right) \tag{1.3}$$

Where:

- $\boldsymbol{P}$ is the pressure;
- μ is the constant coefficient of *dynamic viscosity*. Water dynamic viscosity is 0,001003 $\left[\frac{kg}{m \cdot s}\right]$;
- δ_{ij} is the *Kronecker delta*, which is defined as:

$$\delta_{ij} = \begin{cases} 1 & if\ i = j \\ 0 & if\ i \neq j \end{cases}; \tag{1.4}$$

Accordingly, with the mass conservation equation (Eq. 1.1), the value of the second term on the right hand of the Eq. 1.3 is zero when $i = j$. Therefore, Eq. 1.3 is the sum of an isotropic ($-\boldsymbol{P}\delta_{ij}$) and a deviatoric anisotropic term.

Considering equations 1.1, 1.2 and 1.3 one obtains the *Navier-Stokes equations* as following:

$$\rho\frac{D\boldsymbol{U_j}}{Dt} = \mu\frac{\partial^2\boldsymbol{U_j}}{\partial x_i \partial x_i} - \frac{\partial \boldsymbol{P}}{\partial x_j} - \rho\frac{\partial \boldsymbol{\Psi}}{\partial x_j} \tag{1.5}$$

Which are valid for incompressible Newtonian fluids.

1.1.2 Reynolds Averaged Navier-Stokes equations

Reynolds [27] introduced the possibility to study Eq. 1.5 by decomposing the flow in a mean and a fluctuating component. This decomposition is called *Reynolds decomposition* (Eq. 1.6).

$$\boldsymbol{U}(X,t) = \langle \boldsymbol{U}(X) \rangle + \boldsymbol{u}(X,t) \tag{1.6}$$

Where:

- $\boldsymbol{U}(X,t)$ is the velocity vector at point X and time t;
- $\langle \boldsymbol{U}(X) \rangle$ is the mean velocity field, where the $\langle\ \rangle$ here is taken as time averaging.
- $\boldsymbol{u}(X,t)$ is the fluctuation around the mean.

The time averaging of vectors applied to the *Navier-Stokes* equations (Eq. 1.5) leads to:

$$\rho\frac{\overline{D}\langle\boldsymbol{U_j}\rangle}{\overline{D}t} = \mu\frac{\partial^2\langle\boldsymbol{U_j}\rangle}{\partial x_i \partial x_i} - \frac{\partial\langle \boldsymbol{p}\rangle}{\partial x_j} - \rho\frac{\partial\langle \boldsymbol{u_i u_j}\rangle}{\partial x_i} \tag{1.7}$$

These are the so-called *Reynolds Averaged Navier-Stokes equations* (i.e. *RANS* equations). Where:

- $\boldsymbol{p} = \boldsymbol{P} + \rho\boldsymbol{\Psi}$ is the modified pressure;
- $\langle \boldsymbol{u_i u_j}\rangle$ are called *Reynolds stresses*. $-\rho\langle \boldsymbol{u_i u_j}\rangle$ represent apparent stress arising from the fluctuating velocity field. Without their contribution, equations 1.5 and equations 1.7 would be identical;
- $\frac{\overline{D}}{\overline{D}t}$ is the *mean substantial derivative* that is defined as:

$$\frac{\overline{D}}{\overline{D}t} = \frac{\partial}{\partial t} + \langle \boldsymbol{U_i}\rangle\frac{\partial}{\partial x_i}.$$

A mathematical solution of equation 1.7 can be found by defining a closure for the Reynolds stress tensor.

As mentioned above, *Reynolds stresses* represent apparent stresses arising from the fluctuation velocity field. In particular, *Reynold stress* represents the average transfer of momentum through turbulence.

Reynold stresses can be arranged in a tensor matrix.

$$-\rho \cdot \langle \boldsymbol{u_i u_j}^2 \rangle = -\rho \cdot \begin{bmatrix} \langle \boldsymbol{u_1}^2 \rangle & \langle \boldsymbol{u_1 u_2} \rangle & \langle \boldsymbol{u_1 u_3} \rangle \\ \langle \boldsymbol{u_2 u_1} \rangle & \langle \boldsymbol{u_2}^2 \rangle & \langle \boldsymbol{u_2 u_3} \rangle \\ \langle \boldsymbol{u_3 u_1} \rangle & \langle \boldsymbol{u_3 u_2} \rangle & \langle \boldsymbol{u_3}^2 \rangle \end{bmatrix} \tag{1.8}$$

This is a second order symmetric tensor, where, as for the stress tensor in equation 1.3, terms of the Reynolds stress tensor can be divided in an *isotropic*, $(\frac{2}{3}k\delta_{ij})$, and an *anisotropic* component, $(a_{ij} = \langle \boldsymbol{u_i u_j} \rangle - \frac{2}{3}k\delta_{ij})$.

The *anisotropic* component represents an apparent shear stress arising from velocity fluctuations. According to the continuity equation the *anisotropic* component value is 0 when $i = j$.

The *isotropic* component instead represents apparent normal stresses arising from velocity fluctuations. This component value is 0 when $i \neq j$ thanks to Kronecker delta properties.

$$-\rho \langle \boldsymbol{u_i u_j} \rangle = 2\rho\nu_T \overline{S}_{ij} - \frac{2}{3}\rho k \delta_{ij} \tag{1.9}$$

where:

- $\overline{S}_{ij}$ is the mean rate of strain tensor,

$$\overline{S}_{ij} = \frac{1}{2}\left(\frac{\partial \langle \boldsymbol{U_i} \rangle}{\partial x_j} + \frac{\partial \langle \boldsymbol{U_j} \rangle}{\partial x_i} \right);$$

- ν_T is the *turbulent viscosity*, also called *eddy viscosity*. Its unit of measurement is L^2/T;

- k is the so-called *Turbulent kinetic energy*.

The turbulent kinetic energy is one of the most important parameter describing the flow turbulence, *k(X,t)* read:

$$k = \frac{1}{2}\langle \boldsymbol{u} \cdot \boldsymbol{u} \rangle \tag{1.10}$$

k(X,t) unit of measurement is $\frac{[L]^2}{[t]^2}$.

The turbulent kinetic energy is a measure of the flow turbulence. As it will be shown later, this parameter and its transport equation have been used by *Jones and Launder* (1972) [16]to define the k-ϵ model (Sec. 3.3).

1.1.3 The Boussinesq approximation

Boussinesq in 1877 introduced the so called *turbulent-viscosity hypothesis*. The idea behind the introduction of this hypothesis is that the transport of turbulence behave as a diffusion phenomenon. *Reynolds stresses* can be modeled with an additional turbulent viscosity analogue to molecular viscosity.

The turbulent viscosity has been already introduced in equation 1.9. Substituting this into *RANS* equations (Eq. 1.7) gives:

$$\frac{\overline{D}\langle \boldsymbol{U_j} \rangle}{\overline{D}t} = \frac{\partial}{\partial x_i}\left[\nu_{eff}\left(\frac{\langle \boldsymbol{U_i} \rangle}{\partial x_j} + \frac{\langle \boldsymbol{U_j} \rangle}{\partial x_i}\right)\right] - \frac{1}{\rho}\frac{\partial}{\partial x_j}\left(\langle p \rangle + \frac{2}{3}\rho k\right) \tag{1.11}$$

where ν_{eff} is the *effective viscosity* ($\nu_{eff}(X,t) = \nu + \nu_T$). This equation is the same as Eq. 1.5 with $\langle p \rangle + \frac{2}{3}\rho k$ the modified pressure, $\langle \mathbf{U} \rangle$ instead of $\boldsymbol{U}$ and ν_{eff} instead of ν.

The turbulent-viscosity hypothesis implies that the anisotropy tensor lies on the same direction of the mean rate of strain (- $\langle \boldsymbol{u_i u_j} \rangle + \frac{2}{3}k\delta_{ij} = a_{ij}\ \alpha\ S_{ij}$).

The mean rate of strain have five independent components that are related to the anisotropic part of the Reynolds tensor terms through the scalar coefficient $\nu_T(X,t)$. Hence, mean rate of strain and the anisotropic part of are aligned. However, this alignment does not occur even for simple shear flows. The knowledge of $\nu_T(X,t)$, which now is the only unknown of the problem, means that Eq. 1.11 can be solved.

The eddy viscosity, as the molecular viscosity, can be seen as proportional to appropriate length, L, and velocity, V, scales (or length and time scales).

$$\nu_T\ \alpha\ LV \tag{1.12}$$

Therefore, models based on the Boussinesq approximation use a number of ad-hoc equations to quantify ν_T.

1.2 Flow around obstacles

The literature is full of studies on vortex shedding over many types of obstacles for different value of *Re*. Flows around circular and square cylinders has been well studied because of their relevance for aerodynamic and hydrodynamic applications [29, 21]. Many studies have also been done for airfoils and wings [1]. Fewer studies have been done for airfoils at low *Re*.

Generally speaking, a body submerged in a fluid experiences forces arising from its relative motion and from the difference among pressure on its sides. Those forces are the *lift* force, F_L, and the *drag* force, F_D. Given a reference system and a flow with direction x, the drag force is the force experienced from the body in the same direction. The lift force instead is the force acting in the direction perpendicular to the flow. However, this condition defines a plane of possibilities. For the present work, the lift force is the force acting in the horizontal plane, hence, in the y direction.

The drag force can be seen as the integral of the x-component of shear and normal stresses on the body surface, (Eq. 1.13). The lift force is instead the integral of y-component of stresses, (Eq. 1.14).

$$F_D = \int dF_x = \int p\ cos\phi\ dS + \int \tau\ sin\phi\ dS \tag{1.13}$$

$$F_L = \int dF_y = \int p\ sin\phi\ dS + \int \tau\ cos\phi\ dS \tag{1.14}$$

Where:

- S is the body surface;
- ϕ is the angle subtended between the x-direction and the normal to the considered surface;
- p is the stress normal to the considered surface;
- τ is the shear stress.

Those forces can be also studied from a dimensionless point of view. The drag coefficient, C_D, and the lift coefficients, C_L, can be defined as:

$$C_D = \frac{F_D}{\frac{1}{2}U^2\rho A} \tag{1.15}$$

$$C_L = \frac{F_L}{\frac{1}{2}U^2\rho A} \tag{1.16}$$

The drag coefficient, C_d, has been shown to greatly vary with the Reynolds number (Fig. 1.1).

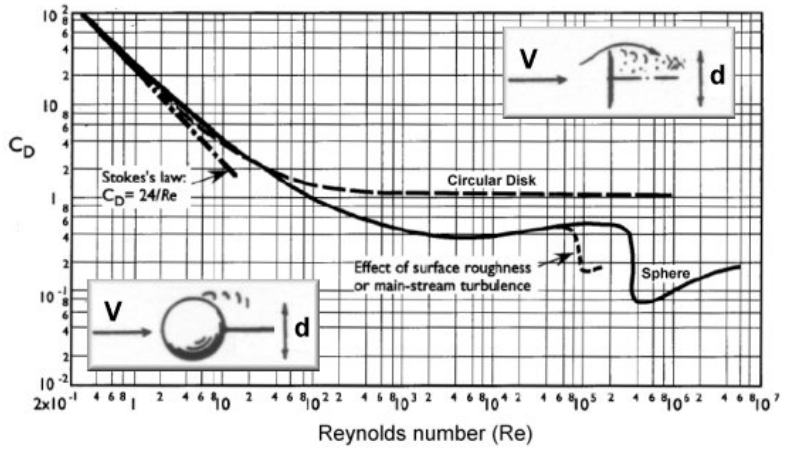

Figure 1.1: Variation of Drag coefficient versus changing of Reynolds number magnitude. (Figure taken from *Tritton, D.* (1988) [29].)

Another well studied effect on C_d of circular cylinders is the *proximity effect*. In fact, the presence of second cylinder either in a side-by-side or in a tandem configuration change forces acting on the reference one. The case of the side-by-side cylinders is of particular interest for the present study because fish, when subjected to the flow, took a side-by-side configuration (for more details see section 3.4.1). Hence, it is possible that the same interaction occurring among cylinders wakes occurs also to fish wakes. *Sumner* (2010) [28] provides a review of studies on vortex shedding among cylinders in different configurations. According to this work the flow field of multiple-cylinder configurations involve complex interactions between shear layers, vortices, and wakes. Sumner's work collects data and report them as a function of the distance between the center of mass of cylinders. This distance and other relevant parameters are named in figure 1.2.

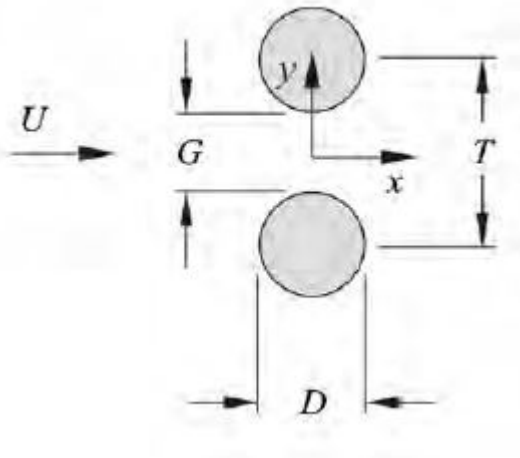

Figure 1.2: Two circular cylinders of equal diameter in side-by-side configuration. D is the cylinder diameter; T is the distance among cylinders center of mass; G is the space among cylinders. (Figure taken from Sumner 2010[28])

Interaction among wakes have been classified according to appreciable differences of their behavior. A simple classification considers the ratio T/D as the main parameter, where T and D are defined as in figure 1.2.

- When cylinders are far enough ($T/D > 2$ 2.2) wakes arise separately. Wakes can then travel in-phase and anti-phase condition. This kind of wake-interactions are identified as being in the *proximity interference* regime;

- When the $T/D < 1.2$, wakes collapse to a single wake comparable to that of a single body. This behavior is especially true when the gap between bodies is zero. Besides, when the gap is non zero, cylinders are subjected to lower hydrodynamic forces. In fact, the flow passing through the gap modify the wake in the same way the *base bleed* effect does. This condition is called of the *single-bluff-body.*;

- For intermediate values of T/D, side-by-side cylinders and their wakes present a mixed behavior, namely the *Biased flow pattern.* The wake is mainly influenced by the flow through the gap. The flow is biased towards one of the two cylinders. The cylinder towards which the flow is directed has an higher resistance to the flow and its near-wake is narrower and presents vortex shedding

at higher frequency then the other one.

Figure (1.3) shows the Drag coefficient as a function of T/D.

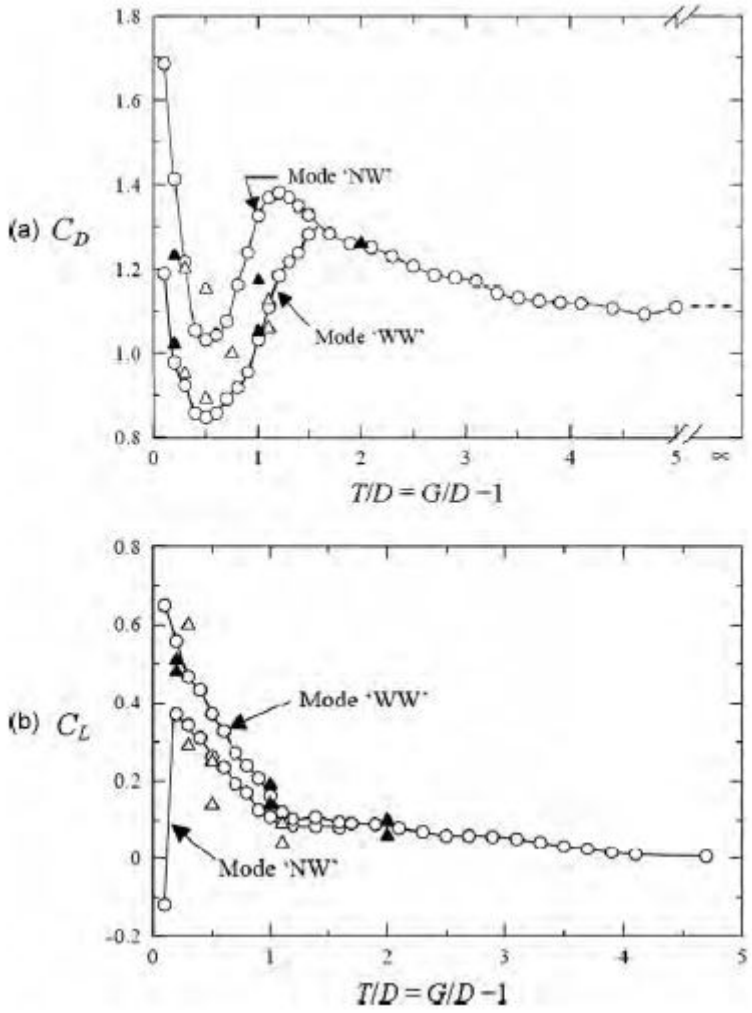

Figure 1.3: Mean aerodynamic force coefficients for two side-by-side circular cylinders as a function of the dimensionless gap ratio: (a) mean drag force coefficient and (b) mean lift force coefficient: ▲, Hori (1959) [14], Re=8000, △, Zdravkivich and Pridden (1977) [32], Re=60000, ∘, Alam et al. (2003a) [2], Re=55000. Mode 'NW' = cylinder with the narrow wake; Mode 'WW' = cylinder with the wide wake. (Figures taken from Alam et al. (2003a) [2]. The picture has an error in the label of the horizontal axis. The minus sign has to be a plus.)

The *base bleed* occurs when a fluid is injected in the region behind the body where the separation of the boundary layer occurs. The base bleed effect consists in moving downstream the position of the vortex formation, thus, the drag force is reduced, while the pressure behind the body increase. For the couple of cylinders, the base bleed effect is induced by the high momentum fluid entering the gap between cylinders.

Other coupled bodies were subjected to studies on hydrodynamic resistance behavior as a function of the distance among them. In particular, *Dewey et al.* (2014) [11] studied effects of the distance between bio-inspired oscillating hydrofoils on their propulsive performance. The variables of the study were the distance between foil normalized with the foil length, D^*, and the difference of foils oscillation phase, ϕ.The study highlighted that both the distance and the oscillation phasing have an effect on the thrust and on the power consumed. In particular, the reduction of the distance between foils magnify the effect of the oscillations. Where, in phase oscillation reduces both the thrust produced and the power consumed, out of phase oscillation enhanced the power consumed and the thrust produced, while, intermediate phase oscillation reduced the studied quantities for one foil while increased them for the other. Results are shown in figure (1.4). Dashed lines enveloping their results in figure are described by a power law with a decay $\alpha D^{*-0.4}$. This law was depicted by *Quinn et al.* (2014) [26] to describe the thrust of an airfoil oscillating at a distance, normalized on the airfoil chord, comprised among 0.25 and 2.9 chord lengths to the ground.

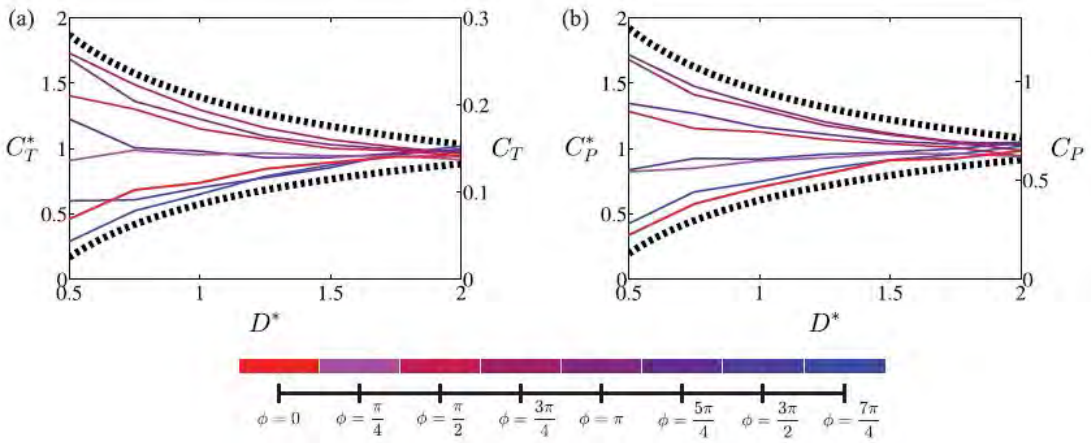

Figure 1.4: Propulsive performance for foil 1 (where foil 1 is one the 2 foils used for the study) as a function of foil spacing $D*$. (a) Coefficient of thrust and (b) coefficient of power. The data are contained in the envelop defined by the dashed lines, denoting a power law with a decay $\alpha D*^{-0.4}$ (Proposed by *Quinn et al.* (2014) [26]. The data for the various phase differentials are denoted by the solid lines, note that the line colors defined in the legend are used in both figures. (Figure taken from *Dewey et al.* (2014) [11]) (C_T is the average thrust coefficient, C_P is the average power coefficient, $C*_P$ and $C*_T$ are normalized quantity).

Chapter 2

Collective behavior in fish

The specialized literature presents many studies having the aim of justify the fish schooling[1]. These works studied many mechanisms that might have a role in in schools formation and conservation. First, works by *Godin et al.* (1988) [12] and *Cresswell, W.* (1994) [10] suggested that being in a group offers better protection against predators by an increased chance of detecting them. Second, a defensive mechanism that groups of animals might experience is the so-called *confusion effect*[2] introduced by *Jeschke and Tollrian* (2007) [15]. Third, being part of a school could enhance the success in foraging (*Krause and Ruxton* (2002)[18]). Finally, another benefit of being part of a group is related to reduction of cost of locomotion [20].

Previous experiments studying the relation between the pattern taken from couples of Minnow (*Phoxinus phoxinus*) and the difference in water velocity highlighted a change in the behavior of fish. In fact, in standing water fish do not show preferential swimming configuration, whereas, in moving water, they tend to adjust themselves side by side at a distance of 0.3 body lengths (Sec 2.2). Hence, the present work aim is to verify the presence of a hydrodynamic benefit fish might have adopting the side-by-side swimming configuration.

[1]Modern biologists define ordinate, thus all members face the same direction, and not ordinate aggregation of fish as two different entities. An ordinate aggregation of more fish is called *school* while a not ordinate aggregation is a *shoal*.

[2]The *confusion effect* occurs when a predator is not able to single out from the group a prey.

2.1 Fish biology

Fish developed many important adaptations to overcome limitations caused by the surrounding environment. Many species developed unique features, but modern biologists agree upon thinking different species have a common ancestor [9]. One heritage of their ancestor is the *lateral line*, which is a sensorial organ spread along the fish body. Many fishes present the lateral line as a system of canals set on the head and along the body where there is usually a main canal [8, 9]. Figure 2.1 shows the lateral line for a *Phoxinus phoxinus*. The organ allows them to understand the direction of the incoming vibration by comparison of different cells stimuli. *Partridge and Pitcher* (1980) [22]tested effects of the lateral line and of the vision on fish schooling capacity. In particular, they studied the difference in the fishes' preferred *distance to the nearest neighbor* (NND) that fish handicapped of one or both the organs have. They observed both-sides blind fish tend to have an increased NND, while fish with sectioned lateral lines tend to be closer to their neighbors.

Thus, it is possible that stimuli fish receive from the lateral line and the sight might have an important role in the interpretation of the data from which the present work starts. In fact, the flowing water and the turbulence modify lateral line stimuli and might reduce fishes' perception of the surrounding.

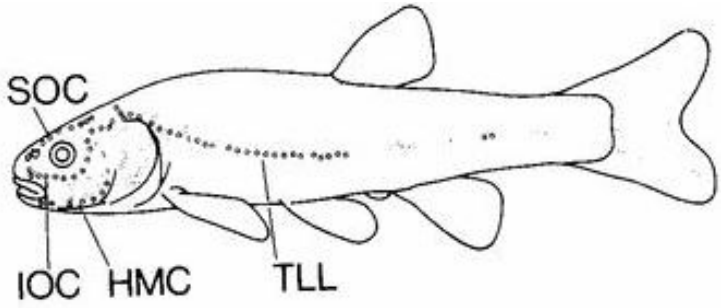

Figure 2.1: Distributin of ordinary lateral line organs in *Phoxinus phoxinus*: • Free Neuromasts; ∘ Canal Pores. SOC, supra-orbital canal; IOC, infra-orbital canal; HMC, hyo-mandibular canal; TLL, trunk lateral line. (Taken from *Bleckmann, H.* (1986) [7])

The work *Weish, D.* (1973) [30] , following a theoretical approach, analyzed

hydromechanical benefits of fishes swimming in a rear line of two-dimensional diamond-shaped schools. The Weish's study required many assumptions:

- *Boundless school.* Weish assumed that a fish swimming inside a school large enough perceive the surrounding as if the school is boundless;
- *Synchronized swimming.* Starting form the definition of a school as a group of fish swimming synchronizing the tail beat, Weish imposed this condition to the studied school.
- *Schooling fishes have same size and length.* Thus, being the velocity of fishes a function of their length, they have the same velocity;
- *Two-dimensional analysis.* Weish analyzed phenomena as they were mainly two-dimensional, as it occurs for schools swimming in shallow water or for layers of superimposed animals;
- *Viscous-less fluid.* To simplify the study, Weish neglected viscosity effects (e.g. dissipation).

Given these assumptions, Weish defined three types of hydraulic benefits. First, he affirmed that a fish in position **B** gets an hydrodynamic benefit by swimming in between fishes **A** and **C** wakes (Fig. 2.2). In fact, being fish swimming in a synchronized manner, the fish in position **B** experiences a positive thrust induced by vortices.

Second, he theorize the possibility that the lateral distance among fish influences the energy saving. As for the drag of a body shedding a vortex trail between confining barriers is enhanced by the presence of the barriers, neighbors fish influence the drag of the focal fish as they and their wake resemble walls for the focal fish wake. Thus, in steady water, the increasing of drag is related to the increasing of the relative velocity of fish.

Third, in a large enough school swimming in moving water, the fluid velocity of water surrounding the focal fish is reduced by the resistance induced by upstream fish. Hence, being forces on fishes a function of the square of the velocity around them, a denser school could leads to a lower force on fish who can then experience a benefit on the energy consumption conserving the same relative velocity.

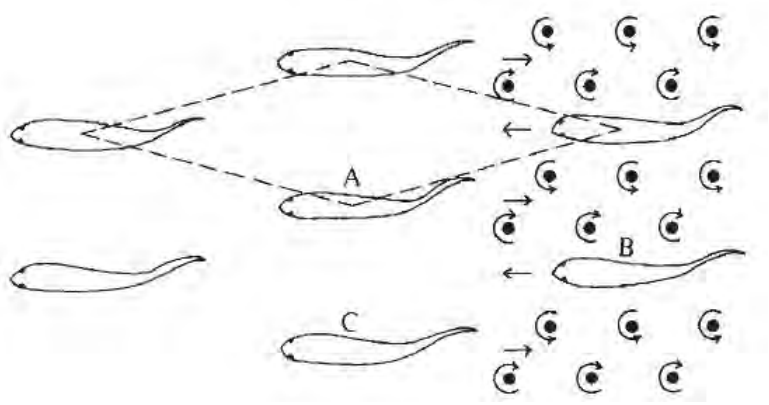

Figure 2.2: Part of a horizontal layer of fish in a school, from above. Arrows near vortex streets show direction of induced flow relative to the vortexes. The dotted line shows a "diamond" patter. (Figure taken from *Weiah D.* (1973)[30])

Partridge and Pitcher (1979) [24] tested Weish theory. They showed that fish have no tendency to place themselves centrally between pairs of school members swimming ahead. Fish also do no maintain a planar formation and their swimming presents no phasing. Yet, they confirmed the formation of vortices where Weish predicted.

Hemelrijk et al. (2014) [13] studied hydrodynamic benefits fish experience from swimming in schools utilizing a *Multi-Particle Collision Dynamic* model. According to authors, this model can account for interaction among wakes and among wakes and individuals and considers viscous effects. Parameters of the model are patterns of the school and distances among fish. Studied schools are boundless in one or two direction following dimensions of the school pattern which could be: *diamond*, the same pattern Weish studied; *in-line*, *rectangular* and *side-by-side phalanx* configurations. These kind of infinite schools were created through the introduction of periodic boundary conditions. Results showed a general benefit for a fish belonging to a school instead of swimming alone. The only school pattern presenting opposite results is the phalanx configuration, which, for distances among animals lower than 0.8 fish body lengths, has a *Froude efficiency*[3] lower then that of a fish swimming along. Results are reported in figure (2.3). The au-

[3]The *Froude efficiency* is the dimensionless ratio between the power used to move forward and the total power.

thors' explanation of this result is that, being the school boundless, the increasing of the resistance due to the proximity lowers the school velocity and overcomes other beneficial effects of schooling.

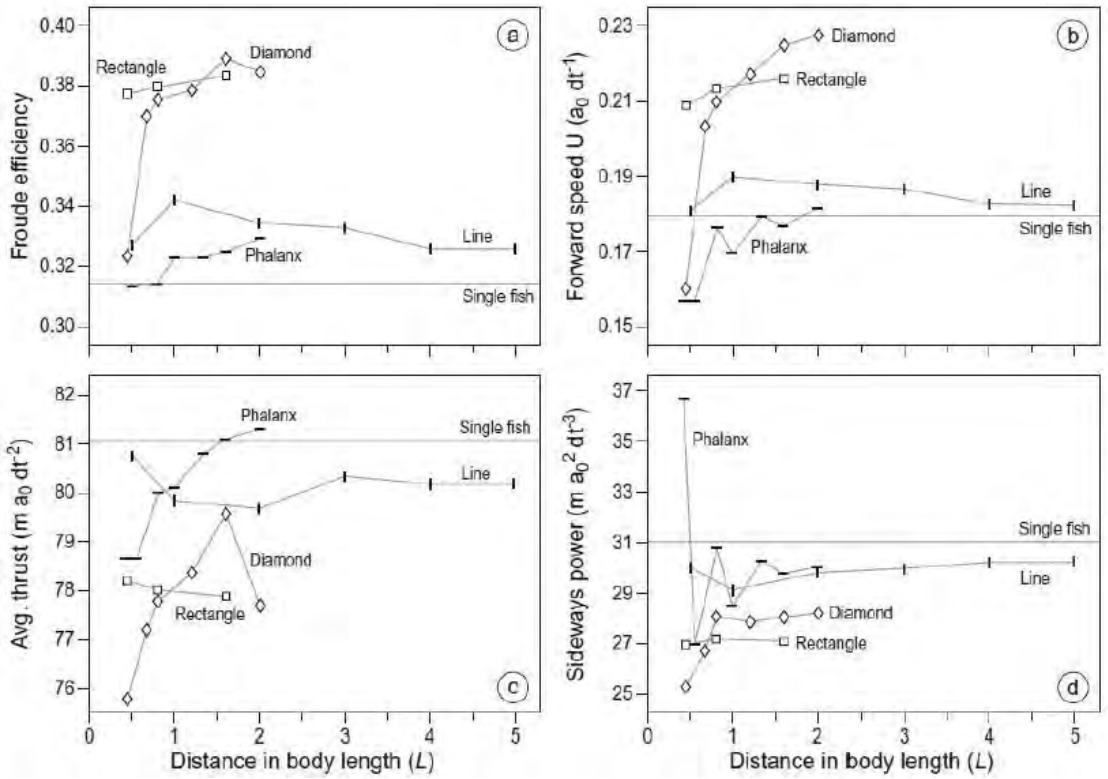

Figure 2.3: Froude efficiency ν (a), speed (b), average thrust (c) and sideways power (d) of different configurations for different distances (in body length L) among individuals. The phalanx, rectangular and diamond configuartion are studied at several laterl distance (dy) and the line formation at several longitudinal distances (dx). Note that due to the large sample size (20 tailbeats or 130.000 time steps) the standard error is essentially zero. (Figure taken from *Hemelrijk et al.* (2014) [13]) ($a_0 = 1.4 \cdot 10^{-4}m$, $m = 1.83 \cdot 10^{-11}kg$ and $\Delta t = 1.5 \cdot 10^{-4}s$ are unit length, unit of mass and unit time respectively)

2.2 Experiments data

This work starting point are fish positions and directions data collected between 2013 and 2015 at the *University of Southampton*. Experiments were made as part

of a research on response of Minnow (*Phoxinus phoxinus*) schools to flow field. These had been conducted at *University od Southampton*'s hydraulic laboratory at Highfield Campus in Southampton.

Two fish were placed in the flume and their motions were recorded with a camera placed above them (Fig. 2.4). Their behavior have been studied for three flow conditions: high flow (velocity 11.57 ± 0.08 m/s, water depth 3 cm), low flow (5.74 ± 0.03 m/s, 6 cm) and a control condition with standing water. Ten trials were made per each flow condition, so a total of thirty thirty-minutes-long movie were recorded. Suitable thirty-second-long movie parts were selected according to the distance among fish (lower than 4 body length) and fish distance form walls. Form each trials only five minutes of movie were analyzed.

Figure 2.4: A frame of one of the video recorded with high flow condition.

Distance between fish were calculated and statics were done utilizing *Ctrax* (fig. 2.5 and fig 2.6), a Matlab® utility.

Results for two-fish school, the case of interest, are shown in figure 2.7 and figure 2.8. In particular, figure 2.7 shows the fish' preferred position in different flow condition, while figure 2.8 shows changes induced by flow condition on fish direction. Figures 2.8 (b) and (c) show that fish prefer to face the flow when it exist. Instead, in standing water (fig. **??** (a)) they do not show a preferential swimming direction. Instead, figures 2.7 (b) and (c) do not show the same uniformity as figures 2.8 (b) and (c). Hence, fish react differently for different flow velocities.

Nevertheless, when the velocity is high they show a preferential position which is different to what observed in standing water (fig. 2.7 (a)).

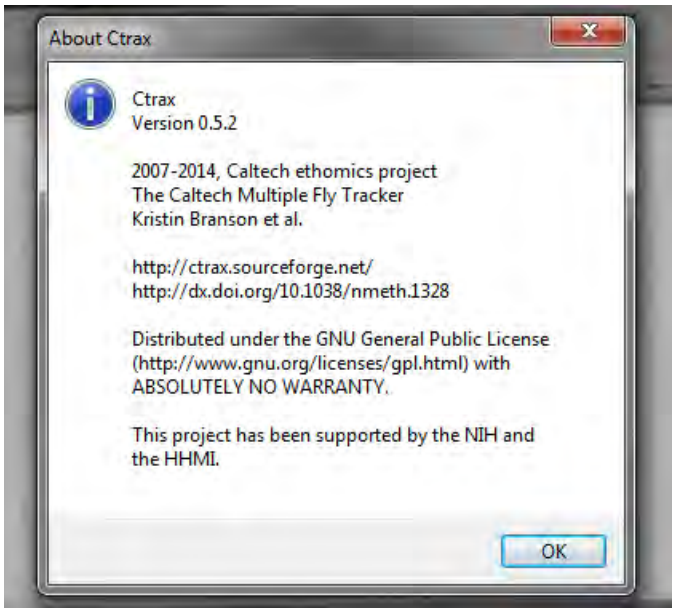

Figure 2.5: Informations about Ctrax

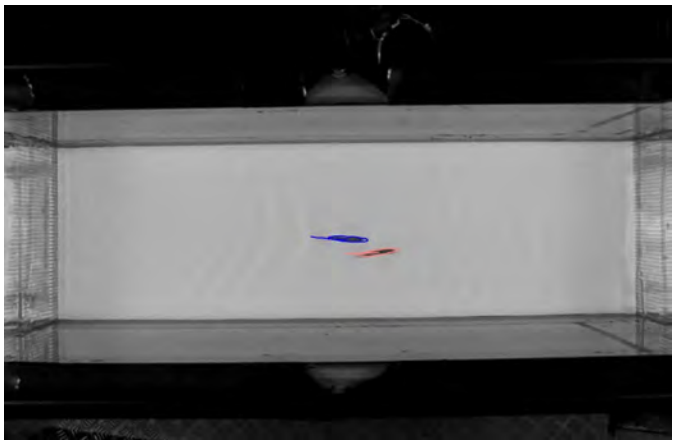

Figure 2.6: Tracking of fish position.

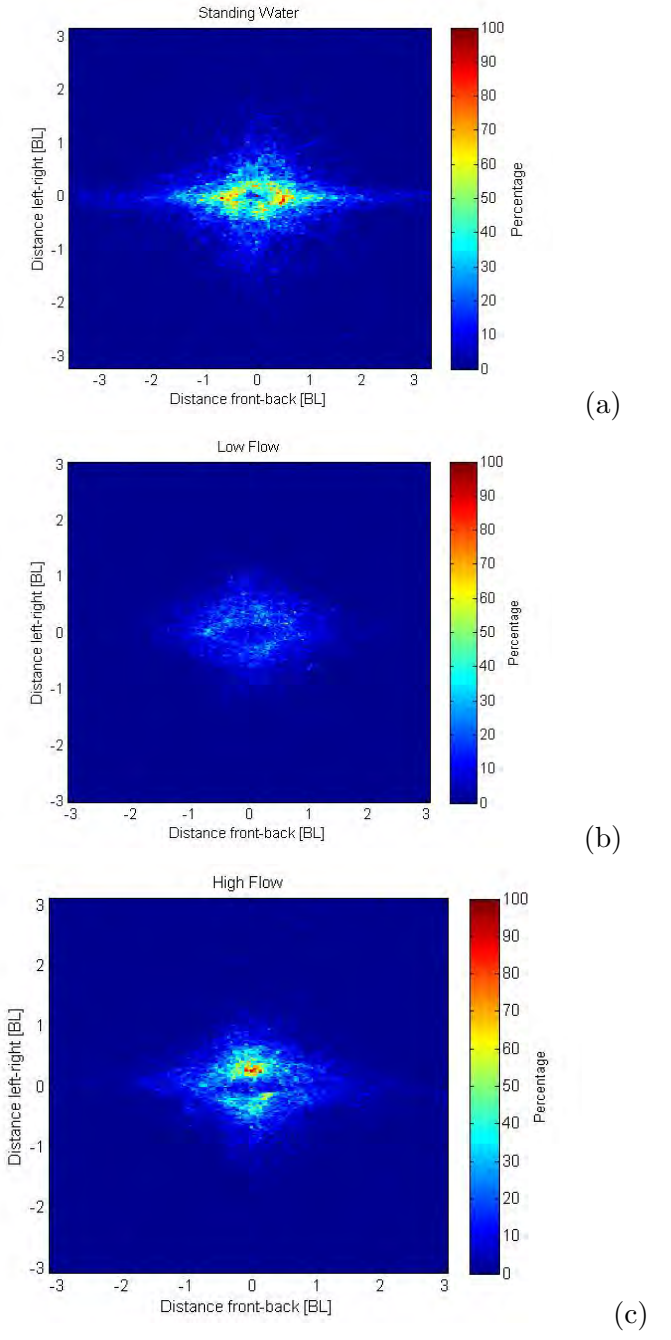

Figure 2.7: Probability density of the position of the neighbor fish respect to the focal fish position. From the top: (a) Standing Water case; (b) Low Flow case; (c) High Flow case.

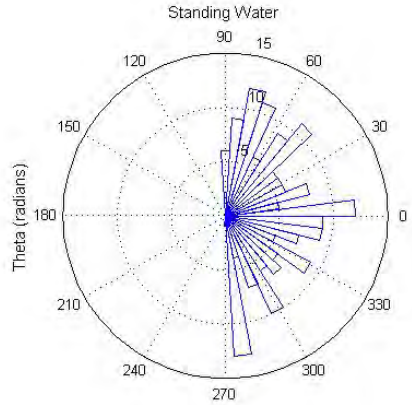

(a)

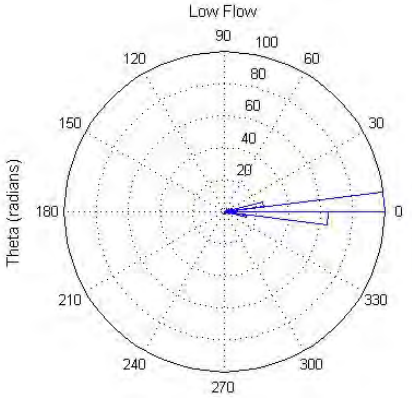

(b)

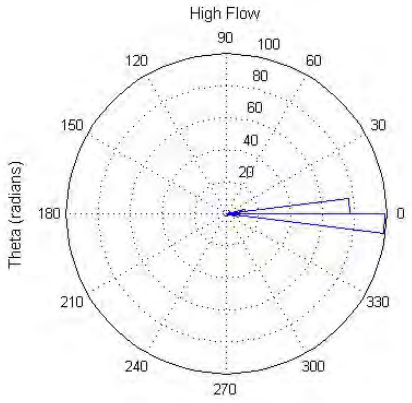

(c)

Figure 2.8: Orientation of fishes compared with the main direction of the flow in different flow conditions. From the top: (a) Standing Water case (Reference direction is the same as other cases); (b) Low Flow case; (c) High Flow case.

Chapter 3

Numerical Methods

3.1 General consideration on CFD

Computational Fluid Dynamic, shortly *CFD*, is the name of that branch of fluid mechanic applying numerical methods to solve problems that involves fluid flows. Within this work, *CFD* were used to evaluate drag coefficients and lift coefficients of side-by-side coupled fish with different distances between them. However, the use of numerical methods is strictly related to computers CPUs and memory capabilities and to time availability [3].

Direct application of Navier-Stokes equations (Eq. 1.5) leads to the so-called *Direct Numerical Simulation* method, *DNS*. Theoretically this method can solve both laminar and turbulent flows, but requires an extremely fine mesh in order to properly solve momentum transport equations among cells. It is practically impossible for turbulent flows especially considering that the number of computations required to calculate parameters value increase with the cube of the flow Reynolds number.

A smarter way to directly apply Navier-Stokes equations (Eq. 1.5) is the *Large Eddy Simulation* method, *LES*. It explicitly solves *NS* equations only for large turbulence scales. Smaller scales effects are taken into account through a subgrid stress model. *LES* requires a coarser mesh then *DNS*, hence, the method can be used for practical purposes, but still its computational effort is far greater then what this work available computers could bear within a reasonable amount of time.

CFD became affordable with the introduction of numerical methods coupling

RANS equations (Eq. 1.7) with a model describing turbulence.

RANS-based turbulence models are born after the need of a mathematical description for *Reynolds Stresses* (Eq. 1.8). The *Boussinesq Approximation* (sec. 1.1.3) is the commonly employed closure hypothesis for *RANS* equations. It defines a relation between Reynolds stresses and an introduced new parameter, i.e. the *turbulence viscosity*.

Assuming to have an initial cell-centered guess of the variable of interest, in this case velocity magnitude and direction, obtained after the *initialization* of the problem, a *discratization scheme* must be applied in order to calculate the variable values at cells' boundaries. These values are required to perform the momentum balance of each cell and therefore to increase the accuracy of results through an iterative solution of the new set of equations. The result is accurate enough when its variation between two consecutive iteration is lower then a threshold value identified as *tolerance*. The satisfaction of this criterion allow to say that the solution reached *convergence*.

3.1.1 Initialization

A *Hybrid Initialization* scheme has been used in order to define the initial condition for the solver [4]. This initialization is a package of many equations that roughly labels the status of the system. The velocity field is described through the Laplace equation (Eq. 3.1) of the velocity potential, ψ.

$$\nabla^2 \psi = O \tag{3.1}$$

The velocity components can be defined through it as:

$$u_i = \frac{\partial \psi}{\partial x_i} \tag{3.2}$$

Other conditions on velocity considered by hybrid initialization are described by boundary conditions like:

- *Wall Boundaries* - The velocity component normal to the wall is zero:

$$u_n = \frac{\partial \psi}{\partial n}|_{wall} = 0$$

- *Inlet Boundary* - Velocity components at the boundary inlet are taken as user-specified values:

$$U = \nabla\psi_{inlet} = U_{user}$$

- *Far Field Boundary* - Far from sources of discontinuity, the velocity field maintains the same directions as at the inlet boundary;

- *Outlet Boundary* - At outlet boundaries, the initial solution is that obtained specifying the zero potential condition.

The pressure field is initialized with the averaged constant value from the boundaries. Other boundary conditions, including those for turbulent parameters, are initialized with constant values averaged over the domain.

3.1.2 Meshing

Good meshing is fundamental in order to obtain reliable results. Inappropriate meshing usually gave numerical problem and bad results [3].

There are two different types of mesh: *structured* and *unstructured*. Mesh belonging to the first type are created strictly using four-edges elements in 2D problems and hexahedral elements in 3D problems. This kind of mesh lead to a faster and less memory-consuming solutions. Unstructured meshes are made with three-edges and four-edges elements in two-dimensional problems, while they use up to twelve-edges elements in three-dimensional problems. This type of meshes is more appropriate for complex geometries.

Numerical errors reduce according to the reduction of cells dimension. However, the shortcoming is the increasing of computational effort required from the solver that can yield to prohibitive simulation time.

3.1.3 Equation discretization and discretization schemes

PDEs[1] describe continuous fluid behavior. The process of modifications of the equations in order to allow them to describe a discrete domain is called *discretiza-*

[1]Partial Differential Equations

tion. Its drawback is the introduction of numerical errors into the solution.

The error is due to the "fineteness" of the discretization itself compared to the continuum character of variables such as velocity or scalars like, e.g. temperature.

The program stores parameters as cell-centered quantities, ϕ_i[2] (Fig.3.1). For every iteration the cell faces value, ϕ_{i-j}[3], needs to be evaluated in order to calculate parameters value of the downstream cells. *Discretization Schemes* offer a way to calculate ϕ_{i-j}. Different discretization schemes produce different errors according to their way to calculate the value of variables at the cells boundary.

The simplest discretization scheme is the so-called *central differencing* scheme. It describes faces values as the distance-weighted mean of the variable value in two adjoining cells and the gradient between them as a linear interpolation of cells values. This is a good approximation for problems where two adjacent cells have the same relevance on the the value of the face between them, but, if the problem presents an high enough convective character of the flow, the face value has to be more related to the upstream cell value then to the downstream one. In order to take better into account convective effects *Upwind schemes* are commonly employed.

Upwind schemes applied to this study are listed in table 3.1.

Name	**Principle**	**Drawback**
First-order upwind	The face value is equal to the cell value of the upstream cell	It overestimates the transport of entities in the flow direction, thus, it increases the numerical error
Second-order upwind	The gradient of the parameter between the present cell and the downstream cell is the same as the gradient between the upstream cell and the present one	The scheme is *unbounded*[4]

Table 3.1: Discretization Schemes

[2]Where i is the the cell reference number

[3]Where $i - j$ combination of numbers is the reference of the face between cells i and j

The second-order upwind scheme, described in table 3.1, is the scheme most used within this work. Thus, a better explanation of how the scheme works and how the second-order accuracy is obtained is given here. The second-order accuracy is the consequence of calculating faces value, ϕ_{i-j}, through a Taylor Series Expansion of the cell-centered solution calculated the previous iteration, ϕ_i, about the cell center. This procedure requires the knowledge of the parameter gradient in the upstream cell, $\nabla\phi_i$, and of the displacement vector between the upstream-cell center and the face centroid, $\overrightarrow{r}_i$, (Fig. 3.1). The equation of the face value, ϕ_{i-j}, is:

$$\phi_{i-j} = \phi_i + \nabla\phi_i \cdot \overrightarrow{r}_i \tag{3.3}$$

The gradient $\nabla\phi_i$ is hence limited to avoid new maxima or minima. $\nabla\phi_i$ is a focal parameter. It is not only required to calculate face values. It appears also in the computation of secondary diffusion term and in velocity derivatives. This parameter is calculated through the *Least Squares Cell-Based Gradient Evaluation* method described in the ANSYS® Fluent theory manual [4].

Having already defined the way to obtain the face value of parameters of interest allow to address the discretization of equations.

ANSYS® Fluent obtains discrete transport equations integrating general transport PDEs (Eq. 3.4) about each control volume defined as the cell.

$$\int_V \frac{\partial\rho\phi}{\partial t}\, dV + \oint p\phi U dA = \oint \Gamma_\phi \nabla\phi dA + \int_V S_\phi\, dV \tag{3.4}$$

Where (Fig. 3.1):

- ϕ is a non-specified parameter;
- ρ is the density of the fluid;
- U is the velocity vector;
- dA and dV are respectively the infinitesimal element of surface and volume;
- Γ_ϕ is the diffusion coefficient for ϕ;

[4] A *bounded* variable has a cell boundary value which is neither higher or lower the surrounding values. An *unbounded* scheme could lead to a not convergent solution.

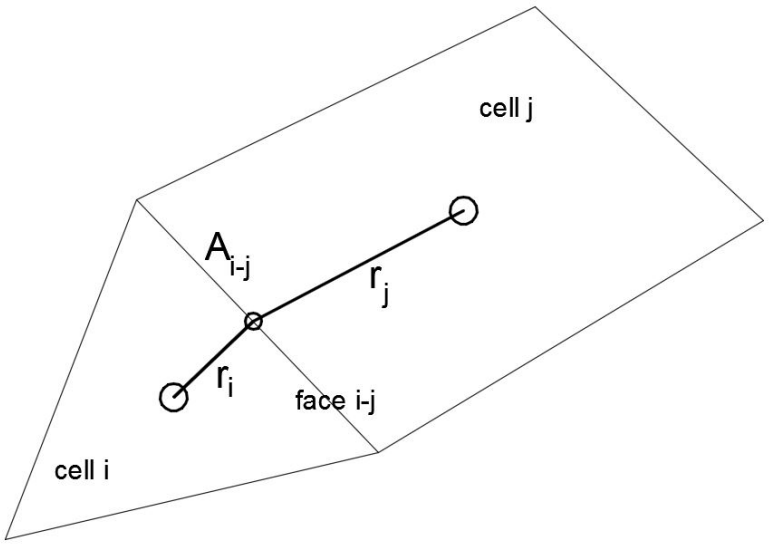

Figure 3.1: Control volume used to illustrate *Discretization* of a scalar transport equation. Cells i and j are two random adjacent cells. Face $i-j$ is the cells contact surface. A_{i-j} is the surface of the face. r_i and r_j are vectors describing the path between surface centroid and cell center.

- $\nabla\phi$ is the gradient of ϕ;
- S_ϕ is the source of ϕ per unit volume.

Equation 3.4 is solved for each cell. Solving it for the right hand cell, *cell j*, showed in figure 3.1 leads to equation 3.5:

$$\frac{\partial \rho\phi_j}{\partial t}V + \sum_{i-j}^{N_{faces}} \rho_{i-j}\overrightarrow{U}_{i-j}\phi_{i-j}A_{i-j} = \sum_{i-j}^{N_{faces}} \Gamma_\phi \nabla\phi_{i-j}A_{i-j} + S_\phi V \qquad (3.5)$$

where:

- ϕ_{i-j}, value of the selected parameter at the face $i-j$;
- N_{faces}, number of faces enclosing cell j;
- $\rho_{i-j}\overrightarrow{U}_{i-j}A_{i-j}$ is the mass flux through cell boundaries;
- A_{i-j} is the area of the boundary. In the 2D case, it is a length;
- $\nabla\phi_{i-j}$ is the gradient of the parameter at the cell boundary;

- V is the cell volume.

The first term of equation 3.5 is the so-called *Temporal Discretization*. In this thesis, when the transient solution was studied, a *Bounded Second Order Implicit Time Integration* scheme was adopted.

An example of discretization is that of equation 3.6. This is the linear equation obtained from the integrated form of the x-momentum equation:

$$u_j a_j = \sum_i a_i u_i + \sum p_{i-j} A_{i-j} \cdot \hat{\boldsymbol{i}} + S \tag{3.6}$$

Where:

- a_j and a_i are constants of the present, j, and neighbor cell, i;
- u_j and u_i are cells x-direction velocity component. u_j is an unknown of the problem;
- S is the source of momentum;
- $p_{i-j} A_{i-j} \cdot \hat{\boldsymbol{i}}$ is the flux of momentum through the cell boundary in the x-direction and is unknown. Where A_{i-j} is the face surface and p_{i-j} is the pressure.;
- $\hat{\boldsymbol{i}}$ is the vector describing the x-direction.

u_j and $p_{i-j} A_{i-j} \cdot \hat{\boldsymbol{i}}$ are both unknown a-priori. They must be calculated in order to obtain a solution.

p_{i-j} is a face parameter. It requires some assumption in order to be derived from cell-centered parameters. ANSYS® Fluent offers many ways to do it. Within this work the used scheme is a second order accurate scheme similar to the Second-Order Upwind Scheme. As the Second-Order Upwind Scheme this *Pressure Second-Order* scheme is unbounded. In order to avoid convergence problems first iterations were done with the *standard* scheme.

Therefore, thanks to the discretization, ANSYS® Fluent can work on a set of linear equations where cell-centered quantities are the unknowns.

3.1.4 Pressure-Velocity coupling

After the initialization phase, the system is defined with a set of cell-centered values which are relatively far from real. Hence, the solution needs to be improved through an iterative procedure because more accurate values of cell-centered parameters need to be calculated.

ANSYS® Fluent allows to apply different algorithms to do this. Two main categories have been defined:

- *Segregated Algorithm.* This is an algorithm that solves equations sequentially (Fig. 3.3). This method is memory-efficient, but more time consuming;
- *Coupled Algorithm.* The coupled solution of the momentum and continuity equation requires more memory, but it is less time-consuming. Other equations, such as turbulence parameters transport equations, are solved in a second stage (Fig. 3.2).

The scheme used within this work is a scheme belonging to the family of coupled algorithms. Its name is *Coupled Scheme*. The scheme offers a robust and efficient single phase implementation for steady-state approach and it is superior to segregated algorithm such as *PISO Scheme* for transient simulation when large time steps are necessary.

3.1.5 Convergence and tolerance

It is said *convergent* a function, $f(x)$, which verifies $\lim_{x\to \boldsymbol{a}} f(x) = \boldsymbol{X}$, where $\boldsymbol{X}$ is a finite value, while $\boldsymbol{a}$ might be both finite or infinite. Being the definition of a convergent function based on a limit, the exact value of the solution cannot be reached. The *convergence* is reached when the difference between the solution of two consequent iterations is smaller then a certain threshold called *tolerance*.

ANSYS® Fluent measure the convergence of each parameter comparing the *sum of Residuals* with the tolerance [5]. Residuals are given by the difference between left hand and right hand sides of the linearised transport equation of ϕ (Eq. 3.7) of two consecutive iterations.

$$a_j \phi_j = \sum_i a_i \phi_i + b \tag{3.7}$$

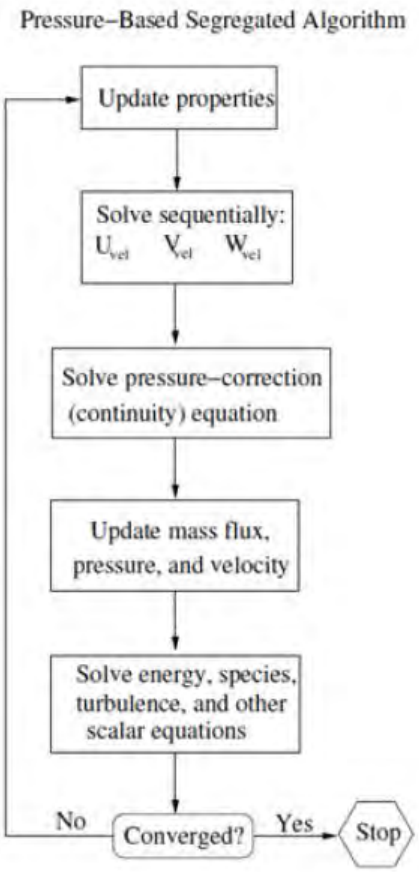

Figure 3.2: Segregated Algorithm scheme [4].

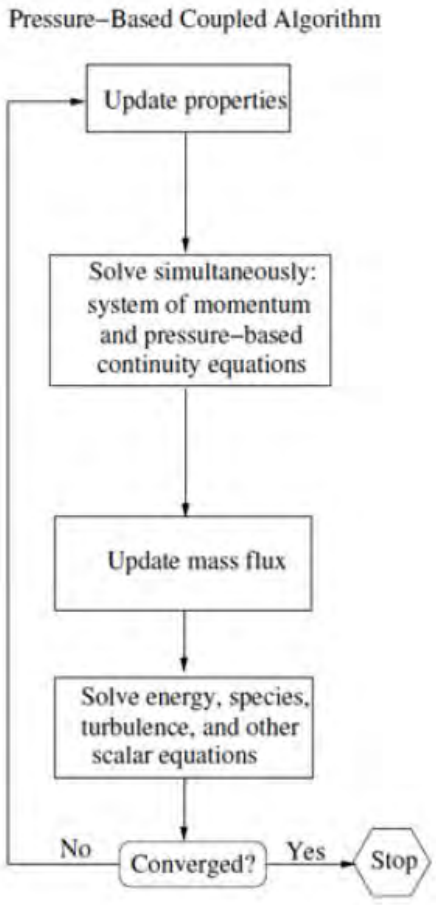

Figure 3.3: Coupled Algorithm scheme [4].

Where:

- a_j and a_i are constants of the present, j, and neighbor cell, i;
- ϕ_j and ϕ_i are cell-centered parameter;
- b is a constant source of ϕ.

This definition of *residuals* leads to:

$$r^{\phi} = \sum_{i} a_i \phi_{i,0} + b - a_j \phi_{j,-1} \tag{3.8}$$

Where:

- $\phi_{i,0}$ is the neighbor cell present iteration value;
- $\phi_{j,-1}$ is the present cell past iteration value;

In order to simplify the comprehension, residuals of all cells are summed and normalized with the summation of the left-hand part of equation 3.7:

$$R^{\phi} = \frac{\sum_j |\sum_i a_i \phi_{i,0} + b - a_j \phi_{j,-1}|}{\sum_j |a_j \phi_{j,-1}|} \tag{3.9}$$

The solution was considered correct only when residuals, R^{ϕ}, were lower then the tolerance, T^{ϕ}.

3.1.6 Y^+ adaptation

ANSYS® Fluent allows to refine or to coarse wall nearest cells in order to make these of the right dimension according with rules on near-wall functions.

The approach proposed by the program is quite easy. When, after a certain number of iteration decided by the user, Y^+ is not conform to rules given by the selected turbulence model cells can be coarsened or refined according to specific needs (Sec. 3.3.4).

Coarsening and refining procedures are done as shown in figure 3.4.

3.2 ANSYS® Fluent and the applied procedure

The software used to simulate flows is ANSYS® Fluent. This is a commercial software produced by ANSYS® Inc. The software is one the most wide-spread simulation-driven numerical solvers in the market.

The procedure for simulations and solver setting is made of the following steps (Fig. 3.5):

- *Geometry modelling.* The geometry of the domain and of the simulated object is first created with a CAD software and then imported in the mesh creator software which is part of the ANSYS set;

(a)

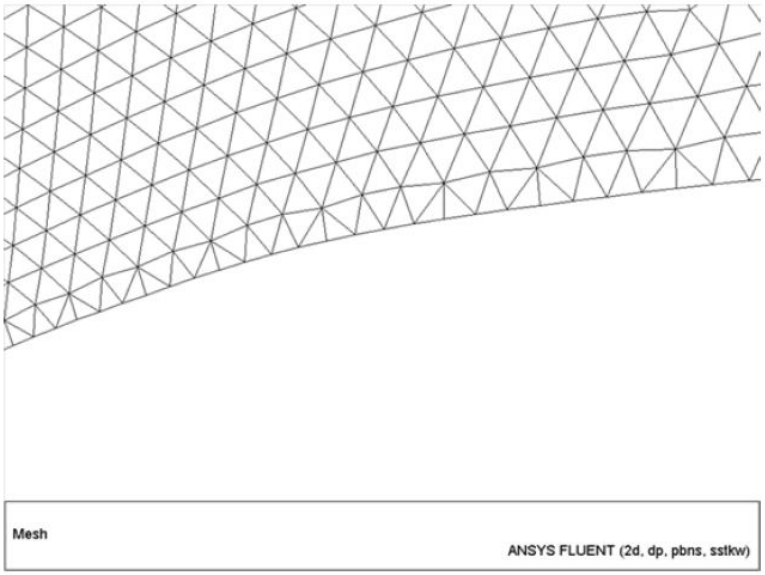

(b)

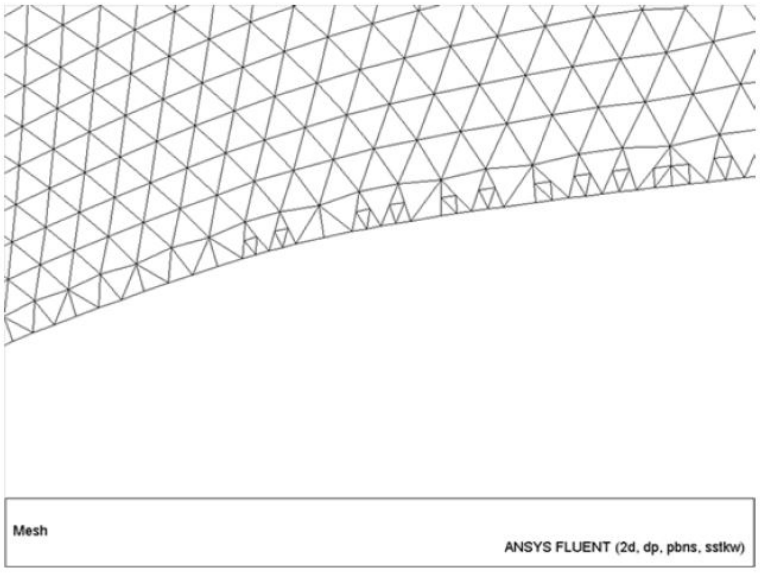

Figure 3.4: Mesh before, (a), and after, (b), refining obtained using Y^+ limitations [4].

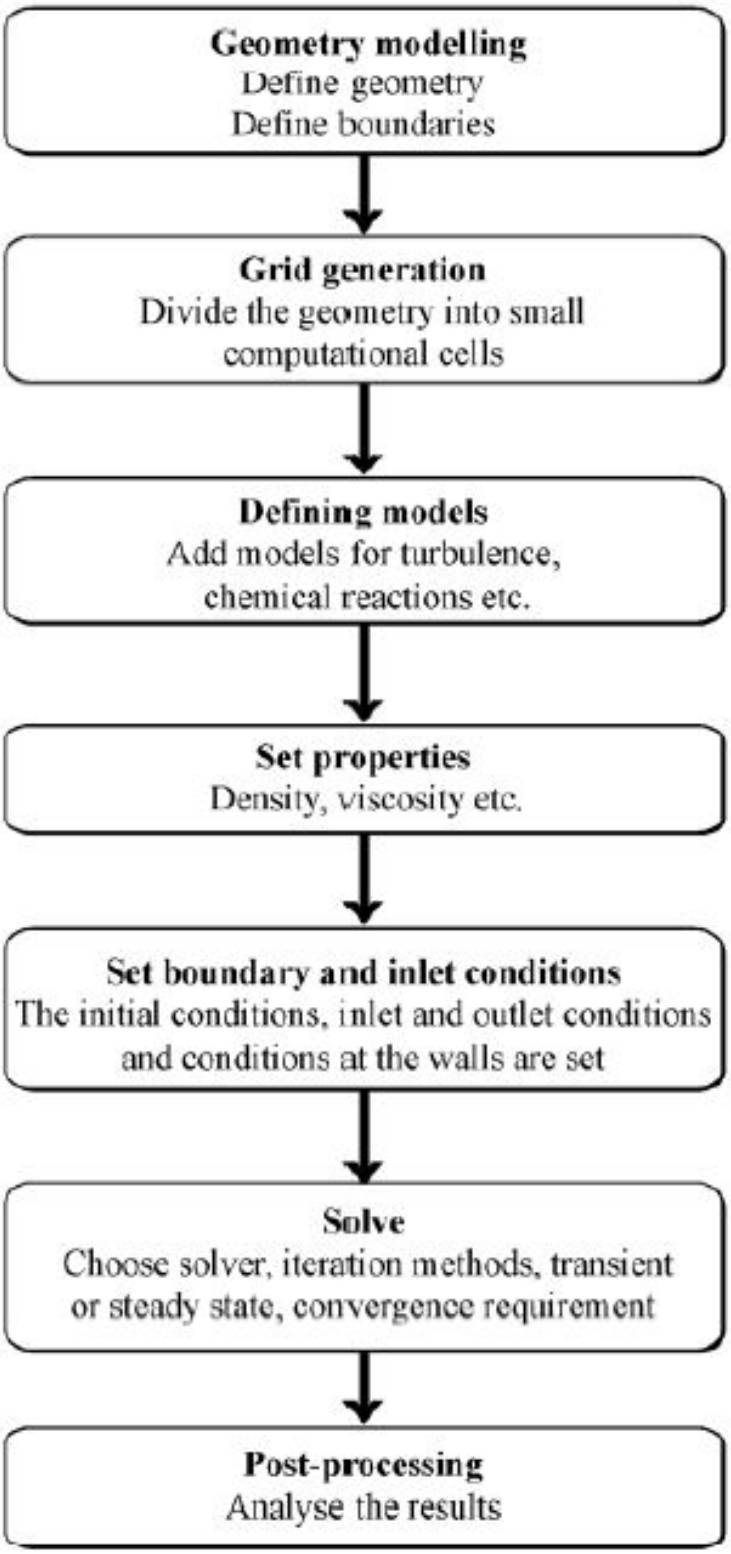

Figure 3.5: Scheme of generic steps in CFD simulations [3].

- *Grid generation.* The mesh is created using best practice and knowledge obtained from sensitivity analysis;

- *Setup of the simulation.* Now the software asks to define solver requirements such as initial and boundary conditions.

  First to come is the definitions of stored-data precision. In this work the *Double-precision* was always employed.

  The mesh is then imported into the solver. Now geometry and mesh have to be scaled using the *Scale* utility of the software. To simplify the drawing phase, one meter long fish have been created. A scale factor equal to 0.066 has been applied to every direction in order to obtain a system with consistent dimensions (see Fig. 3.6). Hence, domains dimensions can be checked with another Fluent utility.

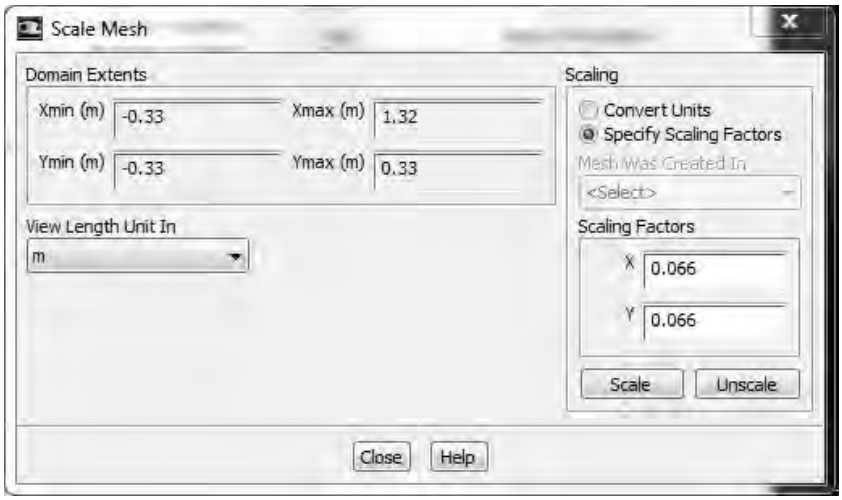

Figure 3.6: *Scale* utility graphical interface.

ANSYS® Fluent allows to choose one of the two numerical methods:

  – *Pressure-Based Solver*
  – *Density-Based Solver*

The Pressure-Based Solver is the one used in this work. It has been historically developed for low-speed incompressible flows. In the Pressure-Based approach the velocity field is obtained from the momentum equation (Eq.

1.2), while the pressure distribution is obtained from a manipulation of continuity (Eq. 1.1) and momentum equation.

The software asks now to define the model used to solve the velocities distribution (Fig. 3.7). The most widely used model within this work are the *k-ϵ RNG* and the *k-ϵ Realizable* model (described in sections 3.3.2 and 3.3.3). K-epsilon models require near-wall treatment definition. The used wall function is the so called *enhanced wall-function* (described in 3.3.4).

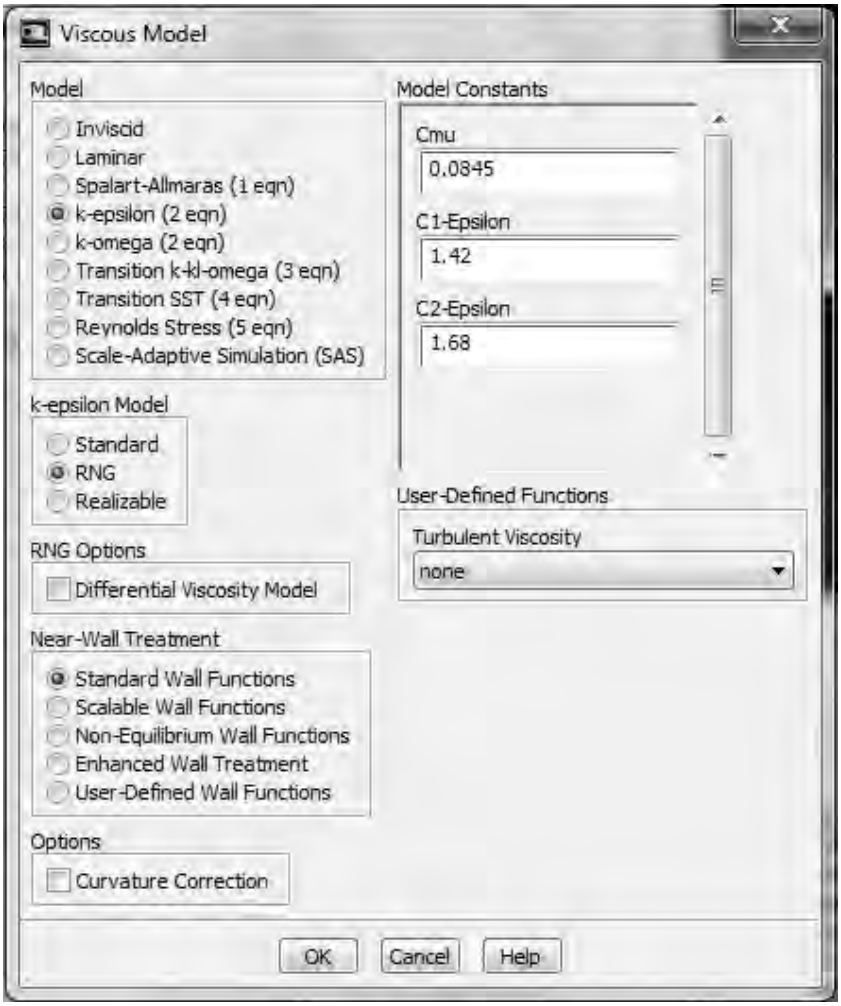

Figure 3.7: Graphical interface of the model selection phase. In the present picture the selected model is the *RNG k-ϵ* model. On the right, model constants are reported.

Fluid properties were defined as the simulated material and loaded into the

solver. In table 3.2 water properties are listed.

Property Name	**Property value**
Water Density	998.2 kg/m^3
Water Dynamic Viscosity	0.001003 $kg/m \cdot s$
Temperature	288.16 K

Table 3.2: Fluid properties used in simulations.

Boundary conditions require to be defined. The *inlet* boundary was characterize with a velocity of $0.1157m/s$, the same velocity used during experiments (Fig. 3.8). K-epsilon models, which are based on the turbulent kinetic energy, k, require the definition of the inlet turbulence. In order to do this, Fluent allows to define turbulence intensity and hydraulic diameter that through the empirical equation 3.20 define k and the boundary. Further details will be given in section 3.3.4. The downstream boundary was set as an *outflow* boundary condition. This condition enforces the continuity on the system by imposing that whatever enters the system through the inlet goes out through the outflow boundary. The use of this definition for the downstream boundary condition may generate an error if the flow through the faces of the boundary cell is directed upstream. Walls corresponding to fish boundaries were defined as "no-slip wall". Boundaries other then those described above were defined as symmetries in order to fasten calculations.

- *Setup of the solver.* The solution was *initialized* in order to give an initial distribution of parameters to the problem. The Hybrid initialization scheme was used (sec. 3.1.1).

  Tolerances for all simulation parameters were set at 10^{-5} (Sec. 3.1.5).

  Discretization schemes and Pressure-Velocity coupling schemes were then chosen. Details on them were given in section (3.1.3) and in section (3.1.4).

  As a general rule, second-order upwind schemes were used in order to limit numerical errors. Continuity and momentum equations have been always solved coupled using the *Coupled* scheme.

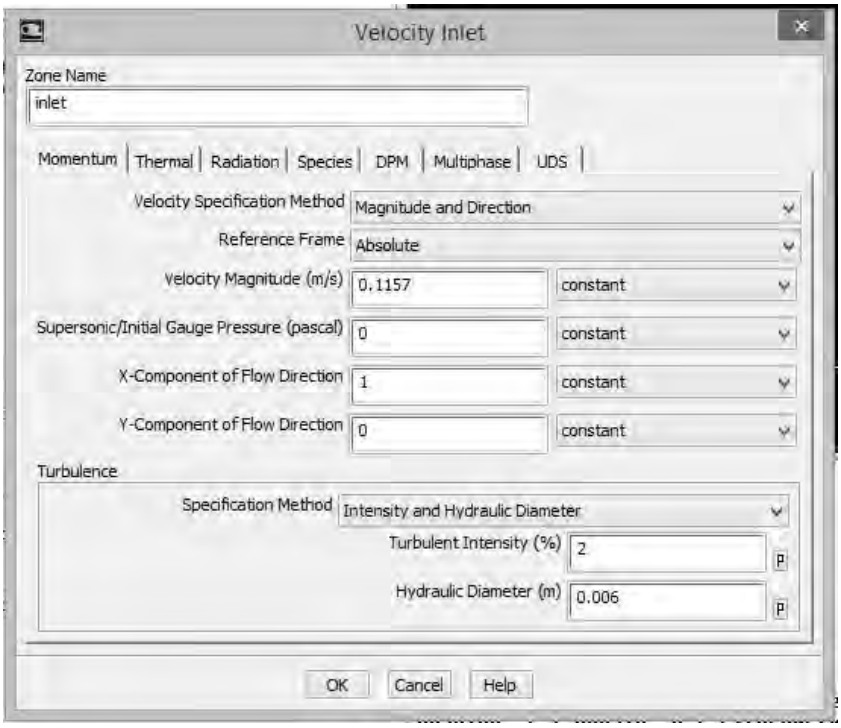

Figure 3.8: Inlet boundary condition setting. The boundary, defined through velocity and turbulence intensity values, become a Dirichlet type boundary.

3.3 K-epsilon models

3.3.1 Standard k-epsilon model

[5]The k-ϵ model is based on *Boussinesq Approximation* (sec. 1) and it belongs to the two-equation model class. Two-equation models combine RANS[6] equation with a system of 2 PDEs[7] which allows to calculate independently the characteristic velocity and length scale.

The so called *standard* k-ϵ model has been developed by Jones and Launder [16]. The equations underpinning the model are:

$$\frac{\overline{D}k}{\overline{D}t} = \nabla \cdot \left(\nu + \frac{\nu_T}{\sigma_k} \nabla k \right) + P - \epsilon; \tag{3.10}$$

[5]This section follows *S. B. Pope*[25], chapter 10 and by *Andersson et al.*[3], chapter 4.
[6]Reynolds Averaged Navier-Stokes equations (sec. (1.1.2)).
[7]Partial Differential Equations

$$\frac{\overline{D}\epsilon}{\overline{D}t} = \nabla \cdot \left(\nu + \frac{\nu_T}{\sigma_\epsilon}\nabla\epsilon\right) + C_{\epsilon 1}\frac{P\epsilon}{k} - C_{\epsilon 2}\frac{\epsilon^2}{k}; \tag{3.11}$$

$$\nu_T = C_\mu \frac{k^2}{\epsilon}. \tag{3.12}$$

Where:

- k is the turbulent kinetic energy (see section 1.1.2). It is a measure of the turbulence intensity and it is defined as half the average of the scalar product of the fluctuation velocity vector, $\boldsymbol{u}$:

  $$k = \frac{1}{2}\langle \boldsymbol{u} \cdot \boldsymbol{u} \rangle$$

  k unit of measurement is $\left[\frac{L^2}{T^2}\right]$;

- ϵ is the rate at which the turbulent kinetic energy is converted in thermal energy. Its unit of measurement is $\left[\frac{L^2}{T^3}\right]$. ϵ can be mathematically described as:

  $$\epsilon = \nu \left(\left\langle \frac{\partial \boldsymbol{u}_i}{\partial x_j} + \frac{\partial \boldsymbol{u}_j}{\partial x_i} \right\rangle \left\langle \frac{\partial \boldsymbol{u}_i}{\partial x_j} + \frac{\partial \boldsymbol{u}_j}{\partial x_i} \right\rangle \right)$$

  Where, $\left\langle \frac{\partial \boldsymbol{u}_i}{\partial x_j} + \frac{\partial \boldsymbol{u}_j}{\partial x_i} \right\rangle$ is the averaged symmetric part of the rate-of-strain tensor, $\frac{\partial \boldsymbol{u}_i}{\partial x_j}$ and $\boldsymbol{u}_i$ is the velocity fluctuation i-component. From the definition, ϵ is always a positive quantity, thus it has always a destructive contribution in the equation 3.10;

- P is the production rate of turbulent kinetic energy $\left[\frac{L^2}{T^3}\right]$;

- σ_k is the turbulent Prandtl number $\left(\frac{\nu_T}{\Gamma_T}\right)$;

- σ_ϵ is the turbulent Prandtl number for dissipation;

- $C_{\epsilon 1}$, $C_{\epsilon 2}$ and C_μ are other dimensionless constants of the model.

Launder and Sharma [19] gave a value for the model constants:

$$C_{\epsilon 1} = 1.44 \; C_{\epsilon 2} = 1.92 \; C_\mu = 0.09, \; \sigma_k = 1.0 \; \sigma_\epsilon = 1.3 \tag{3.13}$$

Equations (3.10) and (3.11) have different origins. The k transport equation can be derived directly form *RANS* equations, while the ϵ equation is an empirically-based equation.

ANSYS® Fluent manual gives a more complex definition of model equations [4]. The turbulent kinetic energy equation becomes:

$$\frac{\overline{D}\rho k}{\overline{D}t} = \nabla \cdot \left(\mu + \frac{\mu_T}{\sigma_k}\nabla k\right) + G_k + G_b - \epsilon\rho - Y_M + S_k \tag{3.14}$$

While the rate of dissipation equation becomes:

$$\frac{\overline{D}\rho\epsilon}{\overline{D}t} = \nabla \cdot \left(\mu + \frac{\mu_T}{\sigma_\epsilon}\nabla\epsilon\right) + C_{\epsilon 1}\frac{P\epsilon}{k}(G_k + C_{\epsilon 3}G_b) - C_{\epsilon 2}\rho\frac{\epsilon^2}{k} + S_\epsilon \tag{3.15}$$

Where:

- G_k is the production of k due to the mean velocity gradient;
- G_b is the generation of k due to the buoyancy;
- Y_M is the contribution of the fluctuating dilatation in compressible turbulence to the overall dissipation rate;
- $C_{\epsilon 1}$, $C_{\epsilon 2}$ and $C_{\epsilon 3}$ are constants;
- S_ϵ and S_k are user-defined source terms. None of them have been used within the work;

Stephen B. Pope defined this model as the "simplest complete turbulence model" and regarded it as "the one with the broadest range of applicability" [25].

Other sources in the literature better define the application range of this model. According to *Andersoon et al* (2012) [3], the model has a low accuracy for flows with strong streamline curvature, swirling flows and axisymmetric jets. The k-ϵ standard model has been developed considering the molecular viscosity negligible. This assumption reduces the applicability of the model in fully turbulent flow [4, 17].

3.3.2 K-epsilon RNG model

In order to overcome the limitation of the *standard* k-ϵ model associated with high dissipation of turbulence, the *RNG* k-ϵ model presents an additional source term.

The RNG theory offers an analytically derived PDE that account for low-Reynolds number effects on effective viscosity.

Comparisons between equation 3.11 and equation 3.16 and between equation 3.15 and 3.17 makes it easy to recognize the new terms introduced from the RNG theory [4].

$$\frac{\overline{D}\epsilon}{\overline{D}t} = \nabla \cdot \left(\mu + \frac{\mu_T}{\sigma_\epsilon}\nabla\epsilon\right) + C_{\epsilon 1}\frac{P\epsilon}{k} - C_{\epsilon 2}\frac{\epsilon^2}{k}; \tag{3.16}$$

$$\frac{\overline{D}\rho\epsilon}{\overline{D}t} = \nabla \cdot \left(\alpha_\epsilon\frac{\mu_{eff}}{\sigma_\epsilon}\nabla\epsilon\right) + C_{\epsilon 1}\frac{P\epsilon}{k}(G_k + C_{\epsilon 3}G_b) - C_{\epsilon 2}\rho\frac{\epsilon^2}{k} - R_\epsilon + S_\epsilon \tag{3.17}$$

R_ϵ represents the main difference between equations and models. It induces a smaller destruction of ϵ then standard model for regions with large enough rate of strain. Hence the turbulent viscosity is lower for these regions.

Model constants $C_{\epsilon 1}$ and $C_{\epsilon 2}$ have different values from standard model. Those values are analytically derived by the RNG theory [4, 31].

$$C_{\epsilon 1} = 1.42 \; C_{\epsilon 2} = 1.68 \tag{3.18}$$

3.3.3 K-epsilon Realizable model

In the presence of high mean rate-of-strain, $\frac{\partial\langle \boldsymbol{U}_i\rangle}{\partial x_j}$, the *standard* k-ϵ model presents a not physical behavior. In fact, Reynolds stress tensor normal components (Eq. 1.8) becomes negative:

$$\langle \boldsymbol{u}_i\boldsymbol{u}_i\rangle = \frac{2}{3}k - 2\mu_T\frac{\partial\langle \boldsymbol{U}_i\rangle}{\partial x_j} \leq 0$$

$$if \quad \frac{\partial\langle \boldsymbol{U}_i\rangle}{\partial x_j} \geq \frac{1}{3}\frac{k}{\mu_T}$$

The k-ϵ *Realizable* model introduces a function describing the *standard* model constant C_μ and a change in the ϵ production term of the dissipation rate transport equation. Thus, the model is likely to provide better performance for flow involving rotation and separation.

The constants of the model, except for C_μ, are the same as those of the *standard* k-ϵ model.

3.3.4 Other requirements of the models

Near-wall treatment

k-ϵ models require that the first layer of cells away from the boundary lies in $Y^+ < 1$ [8] in order to properly solve the momentum transport equation.

Hence, the cells dimension needs to be very fine and meshes drawing and models solving can be practically unbearable. In order to avoid this, *Wall Functions* were introduced.

The idea behind wall functions is to put the first-layer-cells center outside the viscous sublayer and makes suitable assumptions on the velocity profile in order to obtain the wall shear stress. Thus, the mesh can be coarser and the first-layer-cells dimension can leads to value of Y^+ ranging between 30 and 300 [5, 6].

Definition of turbulence at the inlet

The final results of computations should be independent on initial guess of turbulence condition, but a better initial guess leads to a faster convergence.

In order to simplify the guessing ANSYS® Fluent allows to define the turbulence parameters, k and ϵ, as:

$$k = 1.5 \left(I \langle U \rangle\right)^2 \tag{3.20}$$

$$\epsilon = C_\mu^{3/4} \frac{k^{3/2}}{l} \tag{3.21}$$

Where:

- l is the mixing length defined as $0.07 \cdot D$ where D is the hydraulic diameter;
- C_μ is a model constant;
- I is the turbulence intensity.

[8] Y^+ is the non-dimensional wall distance defined as in equation 3.19.

$$Y^+ = \frac{\rho y u_\tau}{\mu_w} \tag{3.19}$$

where ρ is the water density, y is the cell characteristic dimension, u_τ is the friction velocity at the wall.

The *Turbulent Intensity* quantifies velocity fluctuations effects (Eq. 3.22). It is defined as the standard deviation, σ_u, of the velocity fluctuation vector, u.

$$\sigma_u = \sqrt{\langle u^2 \rangle} \tag{3.22}$$

It has the units of a velocity. The normalization of the above quantity with the mean velocity, $\langle U \rangle$ leads to the definition of the *Relative Turbulent Intensity*, I, (eq. 3.23)[4].

$$I = \frac{\sigma_u}{\langle U \rangle} = \frac{\sqrt{\langle u^2 \rangle}}{\langle U \rangle} \tag{3.23}$$

3.4 Simulation Geometry

Geometry features like the *distance* among fish and the *shape of the fish body* are important parameters of numerical simulations.

3.4.1 Range of analyzed distances

In section 2.2, pictures 2.7 and 2.8 show a change in the behavior that couples of fish have for given flow velocities. In particular, picture 2.7 shows that, in standing water, fish do not have a preferential swimming configuration, whereas, in moving water, they tend to adjust themselves side by side at a distance of 0.3 body lengths, BL.

In order to evaluate the presence of a hydrodynamic benefit that fish experience by swimming side-by-side at the distance reported above, simulations were planned to adequately describe the fish's drag coefficient variation for a range of distances from 0.2 BL to 1 BL. Figure 3.9 reports the distances investigated in the simulation.

3.4.2 Fishes simulated body

Minnows (Phoxinus phoxinus) shape was simplified following the idea that only the main profile of their bodies has an influence on drag and lift forces.

The shape was simulated as well-known airfoils profile. Selected profiles are symmetrical along the length and respect proportions of fish dimensions. These

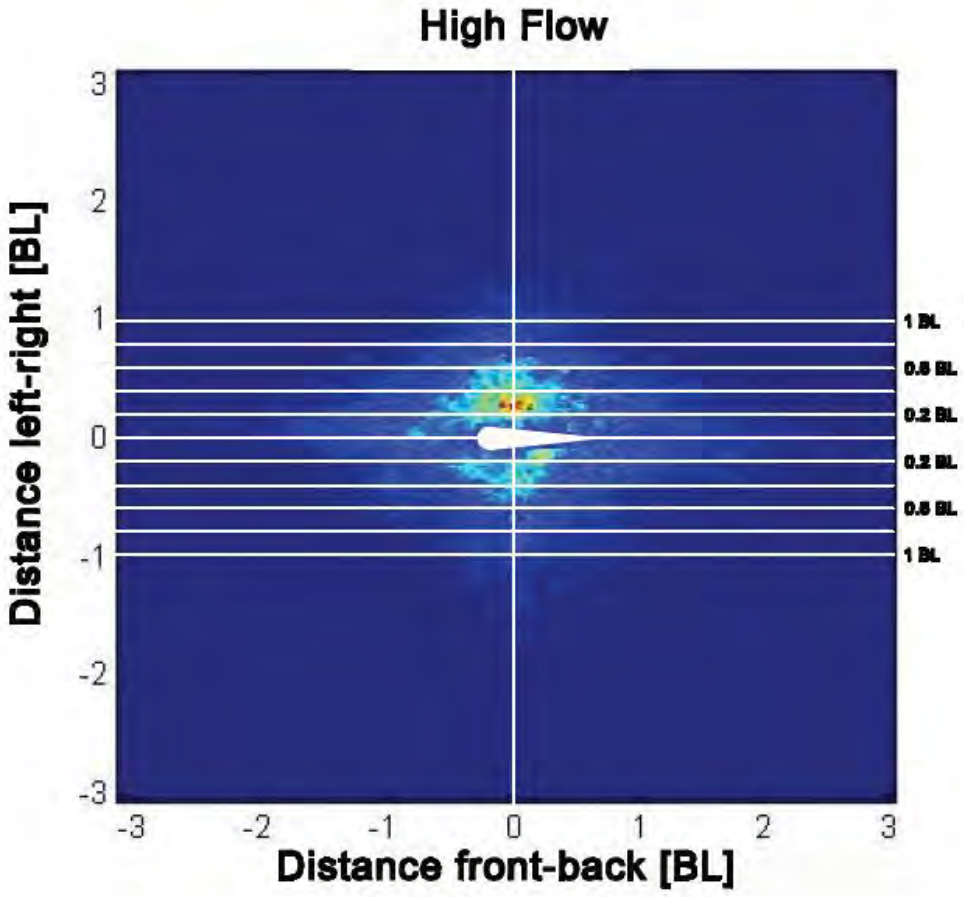

Figure 3.9: Comparison of the focal-fish position with the position of the neighbor fish, which is represented by white horizontal lines in the picture. Numerical simulations were made for distances between animals of 0.2, 0.4, 0.6, 0.8 and 1 body lengths.

average dimensions are: length, 6.6cm, width, 0.6cm, and height, 1cm.

Selected profiles are NACA[9] wing section profiles, which can be described through fixed rules based on a numerical code each section has[10]. The sections numbers are: NACA0009 and NACA0015 (Fig 3.10). These have a maximum width of 9% and 15% of the length. Hence, they are close to fish dimensions.

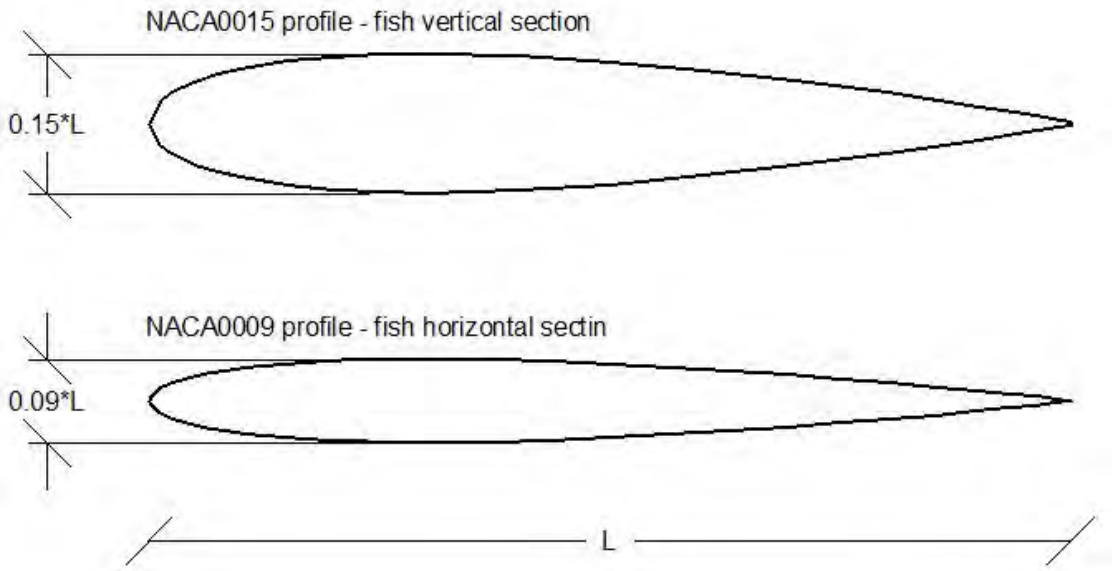

Figure 3.10: Vertical (above) and horizontal (bottom) fish sections drew using NACA 0015 and NACA0009 wing section profiles respectively.

3.5 Sensitivity analysis

The sensitivity analysis is the phase of the model evaluation characterized by the study of how outputs are affected by the change of a single input parameter per time. For the present work, the studied output was the fish drag coefficient.

At the beginning of the work, effects of parameters were studied on the output obtained from the simulation of a square cylinder. This geometry was also used

[9]National Advisory Committee for Aeronautics

[10]First digit of profile number represent the maximum chamber as a percentage of the chord. Second digit describe the distance of the maximum chamber from the airfoil leading edge expressed as tens of percentage of the chord. Last 2 digit represent the width of the profile as a percentage of the chord.

as a test ground to analyze the comprehension of the model behavior.

The elements analyzed during the sensitivity analysis phase are:

- The turbulence model;
- Domain dimensions;
- The mesh type, features and number of cells;
- The turbulence at the inlet.

3.5.1 Turbulence model

Analyzed turbulence models are *k-ϵ RNG* and *Realizable* models, which were described in section 3.3. These model were chosen among others two-equations model because of their good reputation in literature. Other more complex models have been avoided because of the computational power limitation to which this study was subjected. The *standard k-ϵ* model was not considered because of its low accuracy for flows with strong streamline curvature.

The analysis was done utilizing two-dimensional and three-dimensional geometries. Table 3.3 compares two-dimensional simulations results obtained from four geometries, while three-dimensional simulation results are listed in table 3.4. In general, the two models gave similar results for both two-dimensional and three-dimensional numerical simulation. *RNG k-ϵ* model coupled fish results have slightly higher value than the other model results.

Besides, figures 3.11, 3.12 and 3.13 show the difference among models by comparing pictures of coupled fish wakes respectively for: two-dimensional simulation; three-dimensional simulation, top view; three-dimensional simulation, lateral view. Wakes obtained utilizing the *RNG k-ϵ* model are generally longer and with slightly higher turbulent kinetic energy values. The difference is probably given by the rate of dissipation transport equation, which is different for the two model (see section 3.3).

Transient and Steady-State conditions were tested too. This test was conducted on the two-dimensional simulation geometry describing the densest school, 0.2 BL, and was done for the *Realizable k-ϵ* model. Results, computed for 10 seconds of

(a) - *RNG* k-ϵ model

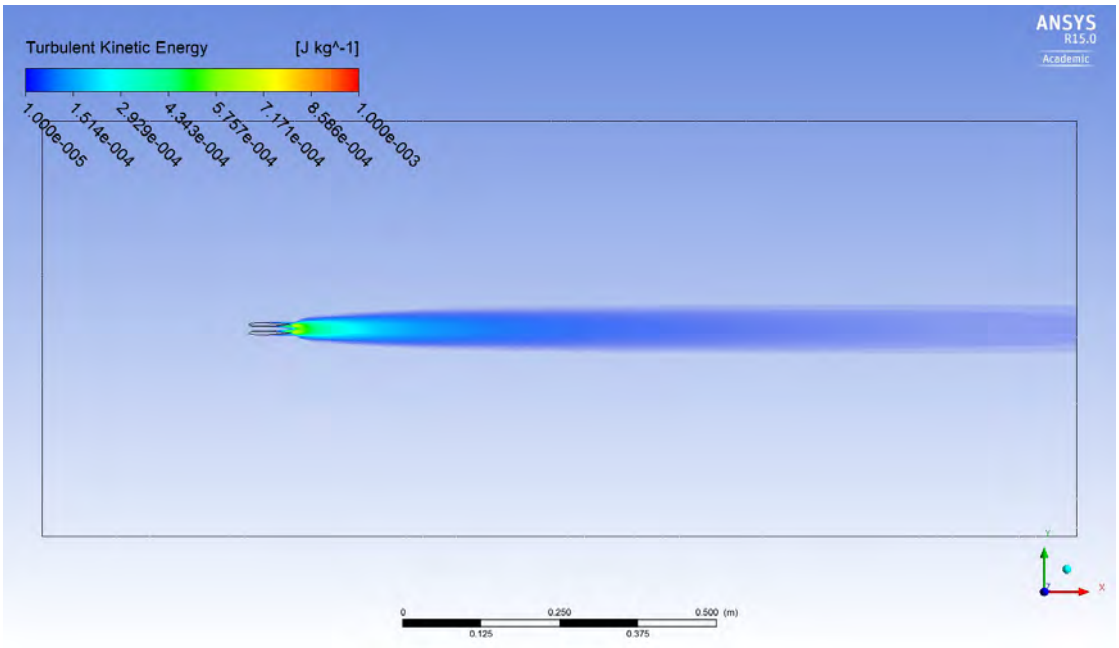

(b) - *Realizable* k-ϵ model

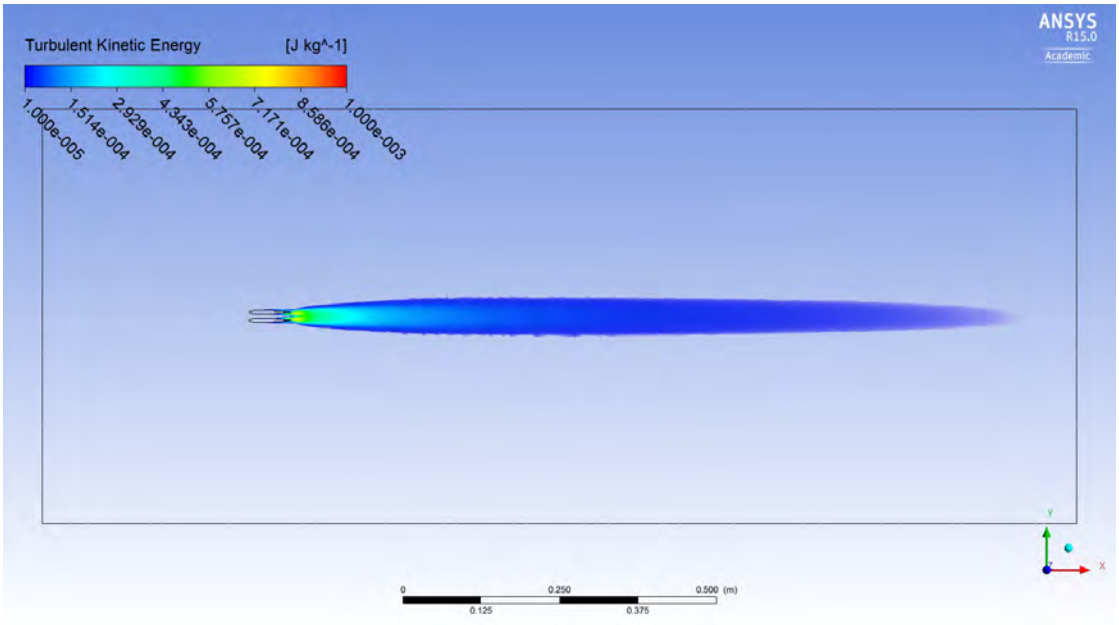

Figure 3.11: (a) wake of coupled fish obtained utilizing the *RNG* k-ϵ model; (b) wake of coupled fish obtained utilizing the *Realizable* k-ϵ model. The two-dimensional simulation geometry utilized was that having fish at 0.2 body lengths apart. The flow zone where the turbulent kinetic energy was greater then 0.00001 was considered fish wake.

(a) - *RNG* k-ϵ model

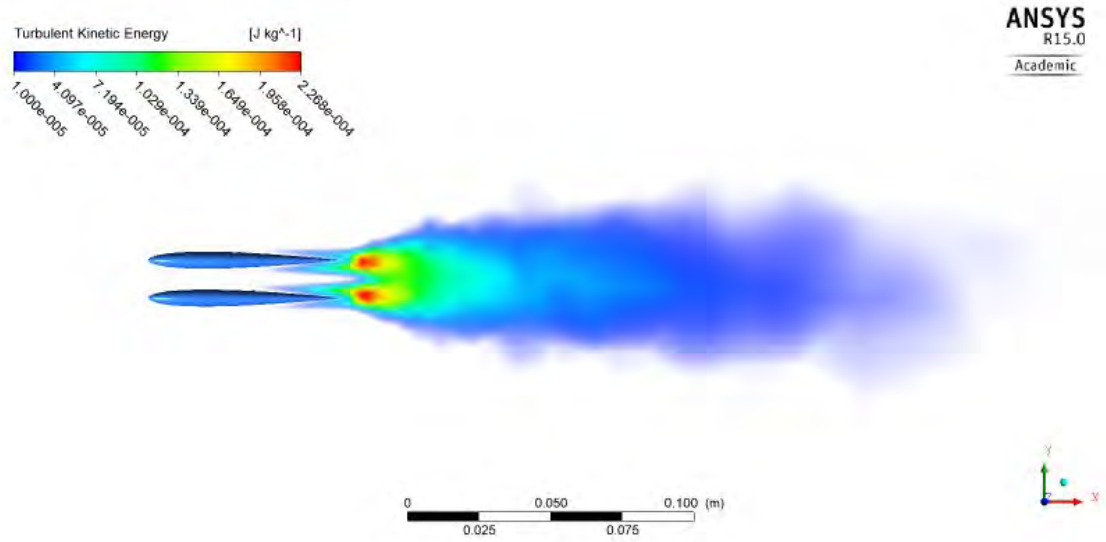

(b) - *Realizable* k-ϵ model

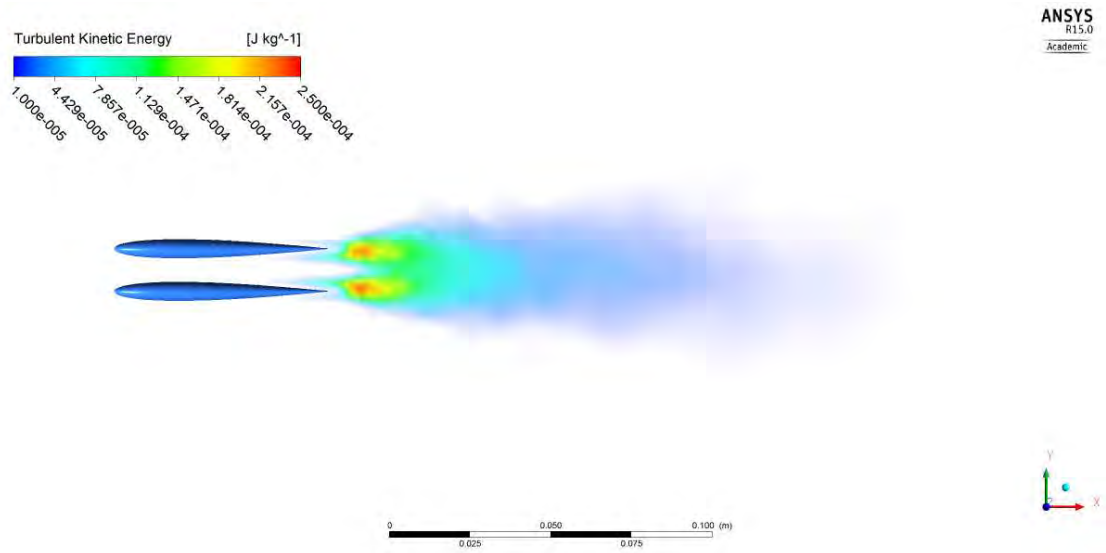

Figure 3.12: (a) top view of coupled fish wake obtained utilizing the *RNG* k-ϵ model; (b) top view of coupled fish wake fish obtained utilizing the *Realizable* k-ϵ model. The three-dimensional simulation geometry utilized was that having fish at 0.2 body lengths apart. The flow zone where the turbulent kinetic energy was greater then 0.00001 was considered fish wake.

(a) - *RNG* k-ϵ model

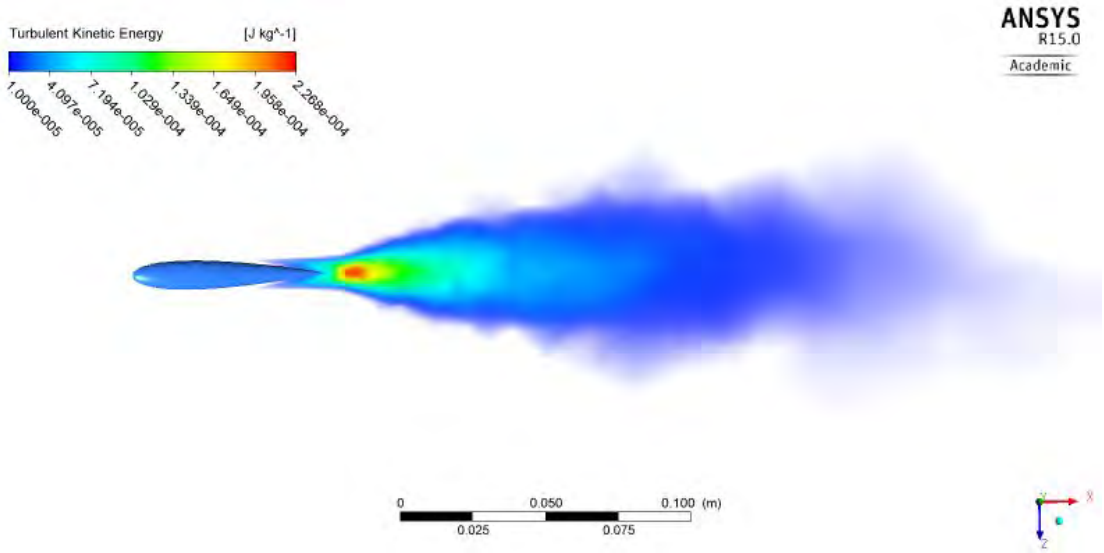

(b) - *Realizable* k-ϵ model

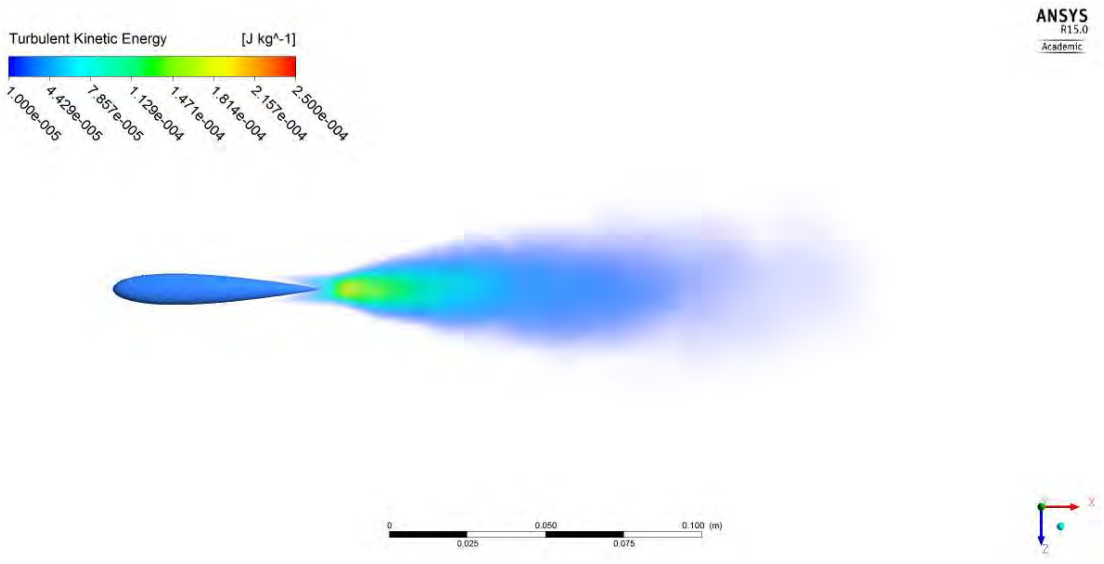

Figure 3.13: (a) lateral view of coupled fish wake obtained utilizing the *RNG* k-ϵ model; (b) lateral view of coupled fish wake obtained utilizing the *Realizable* k-ϵ model. The three-dimensional simulation geometry utilized was that having fish at 0.2 body lengths apart. The flow zone where the turbulent kinetic energy was greater then 0.00001 was considered fish wake.

Drag Coefficient		
$\frac{L}{L_{fish}}$	***RNG* k-ϵ model**	***Realizable* k-ϵ model**
single fish	0.4736	0.4709
0.2	0.6476	0.6497
0.4	0.5444	0.5428
0.8	0.4972	0.4954

Table 3.3: Comparison of Drag Coefficient computed for two-dimensional geometries using k-ϵ *RNG* and *Realizable* models . $\frac{L}{L_{fish}}$ is the distance among fish, which is used to classify the simulation geometries.

Drag Coefficient		
$\frac{L}{L_{fish}}$	***RNG* k-ϵ model**	***Realizable* k-ϵ model**
single fish	0.4260	0.4245
0.2	0.4358	0.4341
0.4	0.4294	0.4275

Table 3.4: Comparison of Drag Coefficient computed for two-dimensional geometries using k-ϵ *RNG* and *Realizable* models . $\frac{L}{L_{fish}}$ is the distance among fish, which is used to classify the simulation geometries.

calculation with a time step of 0.1 seconds, show that there is a very small difference among transient and steady-state results (tab. 3.5), which does not affect the drag force increment order of magnitude, hence, numerical simulations were made by imposing the steady-state condition.

Finally, the study was done utilizing the *Realizable* k-ϵ model, which is slower than the *RNG* k-ϵ model in computations, but was considered the best for fish wake representation.

3.5.2 Domain dimensions

Boundaries and walls greatly affect the flow. Lateral boundary conditions, even if defined as symmetries, constrict the wake and modify the output. Hence, in order to avoid unwanted modification of the flow, boundaries lay at least at 5

Model		$C_{D,dx}$	$C_{D,sx}$	$C_{L,dx}$	$C_{L,sx}$
Transient	average	0.6383	0.6493	-1.2046	1.2786
	minimum	0.6384	0.6494	-1.1947	1.2867
	maximum	0.6372	0.6479	-1.2141	1.2685
Steady-State		0.6383	0.6493	-1.2030	1.2774

Table 3.5: Comparison of drag coefficient computed with transient and steady state numerical simulations. The *Realizable* k-ϵ model was used. Transient results show very small variations (third significant digit) which were considered negligible for the aim of the study.

body lengths far from the obstacle. Nevertheless, the downstream boundary needs to be farther then other boundaries from fish. Figure 3.14 shows two-dimensional simulations fish wakes. In order to obtain reliable results, wake must avoid crossing the downstream boundary line.

The upstream boundary affects the results similarly to the downstream one. It fact, it was noticed that, when the inlet boundary approaches the obstacle (either fishes or square), results are affected by the turbulence of the inlet flow. The inlet turbulence was defined in section 3.3.4.

Domain dimensions take a much more important role for three-dimensional simulations. Larger domains require more cells. Thus, considered the time consumption of solving a greater number of cells, this parameter has been better studied for 3D simulations. However, the difference in solving time of meshes reported in figure 3.15 is small.

In sum, the domain dimensions were, for two-dimensional simulations, 20 BL in the streamwise direction and 11 BL in the direction perpendicular to the flow. For three-dimensional results, z-direction domain dimension was 10 BL. In both cases, fish were placed 5 BL far from upstream and side boundaries.

3.5.3 Mesh

It was hard to adapt a structured type mesh to the geometry of fish. Great curvature of the zone near the nose of the fish impedes to correctly solve the mesh drawing algorithm (Fig. 3.16). Hence, meshes were drawn utilizing the

(a)

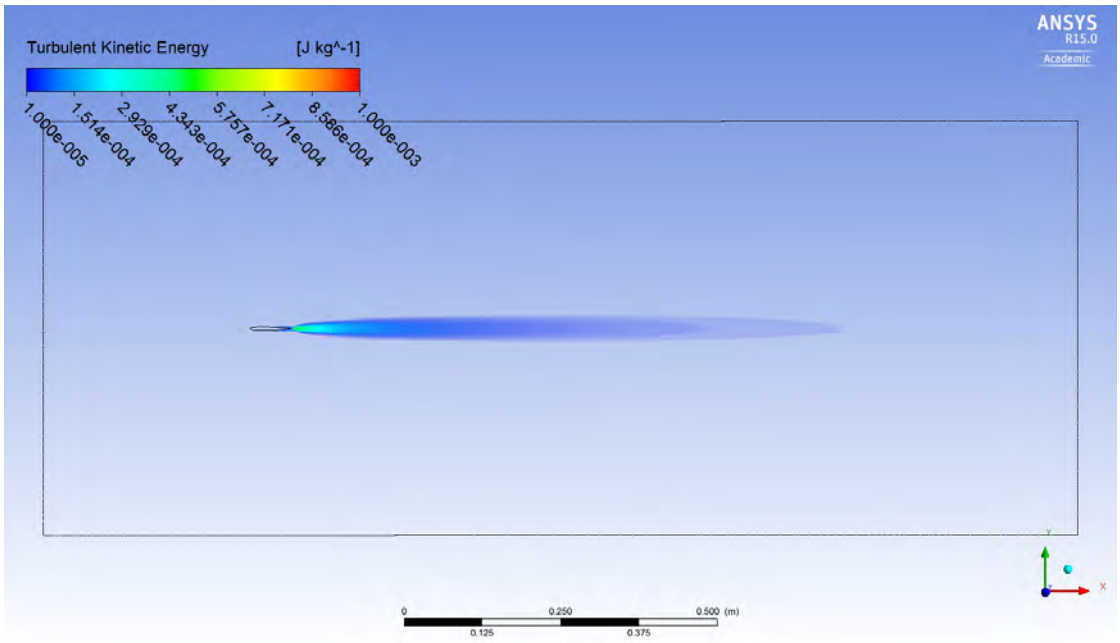

(b)

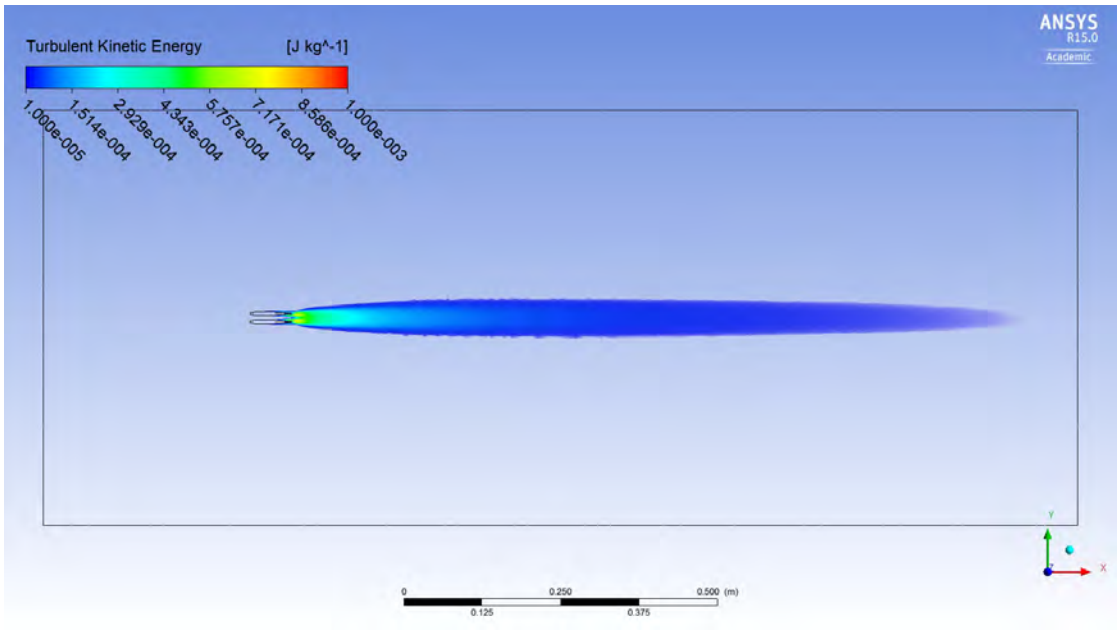

Figure 3.14: (a) wake of a single fish obtained from two-dimensional simulation; (b) wake of coupled fish at 0.2 body lengths apart obtained from two-dimensional simulation. The flow zone where the turbulent kinetic energy was greater then 0.00001 was considered fish wake.

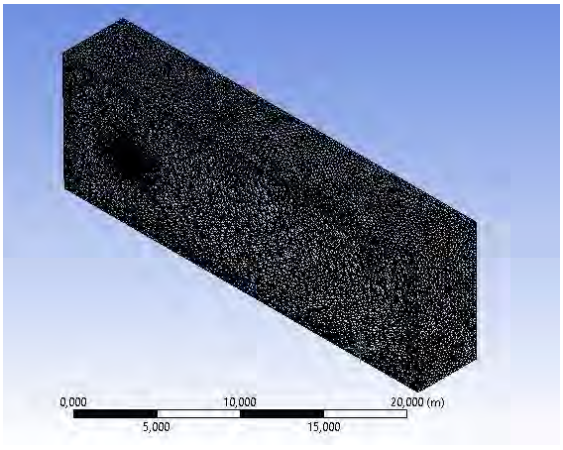

(average C_D= 0.4292)

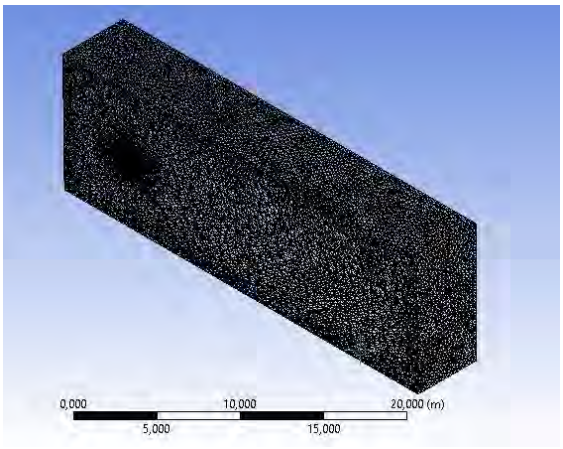

(0.4294)

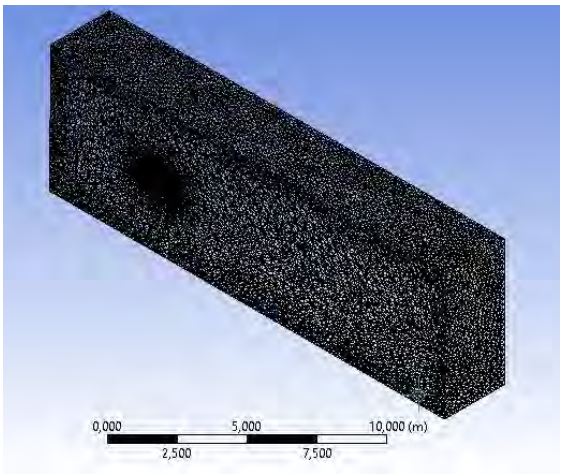

(0.4289)

Figure 3.15: From the top: Mesh with boundaries 5 body lengths, BL, far from fishes; Mesh with the same dimension of the first and a refinement of cells size near fishes; Mesh with lateral boundary 3 BL far from the source of turbulence. The model utilized to evaluate meshes outputs was the *RNG* k-ϵ model.

unstructured mesh algorithm. Nevertheless, first-layers-cells were drawn as shown in figure 3.16 as suggested by ANSYS® Fluent manuals in order to obtain a better condition to solve wall function.

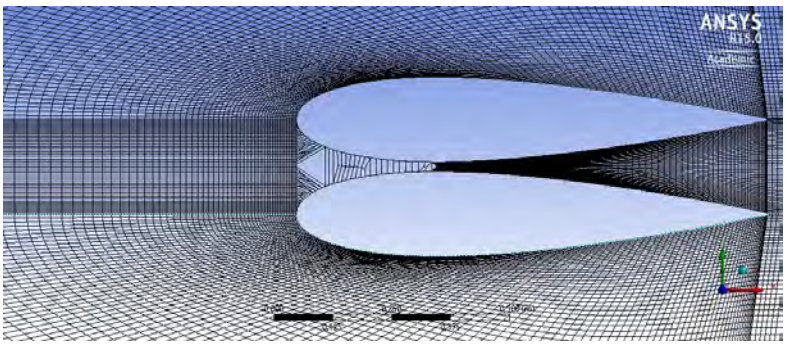

Figure 3.16: Bad structured mesh for fish 0.2 body lengths apart (wrong geometry)

Other then the type of mesh, also the number of cells affect the solution and the time utilized to reach the convergence. Figure 3.19 shows how Drag coefficient value behave with the increasing of cells number. Being the difference between results computed for the 550000 and 1750000 elements mesh relatively small, the simulation geometries meshing was done with 550000 elements mesh settings (Fig. 3.17).

In conclusion, two-dimensional meshes were done imposing the smallest cells of the order of magnitude of $0.0001m$ while biggest of $0.01m$. These value were then scaled with the 0.066 factor used to modify the domain dimension (see section 3.2). Instead, three-dimensional meshes have elements ranging between $0.0025m$ to $1m$. This increasing of cells dimensions was related to the computation feasibility. In both case, the growth rate of cells[11] was imposed to be 1.05 and the first layers cells was created with the *Inflation* algorithm described in ANSYS® Fluent manuals.

3.5.4 Turbulence at the inlet

Being the turbulence at the inlet defined through the turbulence intensity, I, and through the hydraulic diameter, D, as seen in section 3.3.4 and being D a constant of the simulation geometry, the analyzed parameter becomes I.

[11] The cells growth rate is the ratio of the next cell sides versus those of the present cell.

(a)

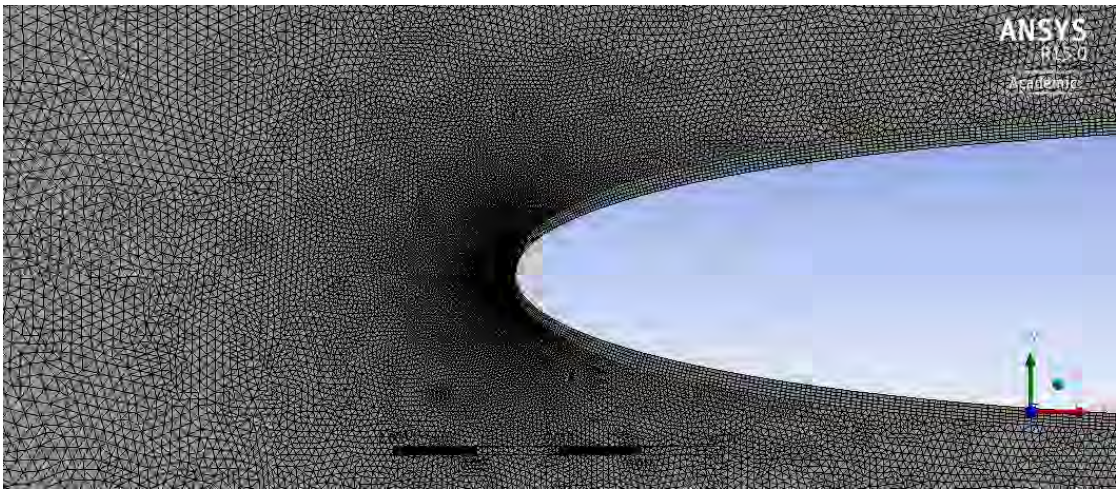

(b)

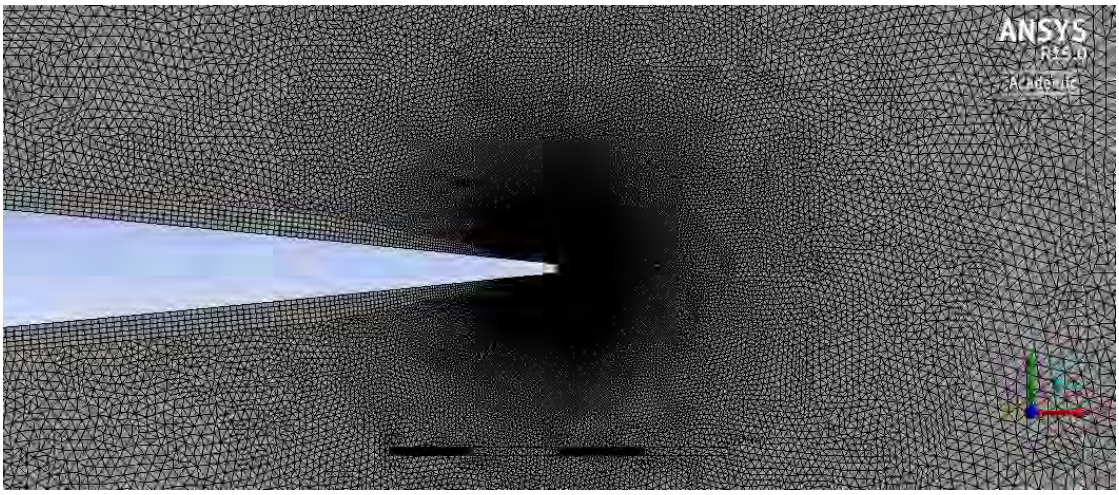

Figure 3.17: (a) 550'000 elements mesh, fish nose; (b) 550'000 elements mesh, fish tail.

(270′000 cells)

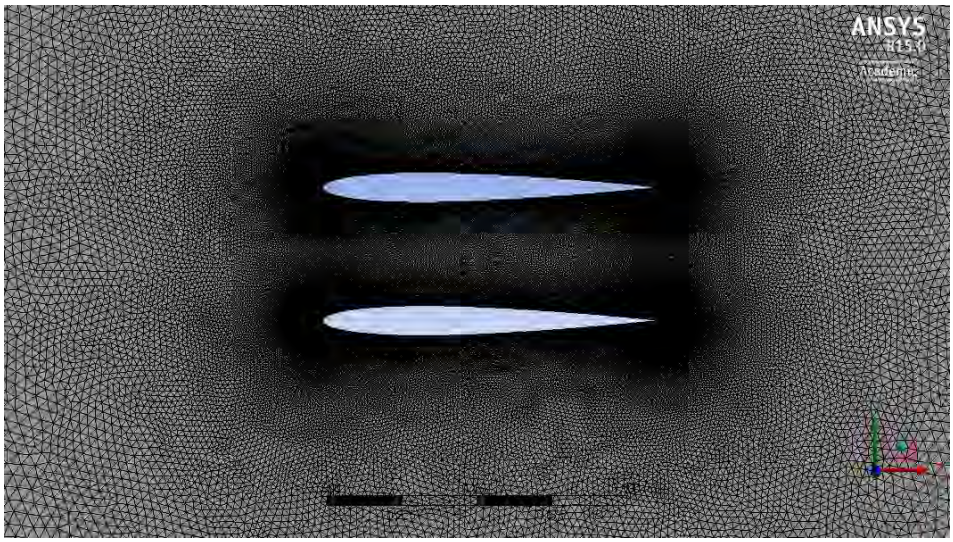

(550′000 cells)

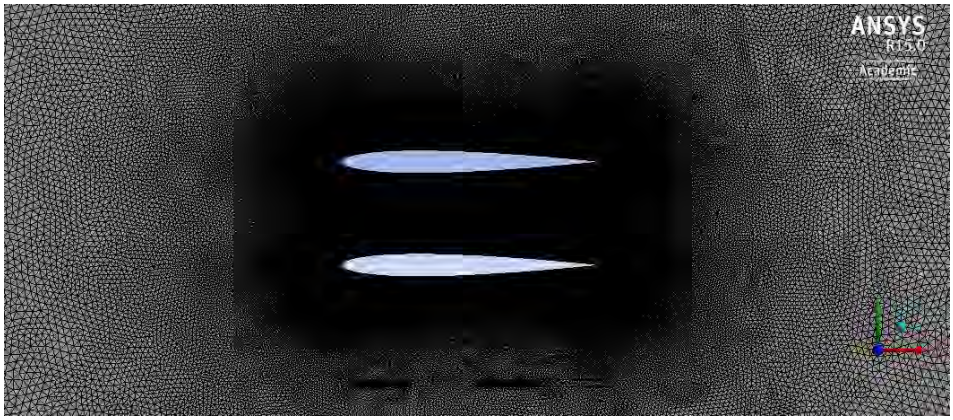

(1′750′000 cells)

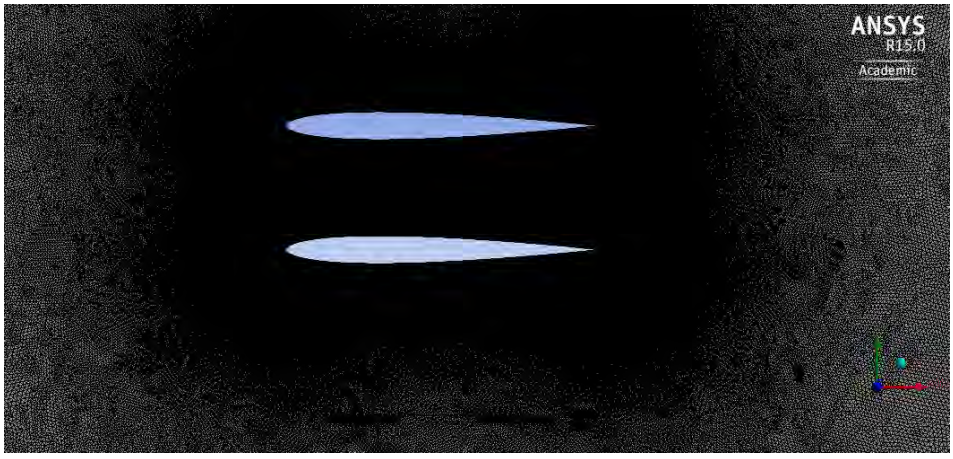

Figure 3.18: Comparison of meshes used to obtain results exposed in figure 3.19. From the top: 270000 elements mesh; 550000 elements mesh; 1750000 elements mesh.

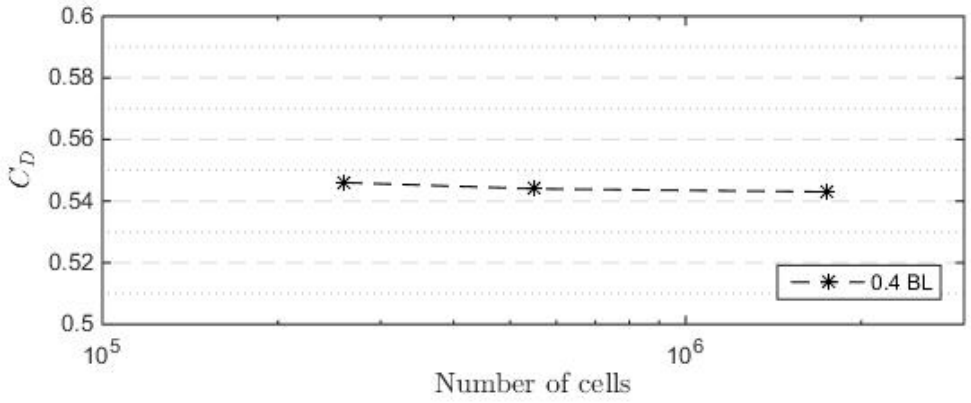

Figure 3.19: Effect of mesh number of cells on drag coefficient. The test case was the two-dimensional simulation geometry having fish at 0.4 body length apart. Mesh used for these numerical simulation are reported in figure 3.18. The model used in order to obtain these results was the *RNG* k-ϵ model.

The turbulence intensity effects are related to the domain dimension. In particular, the distance between the inlet boundary and fish affects the computed value. If the boundary is far enough, effects of I can be seen only for a limited number of iterations, while the final result shows very small variations (Fig. 3.20). The value chose to be used for simulations is $I = 2\%$.

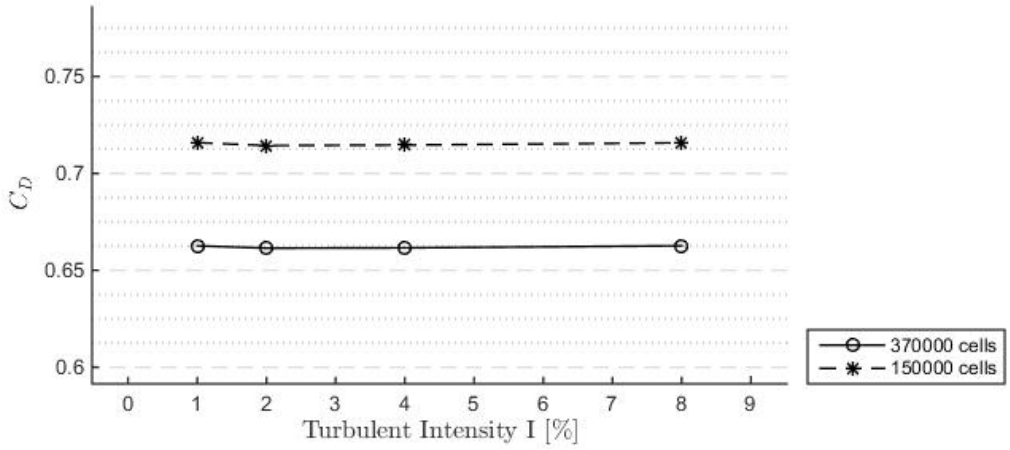

Figure 3.20: Effect of Turbulent Intensity, I, on the fish drag force. Dots and asterisks are associated with two different mesh size as reported in the legend. The single fish geometry were the one analyzed for both the two series.

3.6 Simulations summary

Table 3.6 reports all useful results obtained during model evaluation phase. Together with those used to obtain reported results, other simulation were done, e.g. transient simulation (tab. 3.5) and mesh evaluation simulations (fig. 3.19), whose results were not reported here.

	Drag coefficient on fish				
	RNG k-ϵ model		*RNG k-ϵ model*		
$\frac{L}{L_fish}$	$2D^+$	$3D^*$	$2D^+$	$3D^*$	$3D^\bullet$
Single fish	0.4709	0.4245	0.7436	0.4260	0.4260
0.2	0.6383	0.4341	0.6476	0.4358	0.4355
0.4	0.5427	0.4277	0.5444	0.4292	0.4294
0.6	0.5086	0.4246	0.5110	0.4263	0.4262
0.8	0.4954	0.4255	0.4972	0.4272	0.4277
1	0.4930	0.4253	0.4900	0.4247	0.4254

Table 3.6: Results obtained from simulations. $^+$ refers to two- dimensional meshes defined to have about 550'000 elements (fig. 3.18); * refers to three-dimensional meshes shown in figure 3.15 top picture; ^{*2} refers to three-dimensional meshes shown in figure 3.15 middle picture. $\frac{L}{L_{fish}}$ is the dimensionless distance among fish.

Chapter 4

Results

4.1 Two-dimensional numerical simulations results

Table 4.1 shows the results obtained from two dimensional numerical simulations. Drag and lift forces on fish increase with the reduction of the distance among animals. In particular, the drag coefficient goes from a value of 0.471 for the single fish simulation to a value of 0.649 for the simulation where the distance between fish, expressed as a fraction of the fish body length, $\frac{L}{l_{fish}}$, is 0.2. Thus, the increments of the drag coefficients is about 37% of that computed for the single fish. However, increments of the lift force are much greater than those of the drag force. In fact, the modulus of the lift force increases to more than three times the value of the drag force computed for the single fish. Figures 4.2 and 4.3 show the behavior of drag and lift forces versus the drag force computed for a single fish. According to these results the total force, sum of the lift and the drag forces, acting on fish and its angle, α, increase with decreasing the distance. A scheme of simulations elements and forces acting on fish is showed in figure 4.1.

The lift force a fish experiences is directed towards the other member of the school. This is due to the difference in pressure between left and right surfaces of fish body. Following the Bernoulli equation[1], velocity and pressure are related.

[1] $\left(h + \frac{v^2}{2g} + \frac{p}{g\rho} = constant\right)$ where h is the elevation, v is the flow velocity, g is the gravity acceleration, ρ is the water density and p is the pressure.

$\frac{L}{l_{fish}}$	**Cd of the right fish**	**Cd of the left fish**	**Cl of the right fish**	**Cl of the left fish**
single fish	0.4709		-0.0015	
0.2	0.6383	0.6493	−1.2030	1.2774
0.4	0.5427	0.5430	−0.6605	0.6730
0.6	0.5086	0.5282	−0.1921	0.1650
0.8	0.4954	0.5107	−0.0441	0.0.013
1	0.4930	0.4970	−0.0041	0.0089

Table 4.1: Drag coefficient of fish from two-dimensional simulations. $\frac{L}{L_{fish}}$ is the dimensionless distance among fish.

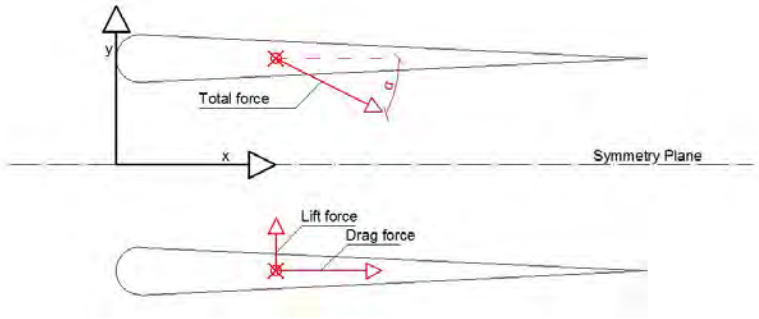

Figure 4.1: Schematics of simulations elements and forces acting on fish.

Wakes comparison gives an idea on the reasons why the drag coefficient increases with the reduction of the distance among fish. Figures 4.4 and 4.5 show the comparison of wakes obtained from two-dimensional simulations. In particular, by comparing figures pictures (b) and (d), which show fish wakes for distances among animals of 0.2 BL and 0.8 BL respectively, modifications of wakes length and of the turbulent kinetic energy are noticeable. In fact, the reduction of the distance among fish induced an increment of the turbulent kinetic energy, which is a signal of the velocity fluctuations augmentation, and elongated the wake in the direction of the flow. Figure 4.4 (c) shows the effect of the fish coupling to the flow. In fact, near fish tail, on the internal side, there is the beginning of the formation of the turbulence responsible of the great augmentation of lift and drag forces.

Figure 4.6 compares flow velocity magnitude near fish. The velocity of the flow

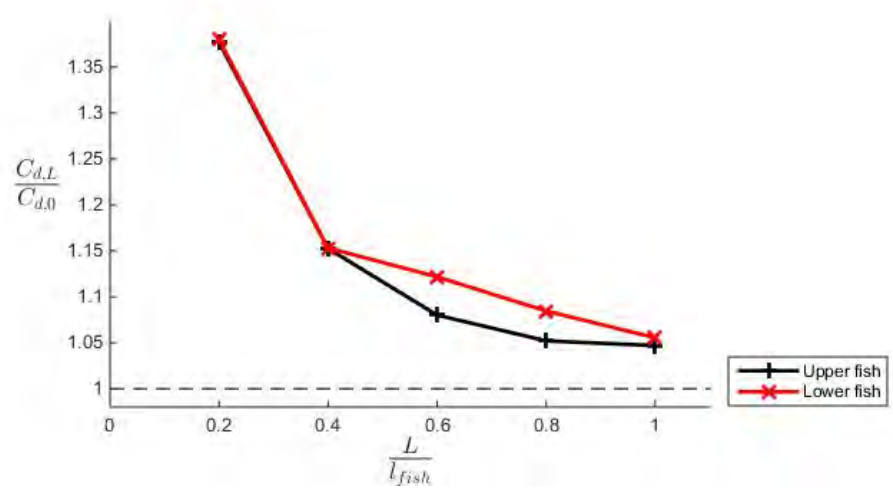

Figure 4.2: Behaviour of Drag coefficient of fishes calculated through 2D simulations. The picture show a the behavior of the ratio between side-by-side and single fish drag coefficient, $\frac{C_{d,L}}{C_{d,O}}$, versus the dimensionless distance among fish, $\frac{L}{L_{fish}}$. The scattering among upper and lower fish results are due to unevenness in the mesh.

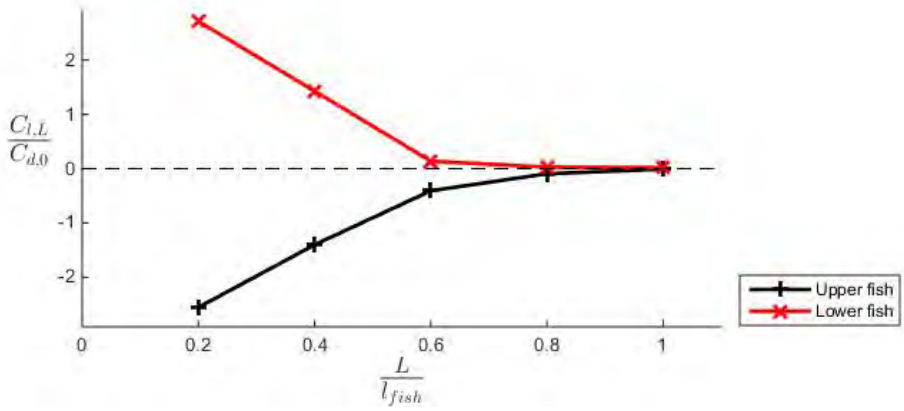

Figure 4.3: Behaviour of Lift coefficient of fishes calculated through 2D simulations. The picture show a the behavior of the ratio between side-by-side fish lift coefficient and the single fish drag coefficient, $\frac{C_{l,L}}{C_{d,O}}$, versus the dimensionless distance among fish, $\frac{L}{L_{fish}}$. The scattering among upper and lower fish results are due to unevenness in the mesh.

among animals increases with the reduction of the distance between them. This behavior of the flow velocity remembers the behavior inducing the base bleed

(a) - single fish geometry

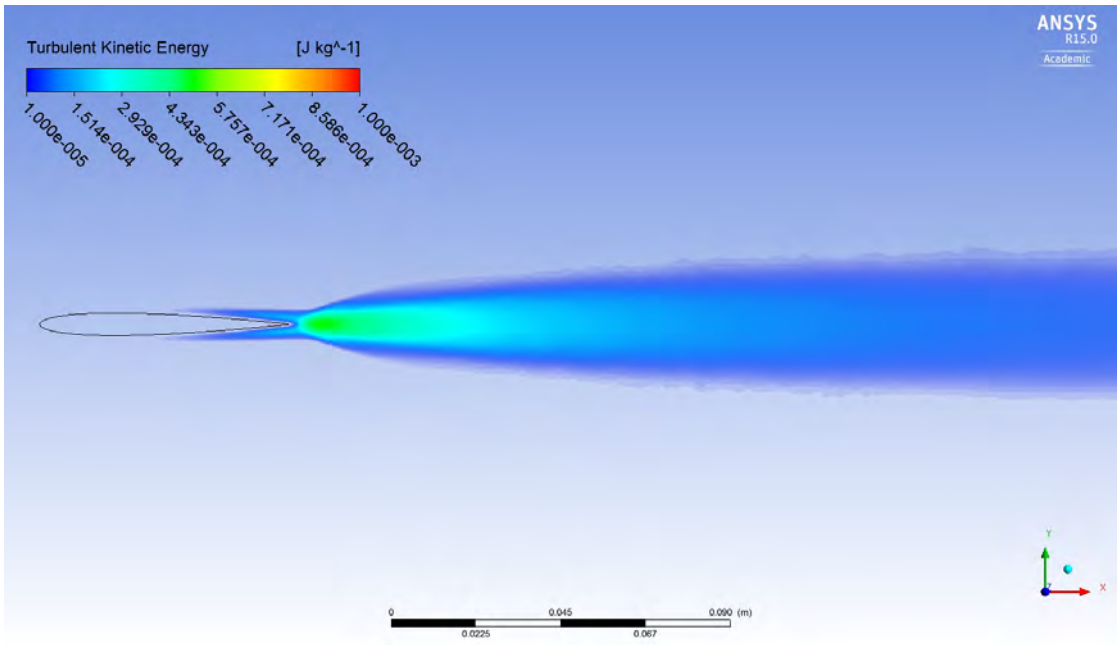

(b) - 0.2 BL geometry

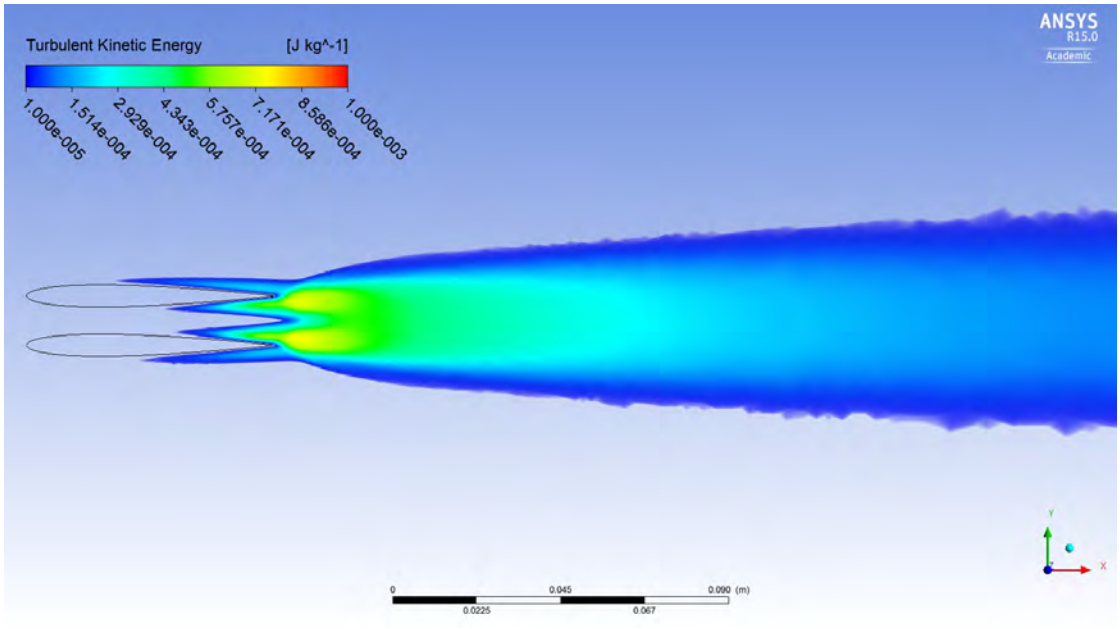

Figure 4.4: Comparison of fish wakes from two-dimensional simulations, close view. (a) single fish wake; (b) 0.2 body lengths, BL, apart fish; (c) 0.4 BL; (d) 0.8 BL. Continues on the next page.

(c) - 0.4 BL geometry

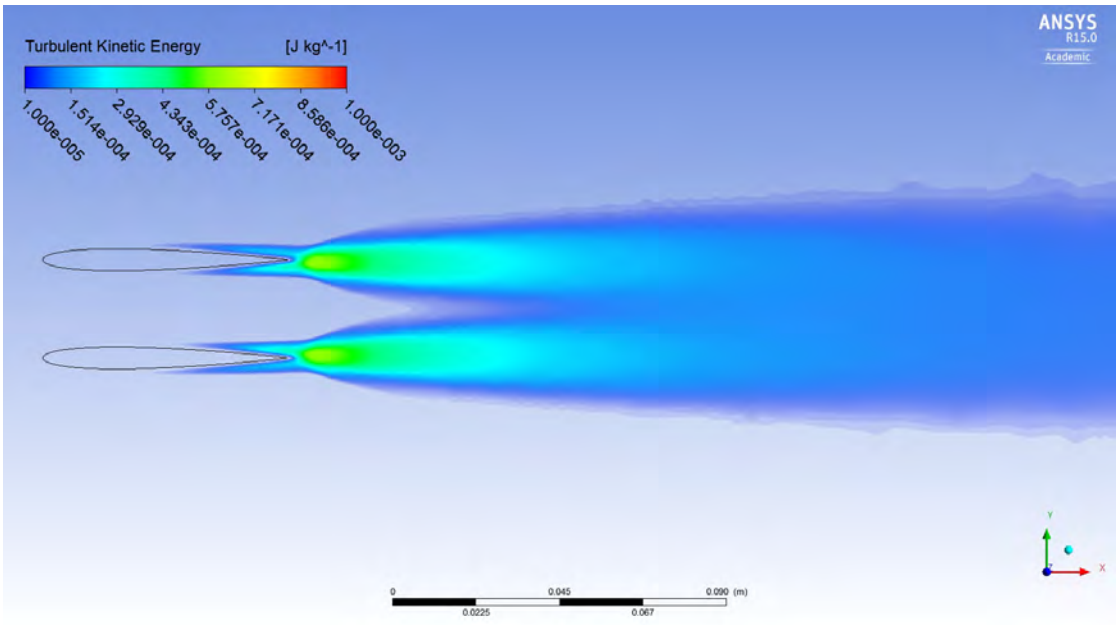

(d) - 0.8 BL geometry

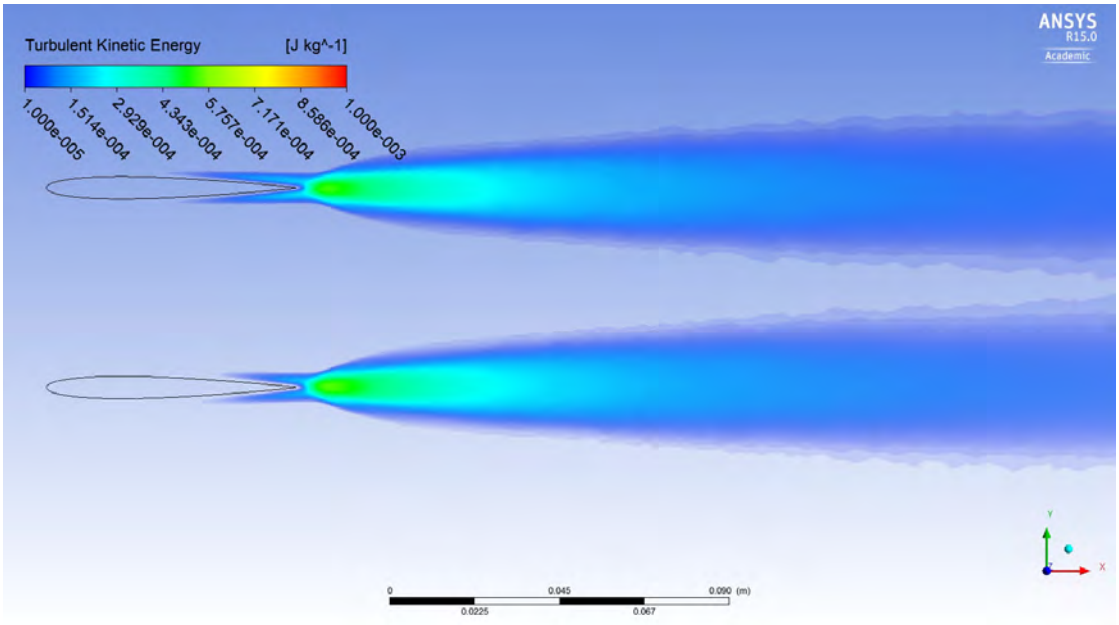

Continued from previous page.

(a) - single fish geometry

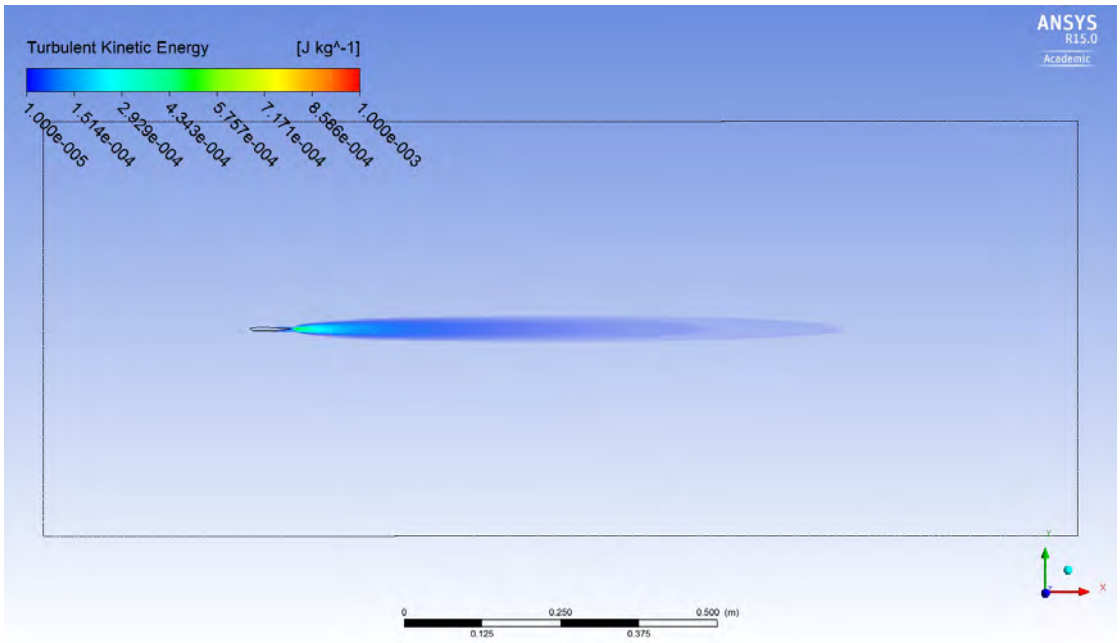

(b) - 0.2 BL geometry

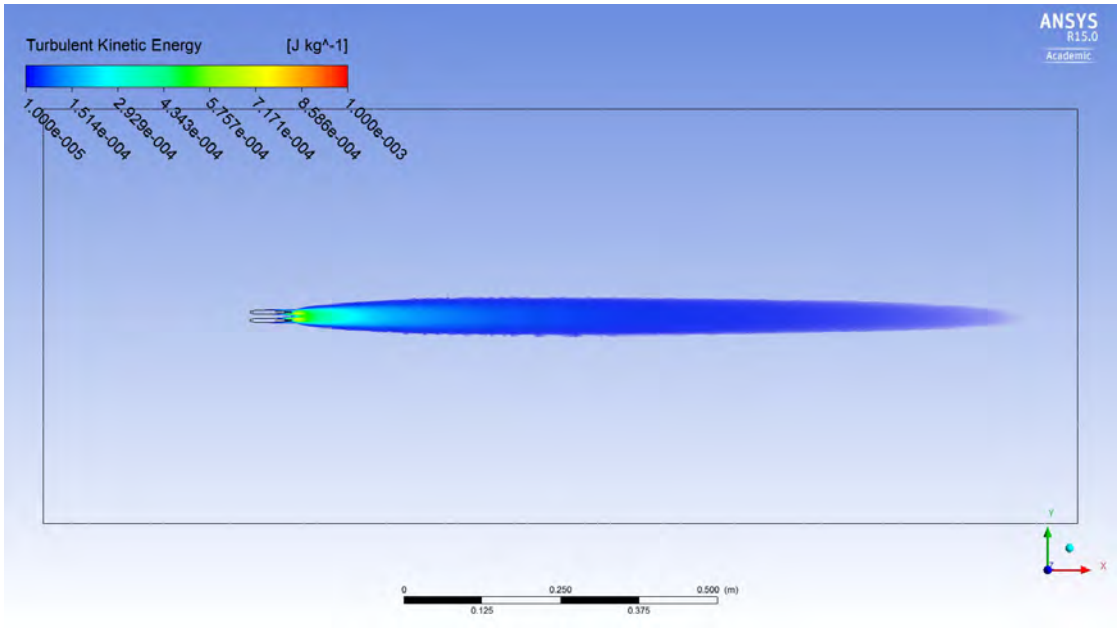

Figure 4.5: Comparison of fish wakes from two-dimensional simulations, far view. (a) single fish wake; (b) 0.2 body lengths, BL, apart fish; (c) 0.4 BL; (d) 0.8 BL. Continues on the next page.

(c) - 0.4 BL geometry

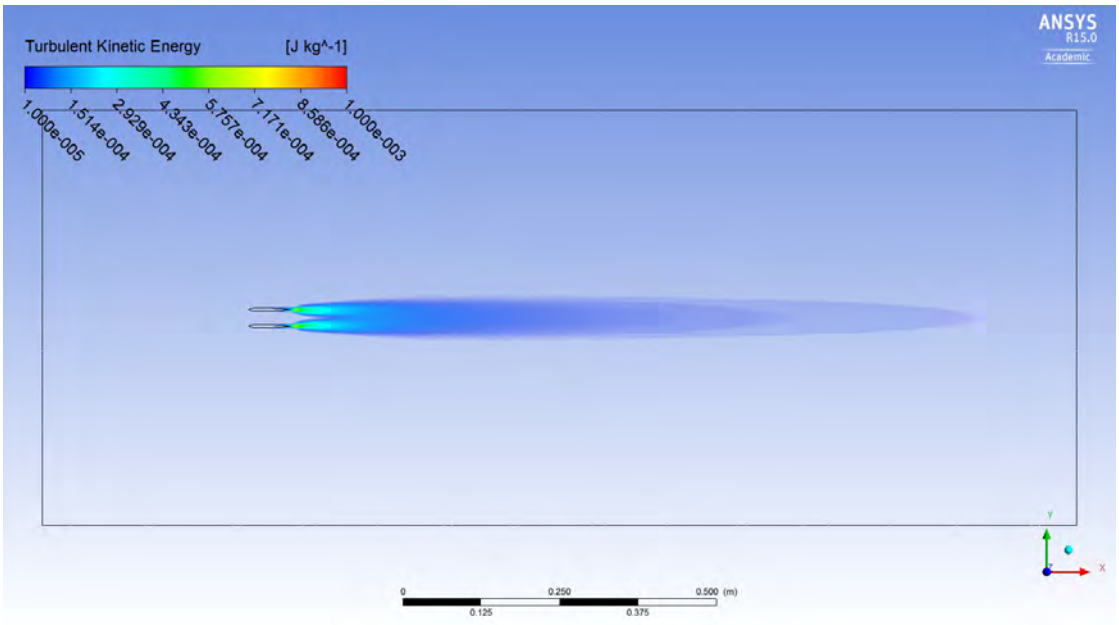

(d) - 0.8 BL geometry

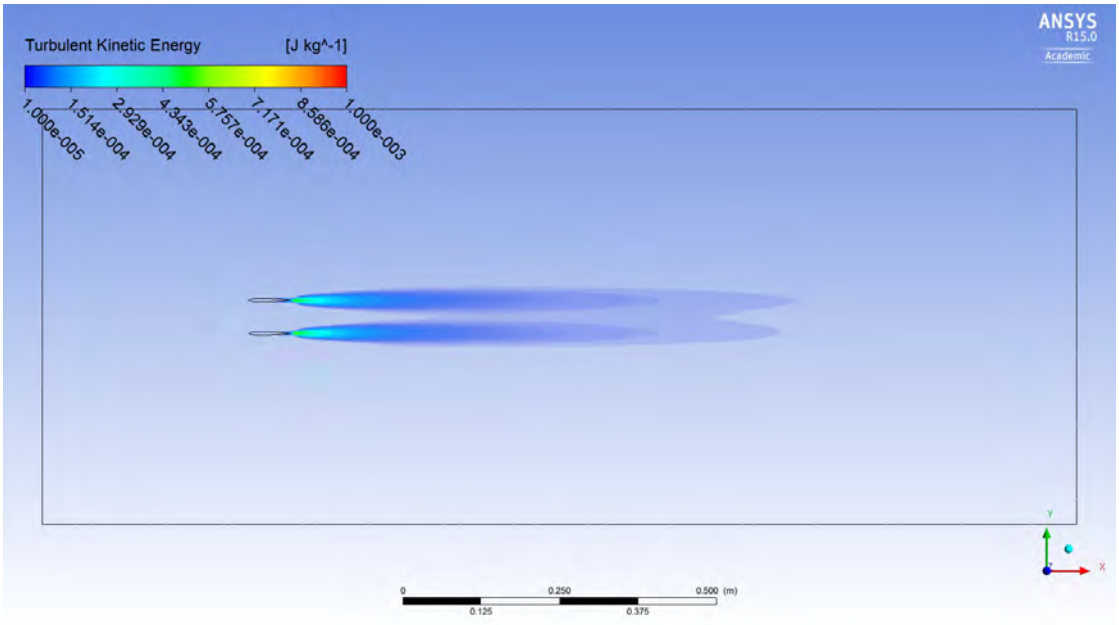

Continued from previous page.

effect on circular cylinder couples in side-by-side configuration. However, this phenomenon occurs to circular cylinder when they are closer than 1.2 T/D [2], while the distance among fish for the densest school simulated, measured as the ratio of the distance versus the fish width in the largest section, is 2.22.

This value, if computed for circular cylinders, places the wakes behavior among those related to the proximity effect. However, the comparison of the percent augmentation of the fish drag force in the densest school configuration, 37%, to that of a couple of circular cylinders at the same distance (fig. 1.2) shows a greater increasing in the drag force of fish. Hence, the airfoils profile might has a role in inducing this augmentation.

4.2 Three-dimensional numerical simulation results

Three-dimensional numerical simulations results are reported in table 4.2. As for two-dimensional simulations, drag and lift coefficients value increases with the reduction of the distance among fish. However, the increments is much lower. In fact, the densest school fish drag coefficient is only 2.26% grater then that of the single fish. The variation of the drag coefficient value with the reduction of the distance is shown in figure 4.7.

For the same school, the lift coefficient increased up to be 9.78% of the drag force acting the single fish. Figure 4.8 shows lift coefficient behavior versus the distance between fish. The direction of the lift force acting on a fish belonging to one of the studied schools is the same as it was for two-dimensional simulations. Hence, it is directed towards the other fish. Nevertheless, being the lift force less then ten percent of the drag force, the angle α (fig. 4.1) is smaller than what was for two-dimensional simulations.

Figure 4.9 shows how the static pressure on fish change with the decreasing of the distance among them. In particular, the single fish experiences lower pressures than coupled fish. This is due to the increased resistance that fish represent for

[2] where T is the distance among cylinders center of mass and D is the cylinders diameter (see sec. 1.2)

(a) - 0.2 BL geometry

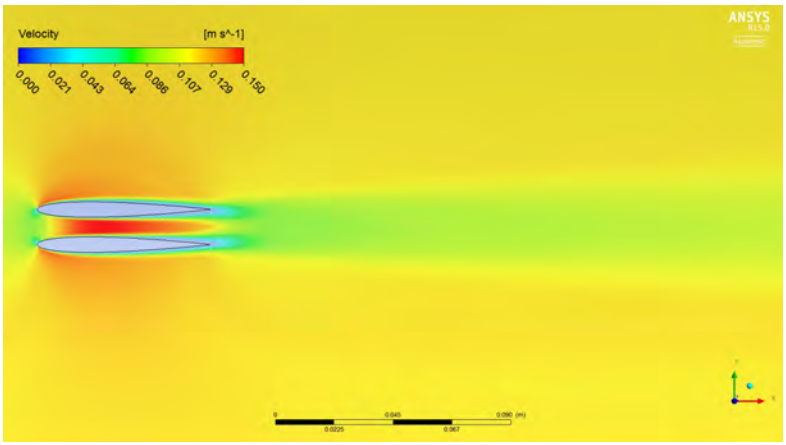

(b) - 0.4 BL geometry

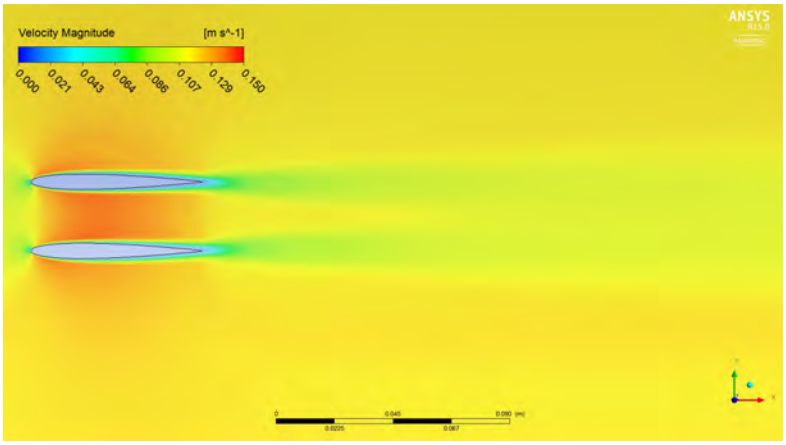

(b) - 0.8 BL geometry

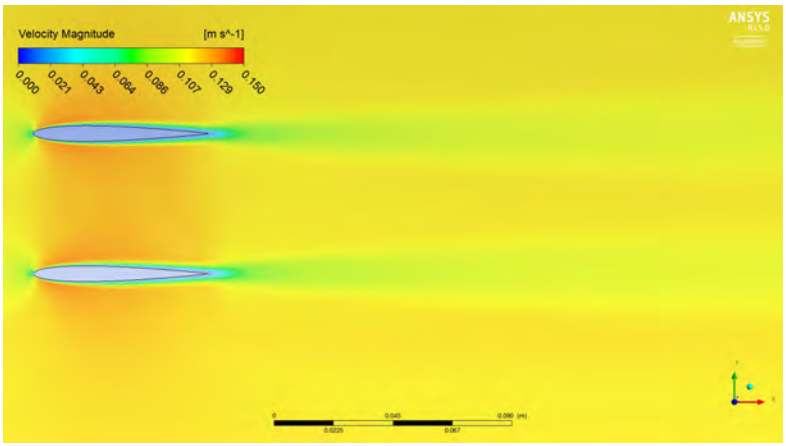

Figure 4.6: Comparison flow velocity near fish from two-dimensional simulations. (a) 0.2 body lengths, BL, apart fish; (b) 0.4 BL; (c) 0.8 BL.

$\frac{L}{l_{fish}}$	**Cd of the right fish**	**Cd of the left fish**	**Cl of the right fish**	**Cl of the left fish**
single fish	0.4245		-0.0002	
0.2	0.4341	0.4340	−0.0415	0.0415
0.4	0.4277	0.4272	−0.0096	0.0096
0.6	0.4246	0.4254	−0.0005	0.0033
0.8	0.4255	0.4249	−0.0034	0.0015
1	0.4253	0.4251	−0.0008	0.0003

Table 4.2: Drag coefficient of fish from three-dimensional simulations. $\frac{L}{L_{fish}}$ is the dimensionless distance among fish.

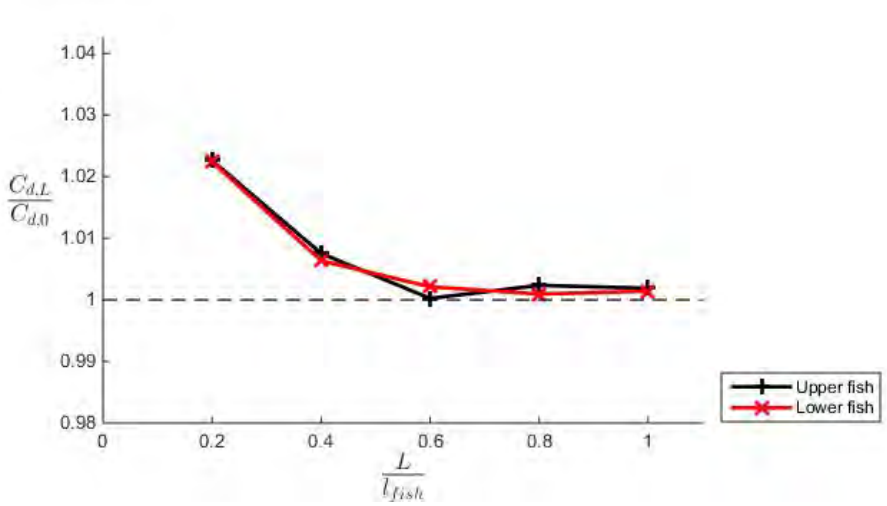

Figure 4.7: Behaviour of Drag coefficient of fishes calculated through three dimensional numerical simulations. The picture show a the behavior of the ratio between side-by-side and single-fish drag coefficient, $\frac{C_{d,L}}{C_{d,O}}$, versus the dimensionless distance among fish, $\frac{L}{L_{fish}}$. The scattering among upper and lower fish results are due to unevenness in the mesh.

water. The comparison of figures 4.9 (b) and (c) with figure 4.9 (a) show a rotation of pressure distribution around fish induced by the difference in flow velocity.

Figures 4.10 and 4.11 show fish wake for the single fish and for couples of 0.2 BL and 0.4 BL detached fish. These present the same wake behavior occurring for two-dimensional simulations results. Hence, the turbulent kinetic energy and the wake

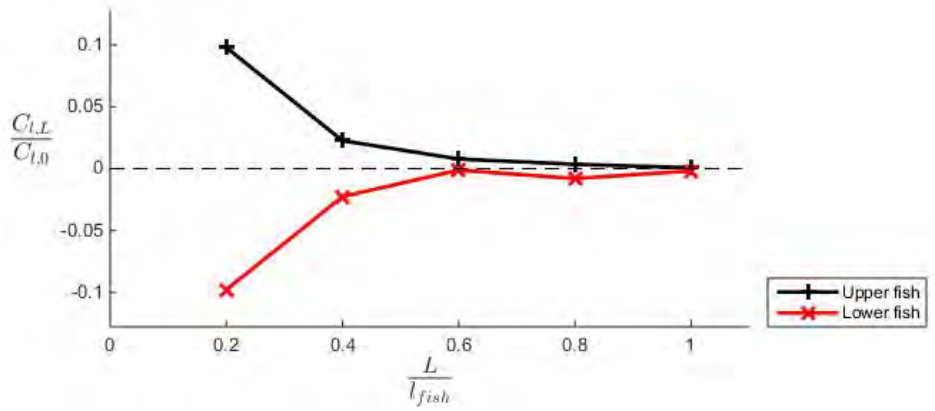

Figure 4.8: Behaviour of Lift coefficient of fishes calculated through three-dimensional numerical simulations. The picture shows the behavior of the ratio between side-by-side fish lift coefficient and the single-fish drag coefficient, $\frac{C_{l,L}}{C_{d,O}}$, versus the dimensionless distance among fish, $\frac{L}{L_{fish}}$. The scattering among upper and lower fish results are due to unevenness in the mesh.

length increase with the reduction of the distance among fish. However, three-dimensional simulations wake are much smaller than those of two-dimensional simulations. This difference is due to the introduction of the third dimension, which helps in the turbulence dissipation.

The third dimensions might avoid the formation of the base bleed phenomenon. In fact, the flow velocity between fish, showed in figure 4.12 (b), gives the idea that the flow dissipate energy by creating turbulence.

4.3 Numerical simulations results discussion

Numerical simulations give no evidence of a hydrodynamic benefit arising from the proximity among fish.

Two-dimensional coupled-fish simulations show a great augmentation of both drag and lift forces with the reduction of the distance among them. Still, according to three-dimensional simulations results, coupled fish experience higher forces than the single fish, but forces increments are one order of magnitude lower than those of two-dimensional simulations. Figure 4.13 show drag coefficient variation as the ratio over single fish drag coefficient. Results are fitted with power law curves. The

(a) - Single fish

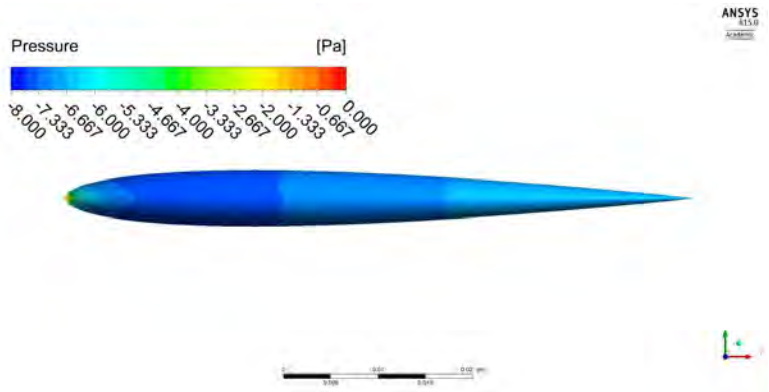

(b) - 0.2 BL

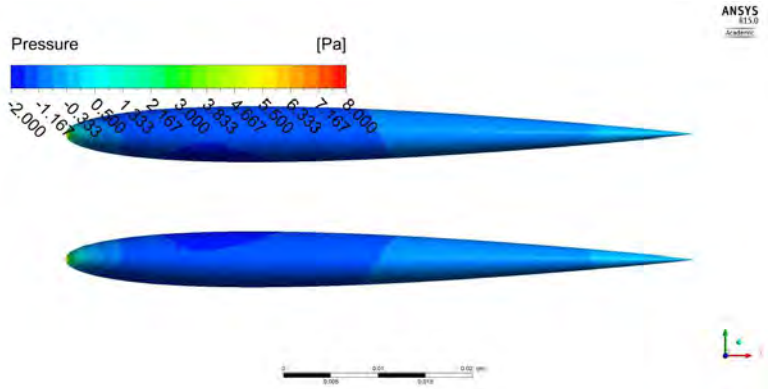

(a) - 0.4 BL

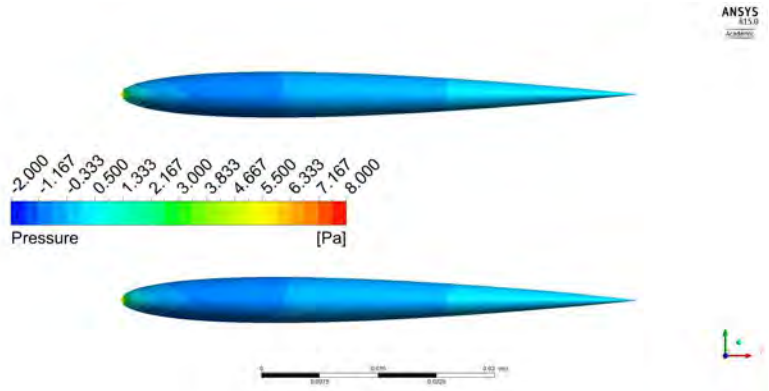

Figure 4.9: (a) static pressure distribution on a fish swimming alone; (b) static pressure distribution on fish 0.2 body lengths, BL, apart; (c) static pressure distribution on fish 0.2 BL. Closer are fish, higher lower the miminum pressure becomes,

(a) - single fish geometry

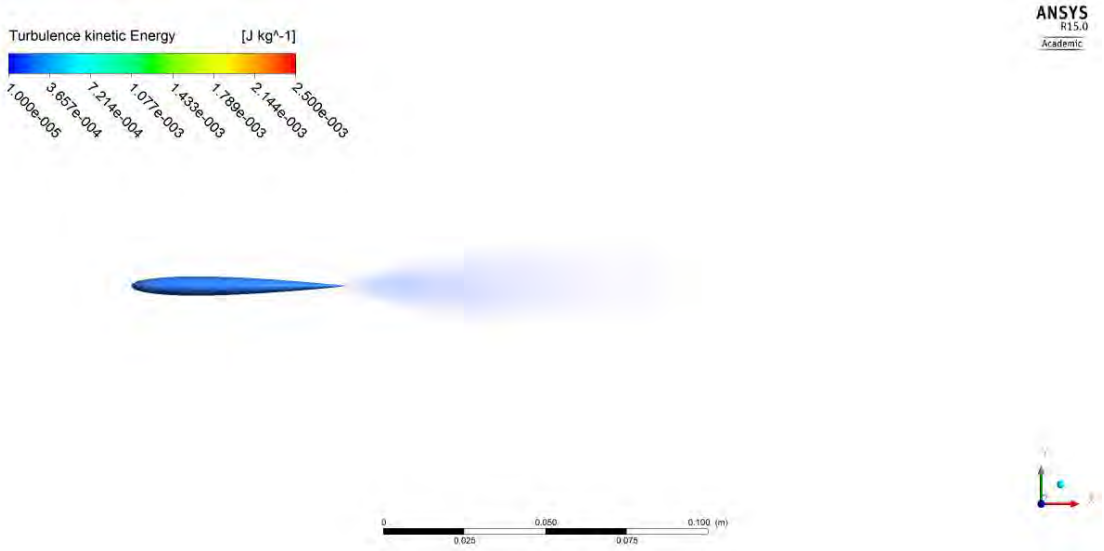

(b) - 0.2 BL geometry

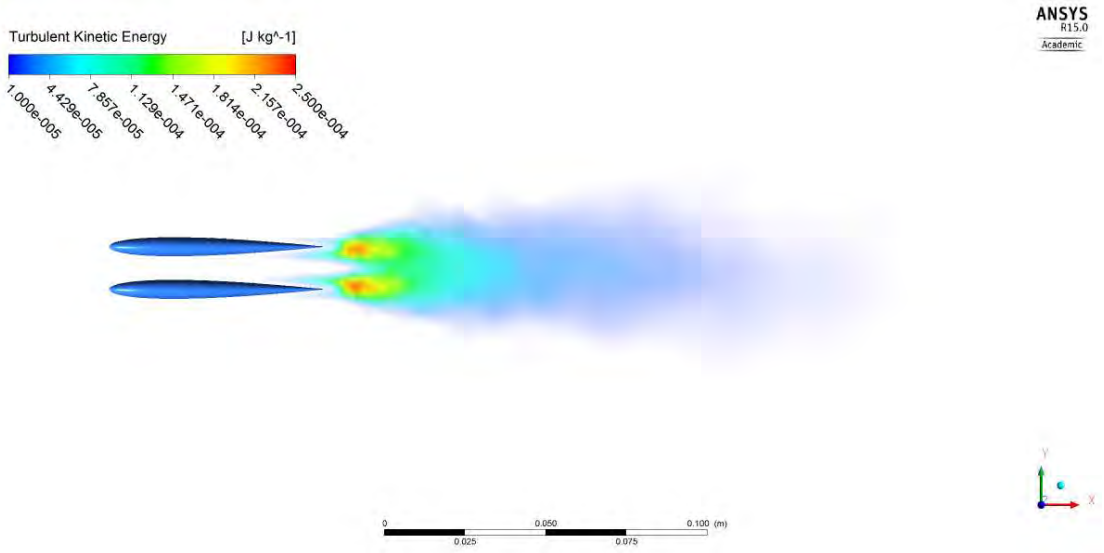

Figure 4.10: Comparison of fish wakes from three-dimensional simulations, close top view. (a) single fish wake; (b) 0.2 body lengths, BL, apart fish; (c) 0.4 BL; (d) 0.8 BL. Continues on the next page.

(c) - 0.4 BL geometry

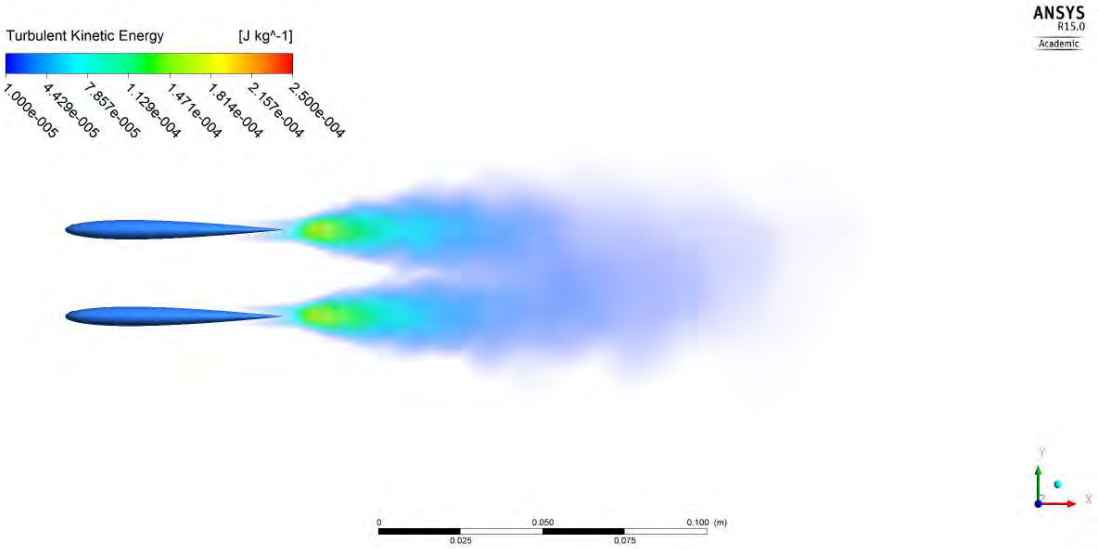

(c) - 0.8 BL geometry

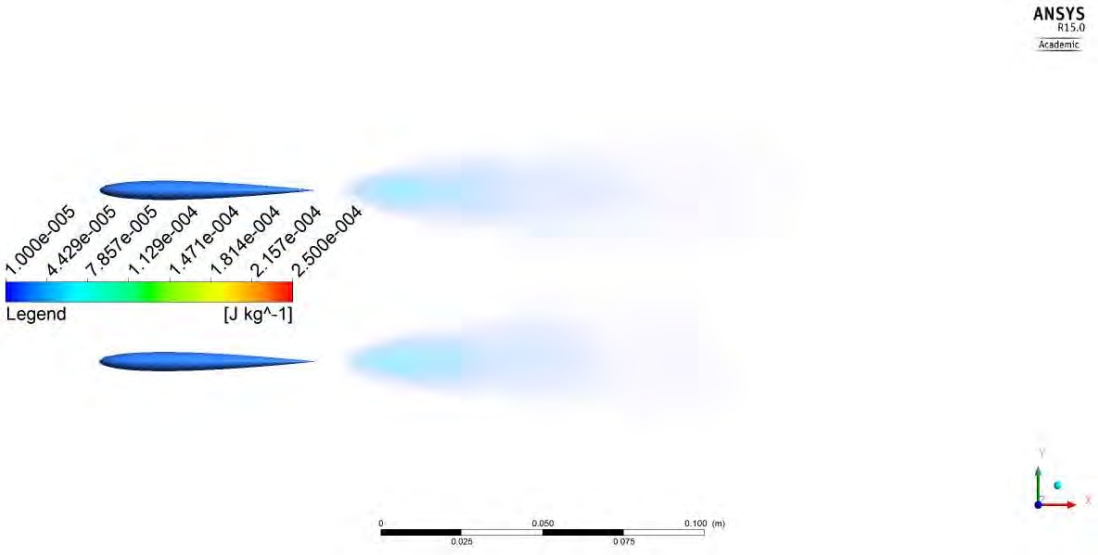

Continued from previous page.

(a) - single fish geometry

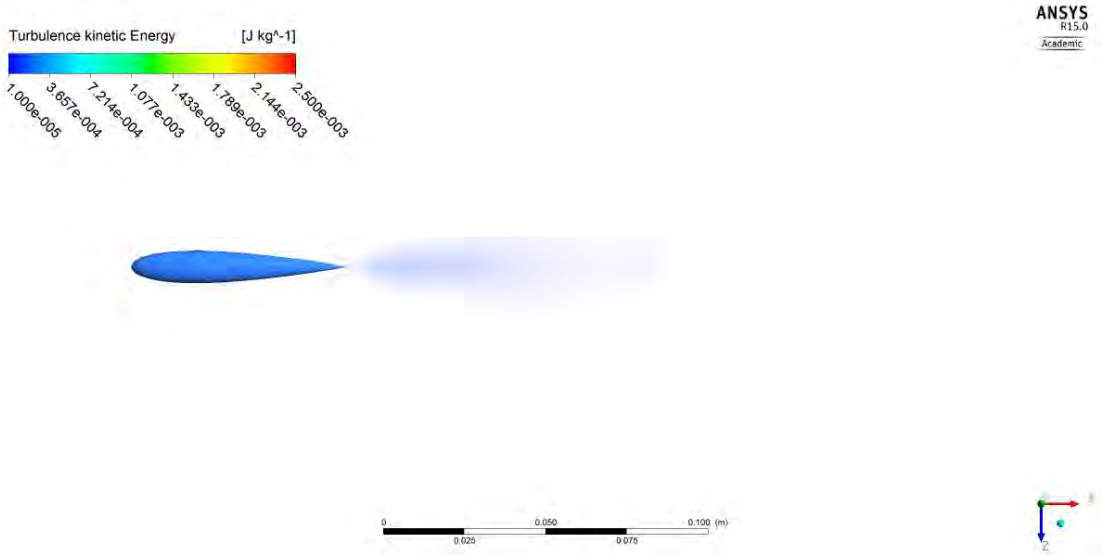

(c) - 0.2 BL geometry

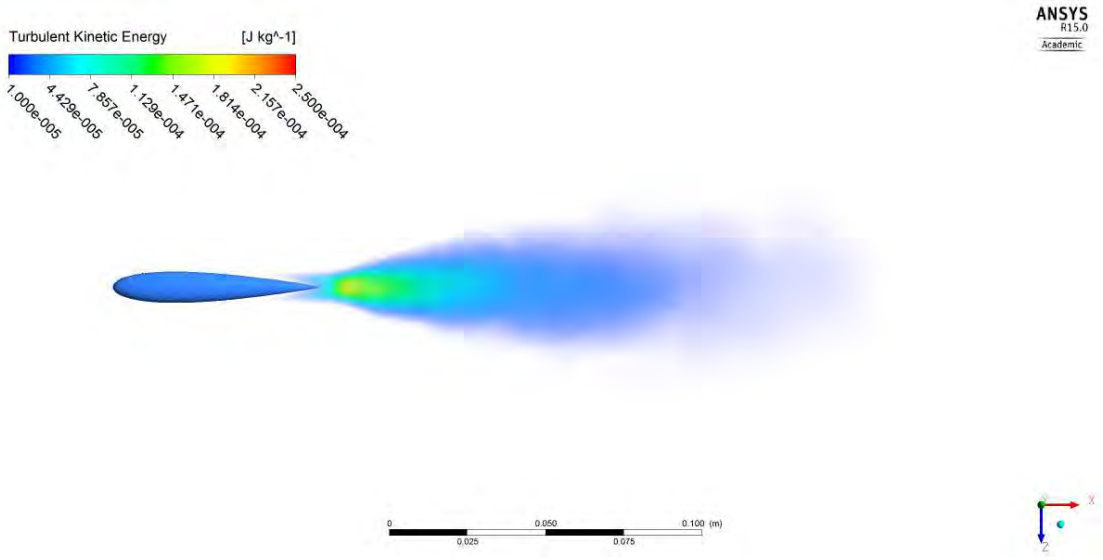

Figure 4.11: Comparison of fish wakes from two-dimensional simulations, close lateral view. (a) single fish wake; (b) 0.2 body lengths, BL, apart fish; (c) 0.4 BL; (d) 0.8 BL. Continues on the next page.

(c) - 0.4 BL geometry

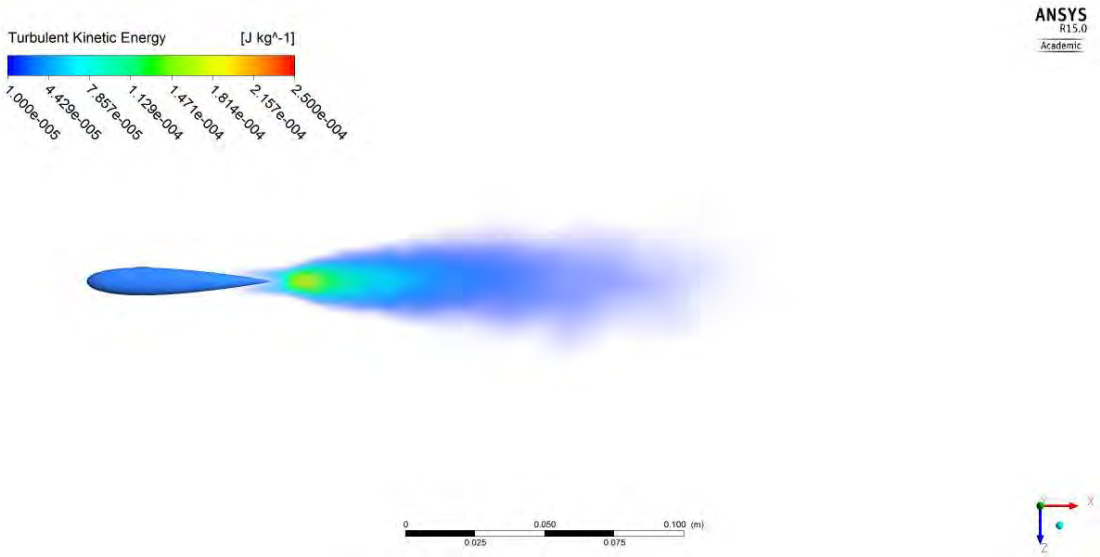

(d) - 0.8 BL geometry

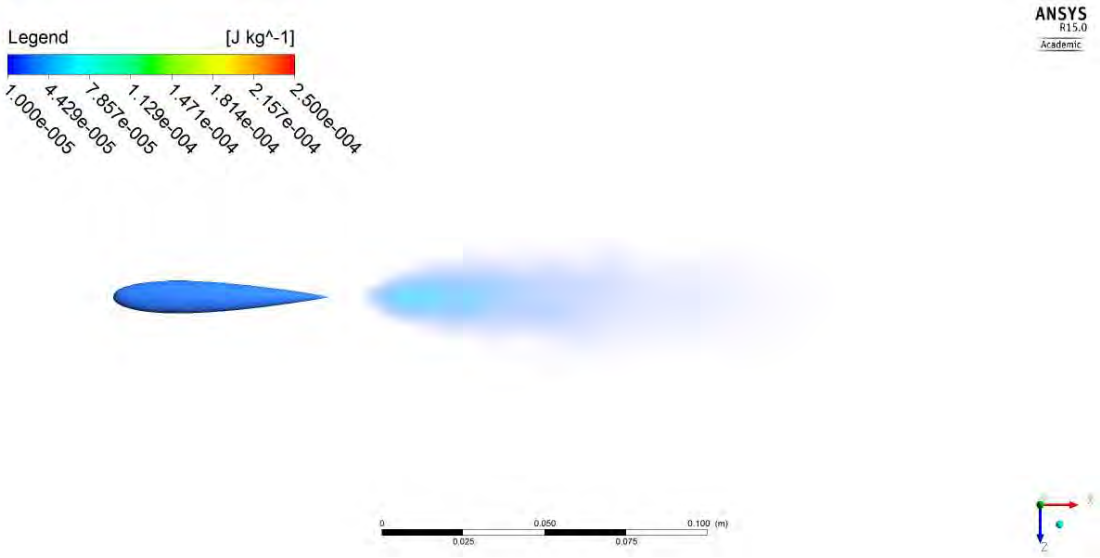

Continued from previous page.

(a) - top view

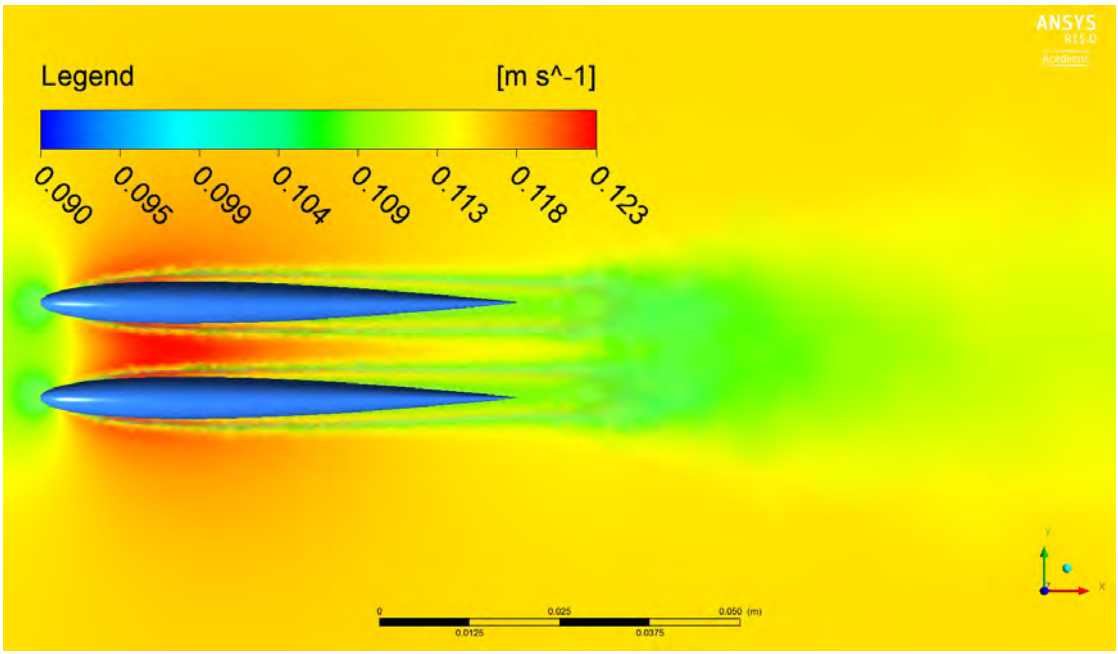

(b) - lateral view

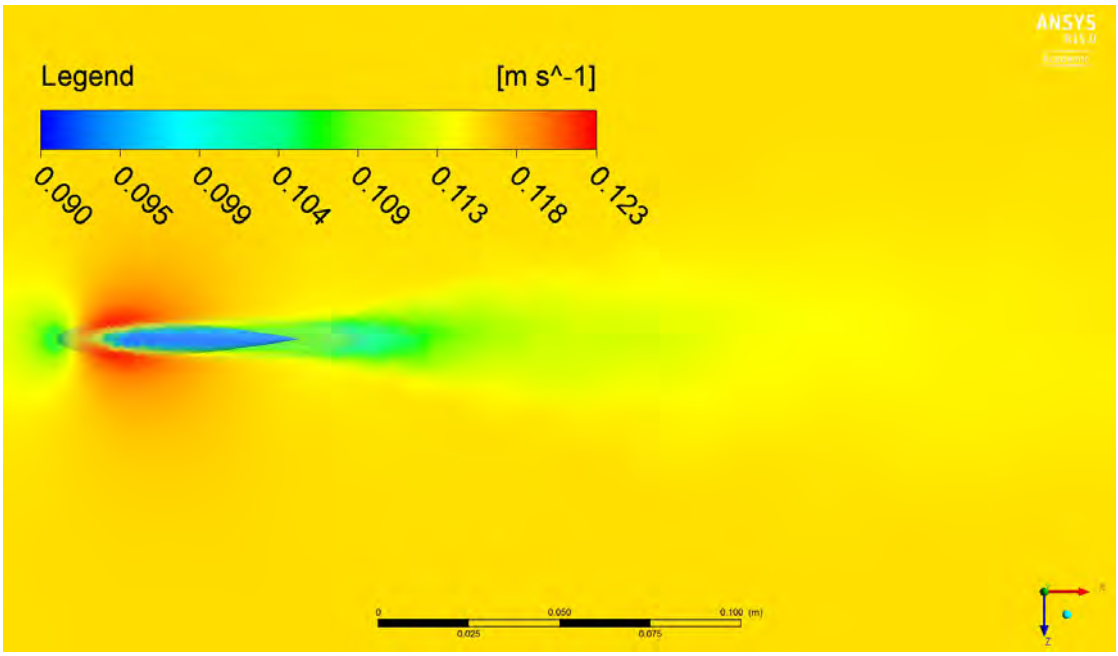

Figure 4.12: (a) flow velocity around 0.2 BL distant fish, top view; (b) flow velocity aroud 0.2 BL distant fish, lateral view of the flow in the middle of fish.

curve exponent of the two-dimensional simulation results is -0.163. This value is different from that one reported from *Quinn et al.* (2014) [26] for thrust force on single airfoil oscillating near the ground, -0.4, which was also used from *Dewey et al.* (2014) [11] to fit their results on coupled airfoil oscillating in phase at various distances. The difference in the power exponent could have origin from the absence of oscillations of this work simulated bodies or from the fact that drag force in the present work simulations is not equal to the inverse of the drag force as it was defined in *Quinn et al.* and in *Dewey et al.*.

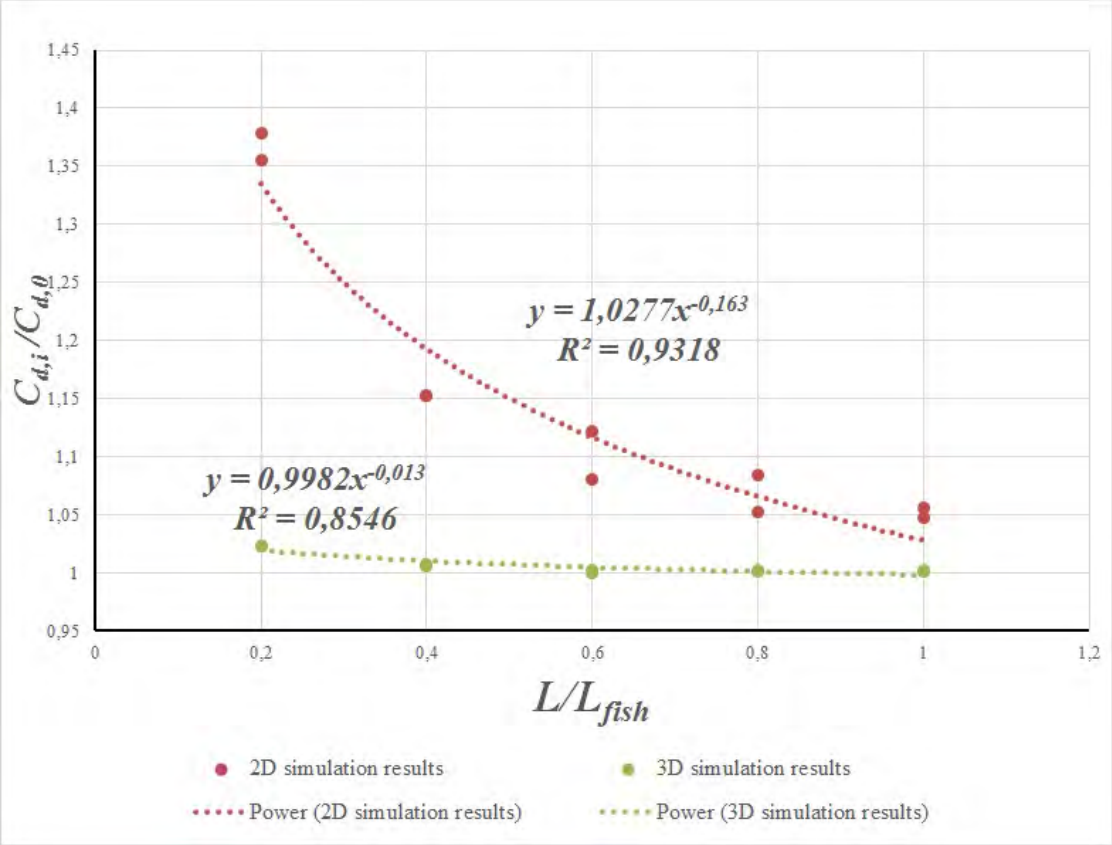

Figure 4.13: Comparison between two-dimensional and three-dimensional simulations results. Results are fitted with power law cures. $\frac{L}{L_{fish}}$ is the dimensionless distance among fish; $\frac{C_{d,i}}{C_{d,0}}$ is the ratio among fish drag coefficient at i distance to the other specimen versus the single fish drag coefficient.

The total force acting on a fish belonging to the densest school, computed as the sum of lift and drag forces, increases of 204% and of $2,73\%$ of the single fish

total force, respectively for two-dimensional and three-dimensional simulations. The small augmentation of total force, computed on three-dimensional simulations results, raises the idea that the force increment due to proximity effects is negligible for fish. However, the lift force, which is close to zero for the single fish, shows more important increments than drag force (e.g. 0.2 BL school's fish F_{lift} becomes $9,78\%$ of the single fish F_{drag}), and raises α up to $5°.46$. Thus, the change from 0 to $5°.46$ of the angle of the total force direction might be more relevant on fish behavior than the increment of the force modulus.

The comparison of fish wake (fig. 4.4, 4.5, 4.10 and 4.11) show that the wake length and turbulence kinetic energy increase with the reduction of the distance among fish. In particular, the turbulence kinetic energy increases in the internal side of schooling fish when they are close. However, this phenomenon is less important in three-dimensional simulations where there is an extra direction to dissipate energy.

The comparison of fish wake behavior with coupled circular cylinders wake behavior leads to the idea that simulated geometries are still far from the behavior of single bluff body occurring for very small gaps among cylinders. The shedding of two-dimensional 0.2 BL simulation's fish wake (sec. 3.5.1) is comparable with what occurs to circular cylinder at a distance of 2.2 T/D (fig. 1.2 and 1.3), but the increment of the fish drag coefficient is greater than that of a cylinder in the same condition of proximity (fig 4.2). Hence, there might be a relation with the body shape affecting the increment. Instead, three-dimensional simulations results suggest that the ratio T/D[3] at which coupled fish were analyzed is even higher then 2.2. In particular, the behavior results of 0.6 BL, 0.8 BL and 1 BL simulation (fig. 4.7) is close to that occurring to cylinder for T/D values of 5.

[3]Where D this time is the characteristic fish diameter.

Chapter 5

Preliminary experiments

The comparison of numerical simulations results with experimental data is a fundamental phase of the experimental process. During this phase, called *Validation*, the reliability of computed results is tested.

Experiments required in order to validate numerical simulations results were conducted at the *University of Southampton* Chilworth facility, the *Southampton Science Park*, during a period of nine days between March the 16^{th} and April the 1^{st}. The nine days of experiments were divided in two periods of three and six days.

In the first three days, a general check on the adequacy of the apparatus was done and rods drag forces were measured. Besides, the second period was characterized by fish drag force measuring.

Experiments were made using a 20m long internal flume with section width of 1.4m and height of 0.6m. The experimental flow velocity was about $0.11 m/s$ measured 2m upstream fish.

5.1 Apparatus

5.1.1 The experimental fish body and the support structure

Two plastic fish were 3D printed using an *Afinia H480 3D Printer*(Fig. 5.1). Fish were designed with a hole where a rod would have been fixed. Rods were then

clutched to a wood beam connected to a load cell, which was mounted on a beam fixed on the sides to the flume (Fig. 5.2).

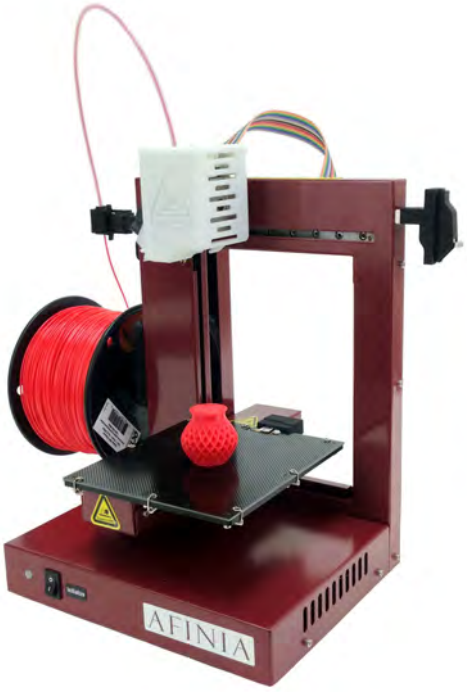

Figure 5.1: Afinia H480, a middle level 3D printer. The picture has been taken from the web site *https://www.3dhubs.com/3d-printers/afinia-h480*.

The structure sustaining fish was a source of errors on the readings (e.g. rods drag forces). Hence, the preliminary design considered this element and tried to reduce the structure influence on measures by increasing the magnitude of the measured force. In order to do this, the fish size was increased, so that forces magnitude were increased too. Being fish-section dimensions related to the length through proportions showed in appendix A and in figure 3.10, the studied parameter was the fish length.

Rods introduce errors both because the structure transmits vibrations and because of the hydrodynamic effect on the submerged part. This last contribution was esteemed to be one half of the computed force value for a 70cm long fish. The drag coefficient of rods was considered approximately equal to 1 like that circular cylinders have for the same Re [29]. While, the fish drag coefficient was taken from single fish numerical simulations results and was about 0.4.

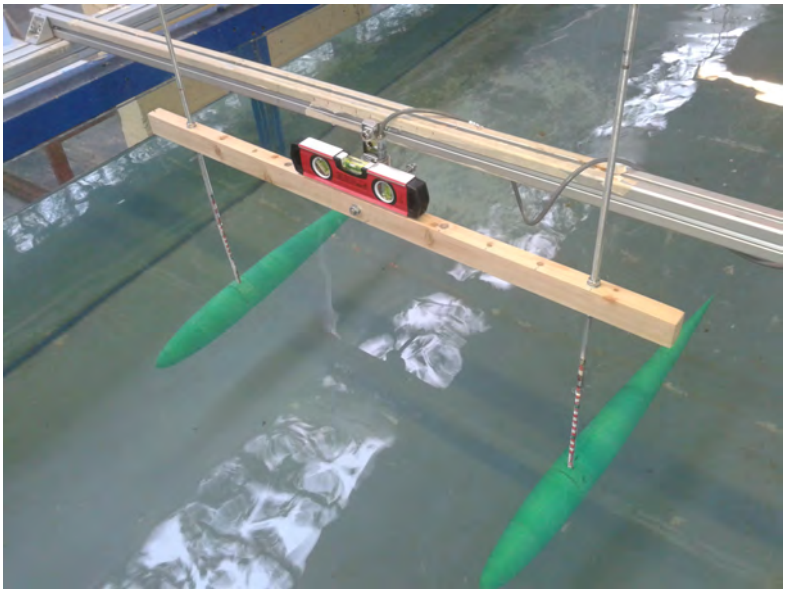

Figure 5.2: Structure used for the experiments.

Given the water depth of 0.5m and the distance of fish center of mass form the flume bottom, 0.25m, their length was chosen to be 0.7m (Fig. 5.3). Table 5.1 shows calculated forces compared with fishes length.

Fish are empty in order to reduce the consumption of printing plastic and were printed in sections because of limits imposed by the printing area. So, they were firstly divided every 10cm in 7 sections. Hence, the first and the third section, counted from the fish nose, were divided again.

The first section has been divided in order to allow the printer to properly print the fish nose, also called section 1.1. This piece is characterized by great curvature. It would have been difficult to print respecting the applied savings of material, if section 1.1 and section 1.2 had been printed all together in section 1. In order to follow the idea of material saving, section 1.2 was designed with a hole, while section 1.1 was full.

The third section was by far the more complex. In fact, this is the section where the rod is inserted. Rods are threaded M8 steel bars with weight of 311g. These were fixed to the fish body using four M8 nuts for each fish. In order to reduce the roughness of fish, nuts needed to be hide inside fish body. Section 3 was designed to do this. Piece 3.1 (fig.5.4) has a bottom hole designed to place two nuts. Instead, the top of piece 3.1 is flat in order to allow nuts to be tightened.

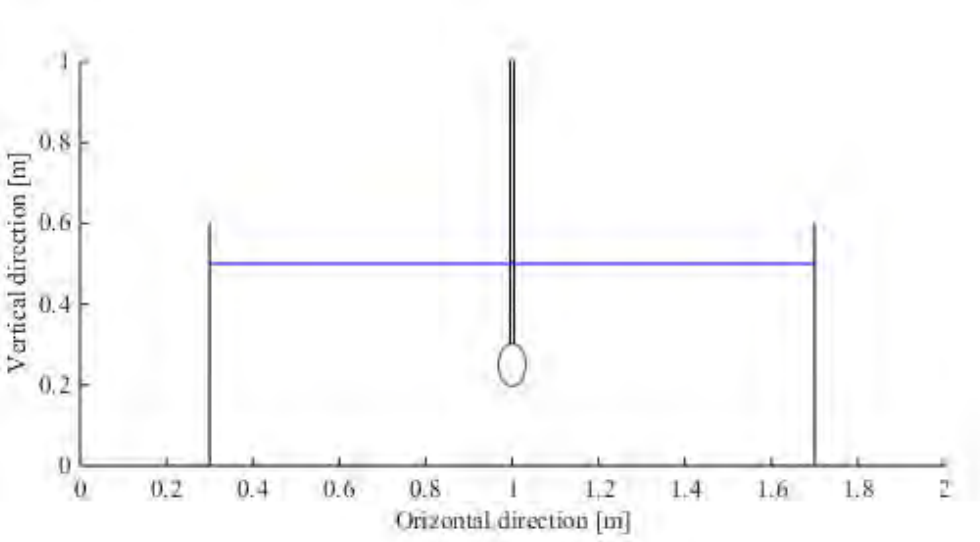

Figure 5.3: The dimension of a fish compared to the flume section.

Fish Length	**Fish force as a % on total force**	**% of Area Occupation**	**% of horizontal length occupation**
L [cm]	$\frac{F_{fish}}{F_{total}} \cdot 100$	$\frac{A_{fish}}{A_{flume}} \cdot 100$	$\frac{D_{fish}}{1.4m} \cdot 100$
50	35.67%	0.76%	6.42%
60	45.28%	1.09%	7.71%
70	**53.90%**	**1.48%**	**9.00%**
80	61.35%	1.94%	10.28%
90	67.65%	2.45%	11.57%
100	72.92%	3.03%	12.86%

Table 5.1: Comparison of fish forces, occupation area and horizontal length occupation for fish of different lengths. L is the fish length, $\frac{F_{fish}}{F_{total}} \cdot 100$ is the percentage of fish drag force, F_{fish}, on the total computed force, F_{total}. $\frac{A_{fish}}{A_{flume}} \cdot 100$ is the percentage of fish occupation area, where A_{fish} is the fish section area and A_{flume} is the flume area. $\frac{D_{fish}}{1.4m} \cdot 100$ is the percentage of fish length occupation measured as the ratio among fish smaller diameter, D_{fish}, and the flume width.

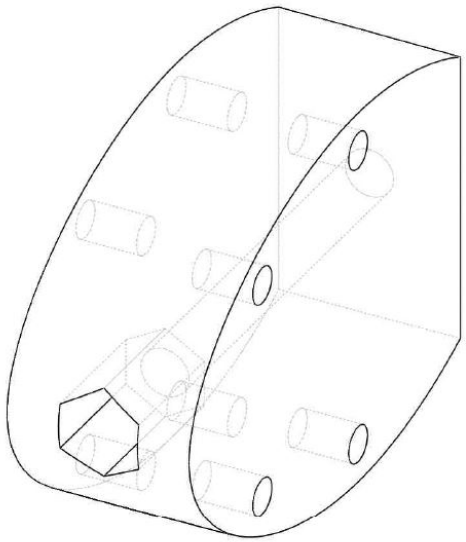

Figure 5.4: Trimetric axonometry of section 3.1.

Nuts allocations have been then topped with caps (fig.s 5.5 and 5.6) following fish shape from appendix A.

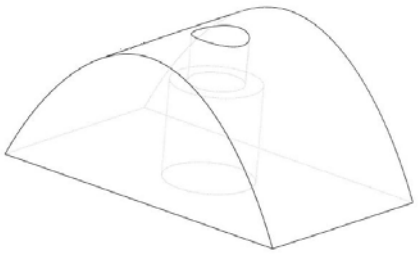

Figure 5.5: Upper nuts top.

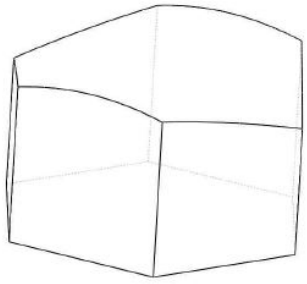

Figure 5.6: Lower nuts top.

Fish have been completely covered with silicone to impede water to go inside their body.

The wood beam was pierced in order to reproduce distances between fish that were studied during numerical simulations (see section 3.4.1). The structure depicted so far is fixed to the load cell through an horizontal M8 beam and then tightened together (fig. 5.7).

Figure 5.7: Junction of the structure to the load cell.

5.1.2 The load cell

The load cell used for experiments has been produced by *Tadea-Huntleigh*. The model is the $355C3$ and is a welded bending beam load cell manufactured in stainless steel (Fig. (5.8)).

The load cell characteristics allow the instrument to properly works with a wide range of temperatures and without suffers the presence of humidity. Its maximum capacity is $5 \cdot \vec{g}$ kN. The total error according to OIML R60[1] is 0.02% of the rated output.

Load cell measurements are based on the difference of resistance induced by deformation on four strain gauges. This strain gauges patter (fig. 5.9) allows to compensate the errors due to singles strain gauge measurements. Hence, the output is weighted on the four strain gauges readings.

Load Cells need to be calibrated. Calibration is the phase during which the measurement is compared with known quantities to improve its accuracy. The load cell has been calibrated using a series of weights of $50g$ up to reach $150g$.

In order to calibrate the cell (Fig. 5.10) a scaling factor has been applied to the

[1]International Recommendation: Metrological Regulation for Load Cell

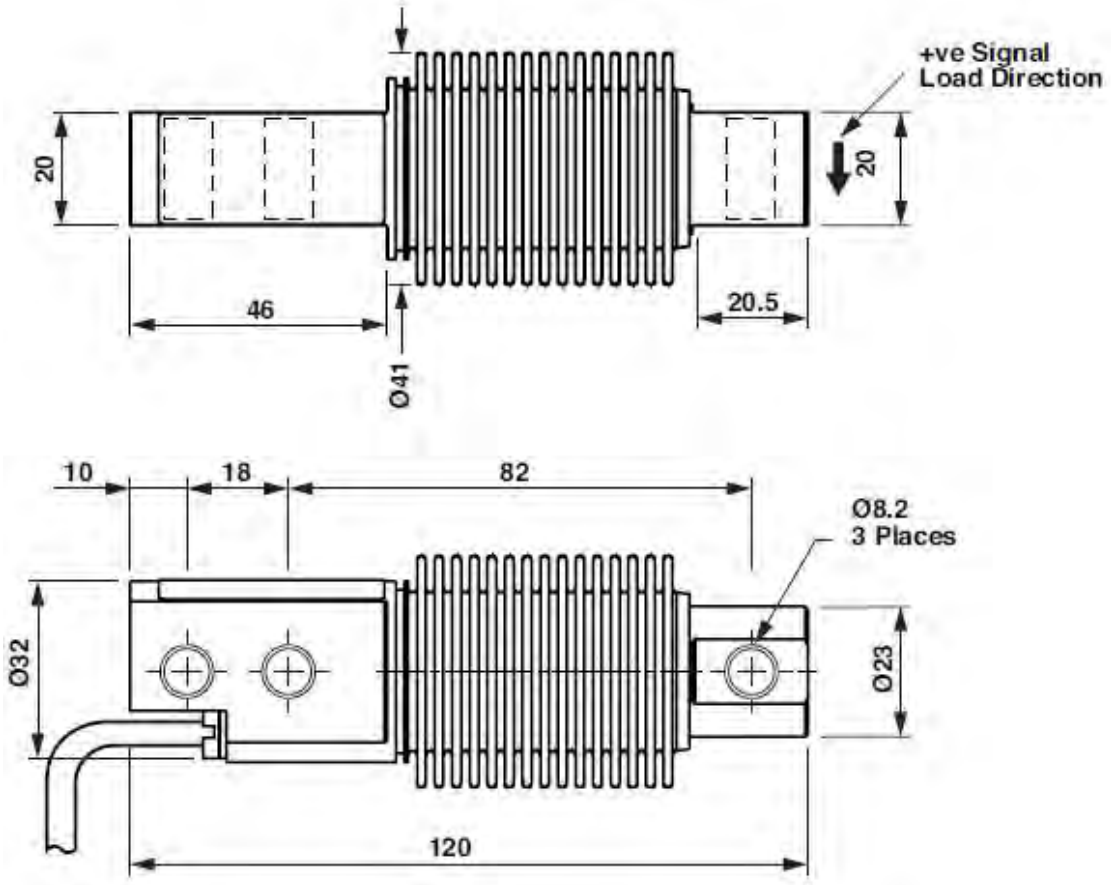

Figure 5.8: Load Cell model 355 C3. Measure in *mm*

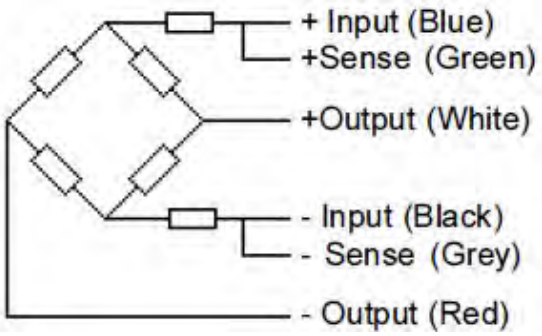

Figure 5.9: Strain gauses scheme.

output making it coherent with test samples weight. Two scales factor have been used to define the linear relation among resistances and forces. The ratio between outputs and inputs, expressed in mV/V, and the applied load, *kgf*, have been used

to define the linear relation among strain and measured forces (Fig. 5.11).

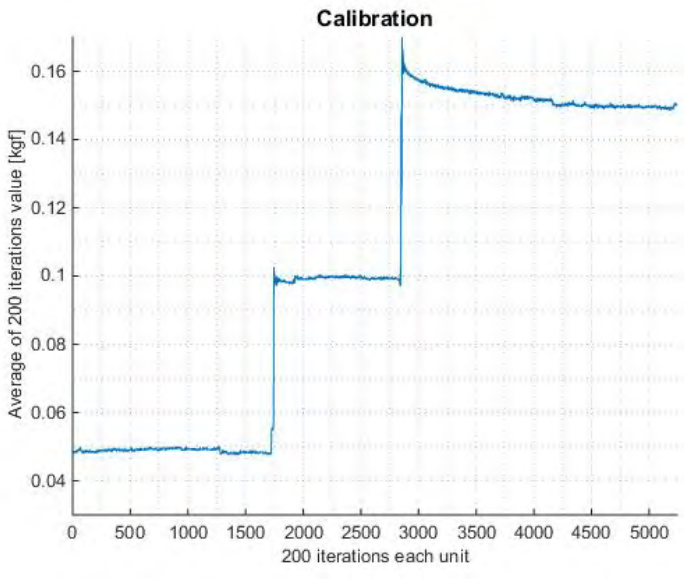

Figure 5.10: Calibration of the load cell. The picture shows the effect of the 3 load steps: 50g, 100g anf 150g.

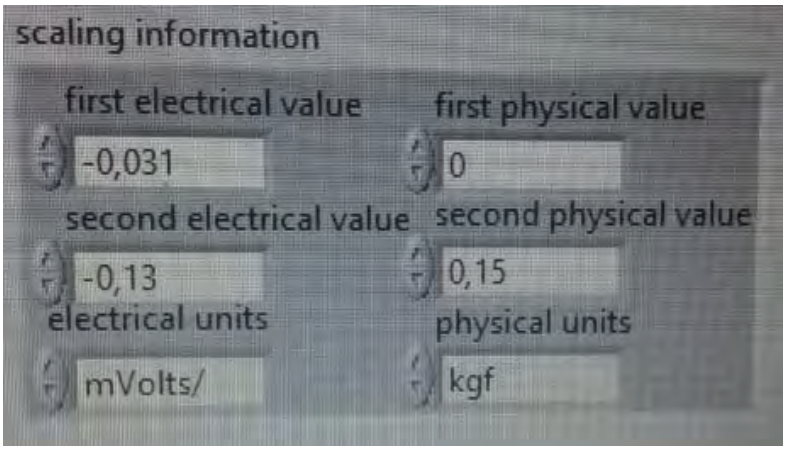

Figure 5.11: Scaling factor values assigned after calibration had been performed.

5.1.3 Velocity measurements

Velocity measures were done in order to calculate the darg coefficients value. The instrument utilized for the velocity measurement is the Flow Tracker® Handheld

ADV ® (Fig. (5.12)).

The probe of the instrument emits an acoustic signal which is then collected by the instrument itself through appropriate receivers. This technology allows to measure the velocity of a "point" $10cm$ away from the probe. Hence, the instrument does not create any disturbance to the flow. The instrument range of measurement is between $0.001m/s$ and $4.0m/s$.

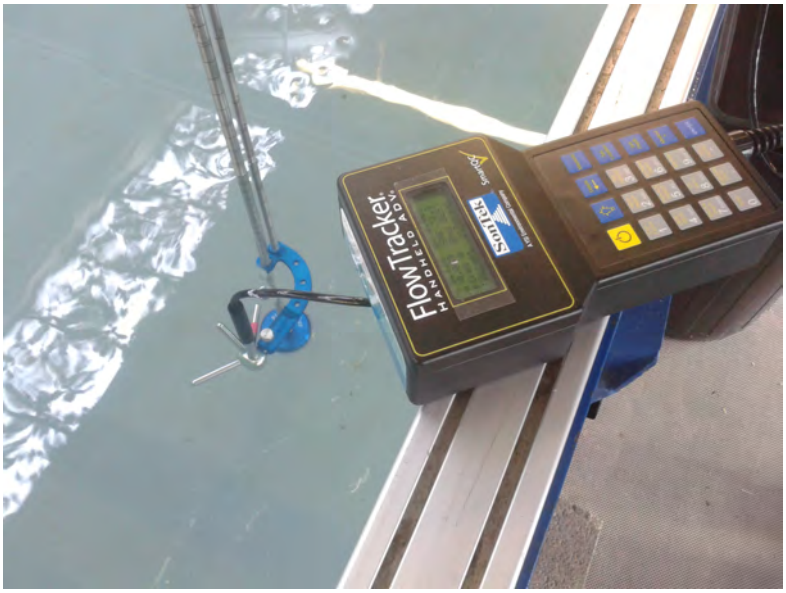

Figure 5.12: Flow Tracker® Handheld ADV ®.

5.2 Method

The structure weight induced a deformation on the load cell, which measured a non-zero value. This unwonted initial measured force value, F_0, was subtracted from values measured when the structure was immersed and subjected to the flow, F_{Flow}, thus, drag forces were calculated as:

$$F_{Drag} = F_{flow} - F_0 \tag{5.1}$$

Measurements corresponding to the second element in the right hand of the equation 5.1 were done when the structure was fixed to the load cell while there was no water in the flume. Then, pumps were switched on and measurements

of F_{flow} value were taken. Figures 5.13 (a) and (b) show two measurements of F_{flow} taken for the same experiment, while figure 5.13 (c) shows the measurement of F_0. Each measure lasted at least 3 minutes and the sampling frequency were 2000 sampling each second. In the time between the two F_{flow} measurement of each experiment, the velocity was measured in three points of the flume section. Velocity measurements were taken at the height of fish nose about $1.7m$ upstream the structure (Fig. 5.13 (d)).

In sum, the experiments phases were:

- 1) F_0 was measured while pumps were turned off;
- 2) Pumps were switched on and F_{flow} first measure was taken after the flume reached uniform flow and the water depth was $52.3m$;
- 3) The velocity was measured in three points;
- 4) F_{flow} second measure were made. After the measurement, pumps were switched off and the structure removed to change the distance among fish.

However, being F_{Drag} the subtraction of two measurements made with and without water, the effect of the buoyancy force occurring while the structure were submerged turned out to be the major errors component of measurements. As will be seen later, experimental results are not representative of the drag force on the structure because the load cell deformation is mainly produced by the effect of the momentum induced by the buoyancy force. The momentum is of curse increased by the increasing of the drag force.

5.3 Experimental results

Figure 5.14 shows experimental F_{Drag} results, which are classified according to set-up changes occurred during experiments. Figure 5.14 (a) shows experiments results obtained during the period among the 23^{rd} and the 26^{th} of March. These first series of measurements had the problem that fish gain weight during sampling, which was due to water entering fish body. Hence, fish have been emptied and sealed again with silicone. Then the series of measurements of the 27^{th} and of

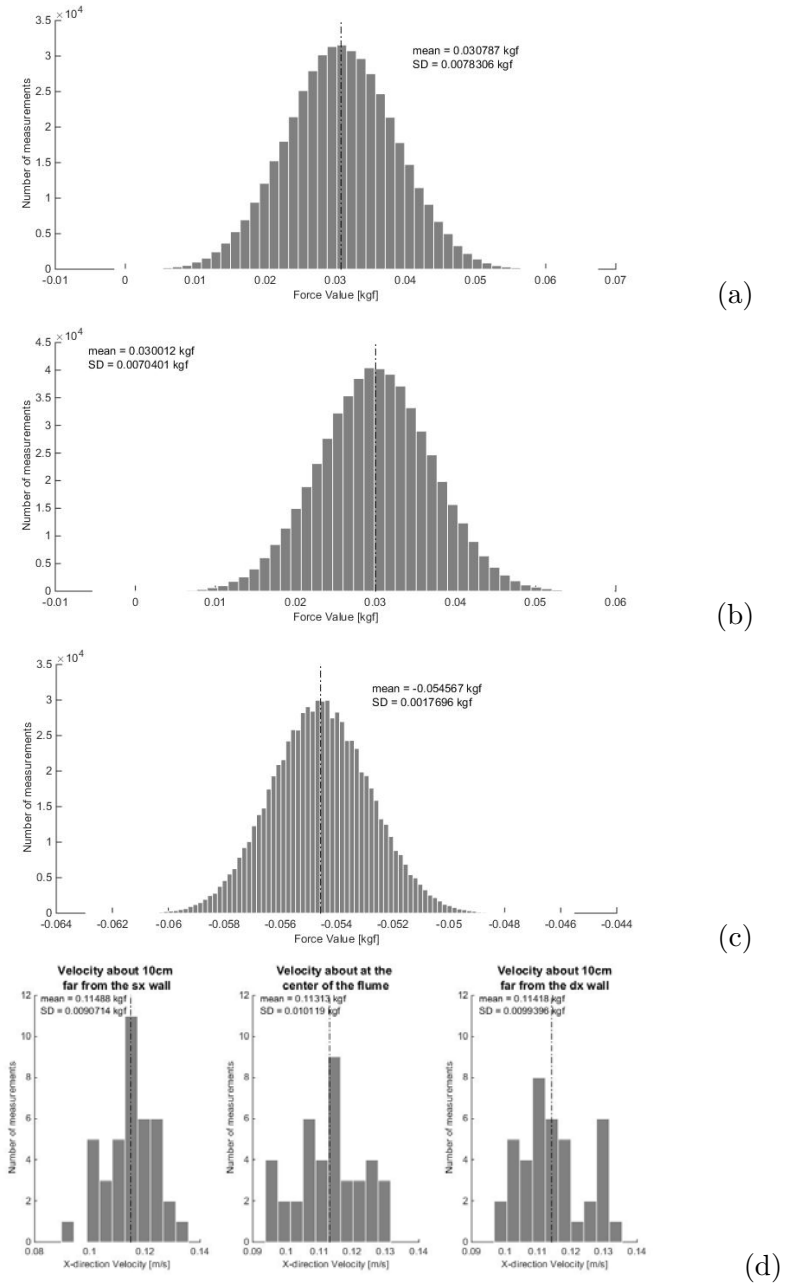

Figure 5.13: Figure (a) and (b) are the histograms of two consecutive measurements of forces on the structure while fish were at 0.4 body length apart and they were subjected to the flow force. Figure (c) is the histogram of forces measured for the same condition of distance, but with the structure emerged. It is possible to notice that even when there were no evident forces, the load cell measured a certain noise. Last three figures (d) are histograms of velocities measured during the same series of measurements.

the 30^{th} of March were done. Analyzing these series of measurements in picture 5.14 (b) is noticeable that measures taken for the same distance among fish have a scattering among them relatively small except for those relative to the distance 0.2 BL. This difference might be due to the increasing of the lift force, which can modify the reading introducing vibrations.

Finally, figure 5.14 (c) shows results taken after emptying again fish bodies and, in order to evaluate the effect of the buoyancy force, after that the fish center of mass was moved appreciably farther from the load cell center of rotation than what were done during other measurements. The buoyancy force effect can be seen comparing the force values computed for the distances of 0.4 BL and 1 BL of measurements series reported in figures 5.14 (b) and (c). In fact, the momentum induced by the buoyancy force increases with the increasing of the distance among center of mass and center of rotation. Indeed, this distance is affected by the drag force increasing.

5.4 Sources of error

The buoyancy force

The buoyancy force is related to the difference of weight of the fish volume when made of water and when occupied by fish. The momentum generated by this force is function of the distance among the fish center of mass and the load cell center of rotation. Figure 5.15 show a general scheme of forces acting on the experimental structure.

A rough esteem of forces acting on fish can be made considering the weight of a fish to be about $500g$ which is a good esteem of the fish weight for the measurements series made after the 27^th of March (Fig. 5.14). The F_{Drag} value is:

$$F_{Drag} = (\frac{C_{D,fish}}{2} A_{fish} + \frac{C_{D,rod}}{2} A_{rod}) \rho \langle U \rangle^2 = \tag{5.2}$$
$$= (\frac{0.4}{2}\ 0.006 + \frac{1}{2}\ 0.002)\ 1000\ 0.11^2 = 0.027kN$$

While the buoyancy force, $F_{Buoyancy}$, computed as the whole fish body would contributes to the momentum in the same way, is (the volume of the single fish, V_{fish} is $1966cm^3$):

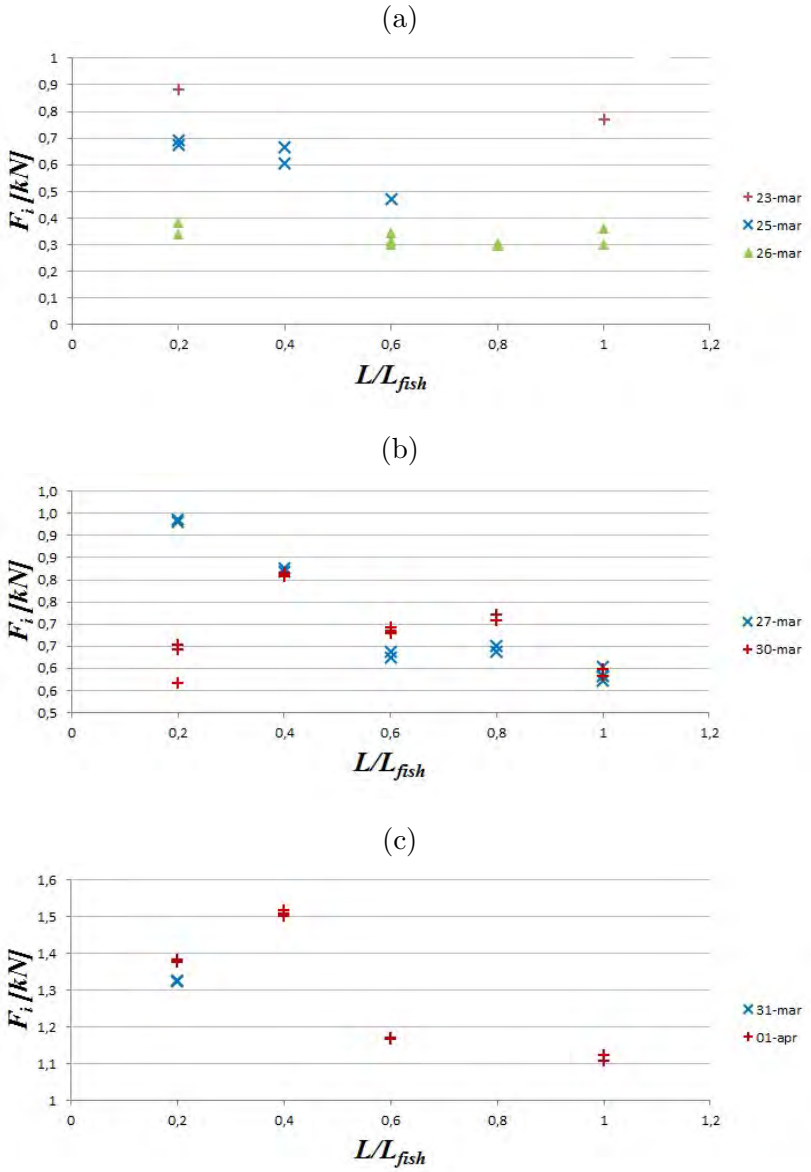

Figure 5.14: (a) measurements taken the 23^{rd} (triangles), the 25^{th} (x) and the 26^{th} of March (+); (b) measurements taken the 27^{th} (x) and the 30^{th} of March (+); (c) measurements taken the 31^{st} of March (x) and the 1^{st} of April (+). The reason behind the division of the data in three graphs is because (a) suffers of errors due to the water entering fish body, (b) is made with results after the first attempt to remove water from fish bodies, while (c) is made with results obtained after the second attempt to remove water from fish. During (c)'s measurements also the setting of the structure was changed in order magnify the effect of the momentum due to the buoyancy force and verify its effects. L/L_{fish} is the dimensionless distance among fish where L_{fish} is the fish length and L is the distance among animals.

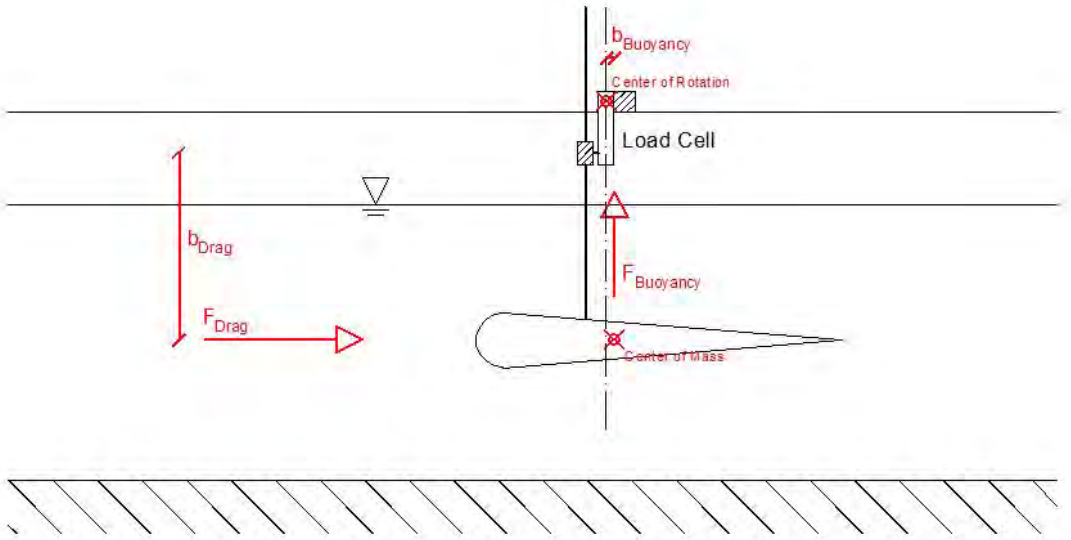

Figure 5.15: Schemes of forces acting on fish. F_{Drag} drag force on structure; $F_{Buoyancy}$ buoyancy force; b_{Drag} darg force arm; $b_{Buoyancy}$ buoyancy force arm.

$$F_{Buoyancy} = \vec{g}\rho(V_{fish} + V_{rod,sub}) - \vec{g}(M_{fish} + M_{rod} + Mbeam) =$$

$$9.81\ 1000\ 0.002 - 9.81\ 0.85 = 11.3kN \tag{5.3}$$

Where $C_{D,fish}$ and $C_{D,rod}$ are fish drag coefficient and rod drag coefficient respectively, A_{fish} and A_{rod} are fish and rod vertical section area, $\langle U \rangle$ is the mean velocity, ρ is the water density, $V_{rod,sub}$ is the submerged rod volume, M_{fish} is the fish weight, M_{rod} is the rod weight and M_{beam} is the beam weight.

The real buoyancy force could be more then one order of magnitude lower of the one reported above because not all the fish body contributes in the same direction to the buoyancy momentum. However, this quantity increases with the increasing of the arm, $b_{Buoyancy}$ and with the movements of the water inside fish bodies.

Being the buoyancy force at least two order of magnitude greater than the hypothesize drag force and being results more than one order of magnitude higher than what were expected, it is my opinion that the buoyancy force compromised results. However, the increasing of the forces value with the reduction of the distance among fish leads to the consideration that there is an increasing of forces (lift and drag) on the structure affecting the arm of the buoyancy force.

The Blockage effect

The *Blockage* is a well known effect due to the proximity to walls, which induce a confining effect that affects the wake. This effect grows with the increasing of the flume section occupation by the obstacle.

According to this definition, I expected an increasing of the measured force value when fish were near the wall, thus for studied distances of 0.8 BL and 1 BL. However, this phenomenon is not recognizable in the data.

Vibrations

Vibrations effects can be seen in figure 5.13 (a) and (b) in the wide range of values measured by the instrument. Vibrations inducing those effects are mainly due to the flow turbulence and to the elasticity of the structure. However, other sources of noise, e.g. pumps, might induce vibrations affecting readings.

Another source of vibrations might be the lift force on fish. The effect of these forces is to push a specimen against the other. Hence, vibrations arise from the elasticity of steel beams and by the water resistance. It cannot be excluded that these vibrations affects the readings too.

Hydrodynamic effects

Hydrodynamic effects induce an increasing of the water level upstream obstacles. This phenomenon introduces another force, ΔF, on the structure due to the difference of the water level before and after obstacles. Being fish areas big, the contribution that the water level difference makes on those surface was considered negligible, while, effects on rods, which have smaller area and higher drag coefficient, was computed (Fig. 5.16).

$$\Delta F = \left[\frac{1}{2}D\gamma(h+\Delta h)^2 - \frac{1}{2}D\gamma h^2\right] = 0.018kN \tag{5.4}$$

where: h is the height of the submerged part of rods has value $0.21m$; the increasing of the water level, Δh, is about $0.001m$; γ is the specific gravity of water; and D is the rod diameter with value 0.009.

The comparison between ΔF value and the value of the drag force of equation 5.2 shows how the measures were affected also by this element.

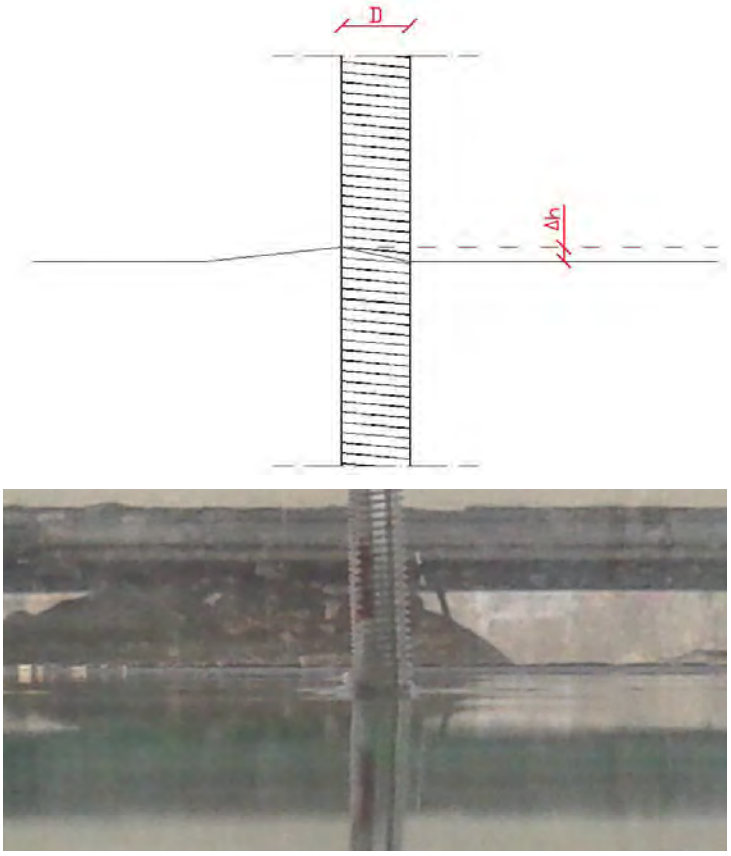

(a)

(b)

Figure 5.16: Hydrodynamic effect on structure. (a) references; (b) picture of the effect.

5.5 Experimental results and errors discussion

The main problem of the present experiment was the buoyancy force, which induced a momentum greatly modifying measurements. This force could be reduced making fish weighting as the water moved. However, the weight gain due to the water entering fish bodies might affects also these fish.

Nevertheless, other vibrations cannot be avoided modifying fish weight. In order be able to exclude the contribution of lift forces vibrations from the uncertainties, a more complex instrumentation, capable to measure forces and momentum in more directions, is required.

To conclude, this experiment has too many uncertainties to be able to proper determine drag coefficients value, but the results trend, as seen in figures 5.14 (b)

and (c), leads to the idea that the force acting on fish increases with the reduction of the distance among fish and that affects the buoyancy force arm. Thus, the load cell deformation, due to the buoyancy force momentum, increases too.

Conclusions

Numerical simulations were the first choice in order to verify the presence of a hydrodynamical benefit on fish belonging to a two-specimens side-by-side school. *CFD* could be faster and cheaper than other experimental methods, but requires the execution of phases such those of the sensitivity analysis and of the validation of the model to make results reliable.

The sensitivity analysis were carried out and reported in chapter 3. In particular, during the sensitivity analysis phase, turbulence models were tested. The model chose to study drag and lift coefficient is the *Realizable* k-ϵ model. It is a two-equations model deriving from the coupling of *RANS* equations with turbulent kinetic energy, k, and its rate of dissipation, ϵ, transport equations. This model family is well known for its commercial applications and for the limited computational effort required. Finally, simulations were done both with two-dimensional and three-dimensional geometries.

Results of these simulations showed that fish belonging to a side-by-side schools at 0.3 body lengths, BL, apart experience higher forces than a single fish in the same flow condition. In particular, according to two-dimensional simulations results, the drag force computed for fish belonging to the densest school (0.2 BL) is 37.9% higher than the same force computed for the single fish. This increment is reduced to only 2.26% for three-dimensional simulations. Lift force on fish, calculated in the horizontal direction normal to the flow, grows up to 271% and 9.78% of the single fish drag forces computed respectively using two-dimensional and three-dimensional simulations.

The increasing of forces on fish is also visible by comparing coupled fish wakes (fig. 4.4, 4.5, 4.10 and 4.11). The reduction of the distance among fish increases both the wake length and the flow turbulence around them. In particular, the

increment of turbulence occurs near fish tail in the internal side of the school. Three-dimensional simulations fish wakes are shorter than those computed for two-dimensional simulation. This is due to the introduction of the third dimension, which increases the turbulence dissipation. However, the comparison of wakes and drag coefficients (fig. 4.2 and 4.7) of coupled fish and coupled circular cylinders (fig. 1.3) leads to the idea that studied distances are far from those generating the single-bluff-body condition described by *Sumner et al.* (2010) [28] for cylinders. In particular drag coefficient increments computed for three-dimensional simulations with distances between fish of 0.6, 0.8 and 1 BL are comparable with those corresponding to cylinders far apart enough to avoid wakes interactions. Figures 4.10 (d) and 4.11 (d) show this non-interaction condition for the distance among animals of 0.8 BL.

In order to validate results, laboratory experiments were done. Experiments were made trying to reproduce numerical simulations condition. However, it was not possible to compare experimental results values with those obtained through simulations because of problems in the experimental set-up. In fact, the buoyancy force and its momentum induced unwonted deformations to the load cell, which modified the readings. In particular, the arm of the buoyancy force, hence the momentum influence on the load cell, increased with the increasing of drag force. Figures 5.14 (b) and (c) show trends of results that might be comparable with those of numerical simulations considering the effect of the drag-buoyancy interaction described.

In conclusion, no evidences of a hydrodynamical benefit were found. Besides, swimming in a dense side-by-side school of two elements is generally more expensive than swimming alone. This result agrees with *Hemelrijk et al.* (2014) [13] results showing a decreasing in Froude efficiency[2] for dense schools. However, their results also show a benefit for fish swimming more than 0.8 BL apart. According to mine three-dimensional simulations results, there are no interaction among wakes for those distances among fish, which experience the same lift and drag forces than a fish swimming alone. Hence, the benefit described in Hemelrijk et al. might arises from the in-phase swimming of their fish. Further experiments on the topic should

[2]The *Froude efficiency* is the dimensionless ratio between the power used to move forward and the total power.

consider the phase of fish swimming to understand possible interactions among wakes.

Finally, the studied fish behavior might be related to the transmission of information among specimens. *Partridge and Pitcher* (1980) [22] studied handicapped fish schooling capacity. They showed that fish handicapped of the lateral line are capable to school, but their preferred distance to the nearest neighbor, NND, was reduced. They related this behavior to the incapacity of fish to perceive the repulsive stimulus from the sectioned organ. Furthermore, NND normally decreases with the growth of the number of fish swimming in the school [22, 23]. These behaviors occur when lateral line's stimuli might be confused by the turbulence induced by the school's member or are completely absent as in the case of handicapped fish. In this work starting data, fish swim at a distance of 0.3 BL in a side-by-side school pattern when the flow velocity is high, while, for the slower velocity case, they keep the same mean direction, but the school is more loose (fig. 2.7 and 2.8). It is possible that, in the high velocity case, the fish perception of the surrounding through the lateral line is diminished by the flow turbulence. Hence, there might be a relation between the information transmission due to the organ and the position in the school.

Moreover, forces increments might be negligible for fish. In fact, the total force acting on a fish belonging to the densest school, computed as the sum of lift and drag forces obtained from the three-dimensional simulation, increases of $2,73\%$ of the single fish total force.

Appendix A

NACA profiles

NACA0009 and NACA0015 profiles were introduced in section 3.4. These profiles describe the fish shape along the horizontal and vertical direction respectively. The shape of NACA profiles are reported in table A.1 as series of points. The series of points represent only one side of the fish shape because profiles are symmetrical. Also, point coordinates are scaled for a one meter long airfoil. Figure 3.10 shows profiles shape.

Length [mm]	Width [‰ of L]	Height [‰ of L]
0	0	0
0.247	2.085	3.509
0.987	4.141	6.971
2.219	6.167	10.382
3.943	8.163	13.743
6.156	10.128	17.05
8.856	12.059	20.301
12.042	13.956	23.494
15.708	15.816	26.626
19.853	17.638	29.694
24.472	19.42	32.694
29.56	21.16	35.622
35.112	22.855	38.476
41.123	24.503	41.251
47.586	26.102	43.943
54.497	27.65	46.549
61.847	29.144	49.064
69.629	30.582	51.485
77.836	31.961	53.807
86.46	33.28	56.028
95.492	34.537	58.143
104.922	35.728	60.149
114.743	36.853	62.043
124.944	37.91	63.822
135.516	38.897	65.483
146.447	39.812	67.024
157.726	40.655	68.444
169.344	41.425	69.739
181.288	42.12	70.909
193.546	42.741	71.954
206.107	43.286	72.871
218.958	43.755	73.662
232.087	44.15	74.326
245.479	44.469	74.864
259.123	44.715	75.277
273.005	44.886	75.566
287.11	44.985	75.732
301.426	45.013	75.779
315.938	44.97	75.707
330.631	44.859	75.52
345.492	44.681	75.221
360.504	44.438	74.812
375.655	44.133	74.298
390.928	43.766	73.681
406.309	43.342	72.966
421.783	42.861	72.157
437.333	42.327	71.257
452.946	41.741	70.272
468.605	41.108	69.205
484.295	40.428	68.061
500	39.705	66.844

Table A.1: This table shows the NACA0009 and the NACA0015 values sampled on 200 points within one meter

Length [mm]	Width [‰ of L]	Height [‰ of L]
515.705	38.942	65.559
531.395	38.141	64.21
547.054	37.304	62.802
562.667	36.436	61.34
578.217	35.537	59.827
593.691	34.612	58.269
609.072	33.661	56.669
624.345	32.689	55.032
639.496	31.697	53.362
654.508	30.688	51.663
669.369	29.665	49.94
684.062	28.629	48.197
698.574	27.583	46.436
712.89	26.53	44.664
726.995	25.472	42.882
740.877	24.41	41.095
754.521	23.348	39.307
767.913	22.288	37.521
781.042	21.23	35.741
793.893	20.179	33.971
806.454	19.135	32.214
818.712	18.101	30.474
830.656	17.08	28.754
842.274	16.072	27.057
853.553	15.08	25.388

Length [mm]	Width [‰ of L]	Height [‰ of L]
864.484	14.107	23.749
875.056	13.154	22.145
885.257	12.223	20.577
895.078	11.316	19.051
904.508	10.436	17.569
913.54	9.583	16.134
922.164	8.761	14.749
930.371	7.971	13.419
938.153	7.214	12.145
945.503	6.493	10.932
952.414	5.81	9.781
958.877	5.165	8.696
964.888	4.561	7.679
970.44	4	6.734
975.528	3.482	5.862
980.147	3.009	5.065
984.292	2.582	4.347
987.958	2.203	3.708
991.144	1.872	3.151
993.844	1.59	2.677
996.057	1.359	2.288
997.781	1.178	1.983
999.013	1.049	1.766
999.753	0.971	1.635
1000	0.945	1.591

Continue from previous table

Ringraziamenti

Desidero ora ringraziare tutti coloro i quali sono stati d'aiuto per la stesura di questo lavoro, che hanno fatto osservazioni, critiche e suggerimenti al fine di potermelo far sviluppare al meglio. A loro va tutta la mia gratitudine, anche se spetta a me la responsabilità di ogni errore contenuto in questa tesi.

Innanzitutto ringrazio il Professor Andrea Marion, Relatore, per la possibilità che mi ha dato di partecipare al programma Erasmus e per i consigli. Ringrazio poi il Dottor Costantino Manes per avermi seguito come supervisor presso la *University of Southampton*, per i preziosi suggerimenti datimi e per le svariate ore di confronto che mi ha concesso.

Hence, I want to thank Dr Toru Tsuzaki, head of the hydraulic laboratory at the University of Southampton, for his help in designing the experiment and Jasper De Bie, Ph.D. candidate, for helping me in understanding fish biology and for letting me participate on his research.

Un ringraziamento va anche agli amici che, all'estero, o dalla patria, mi hanno sostenuto, sopportato ed aiutato durante lo svolgimento del presente lavoro. A Luca per essere stato sempre presente quando tornavo a casa. A Giulia per essere partita allo sbaraglio. A Mirco, Arianna e Giacomo, perché gli unici ingegneri che all'estero durano sono ambientali, mentre quelli che tornano a casa e trovano lavoro sono meccanici. A Giuseppe, Fernando e Roberto che non mi hanno mai fatto mancare il sorriso nei nove mesi di Erasmus. A Silvia, Francesco B., Francesco G., Enrico e Leonardo per la fantastica esperienza universitaria affrontata assieme e per tutte le difficoltà che l'aver lavorato con loro mi ha fatto superare. Per lo stesso motivo voglio ringraziare anche Luca, con il quale lo studio è stato un gioco molto divertente.

Ringrazio dal più profondo Giorgia per avermi sempre fatto la telecronaca di

quanto succedesse a casa, come quasi a dire: “Tu di qui non te ne puoi andare”, Silvia per la lucidità insana con cui abbiamo affrontato l’università e siamo diventati amici, Giacomo per presentarsi sempre con nuove idee, o idiozie che dir si voglia, che spesso mi hanno ricordato che tutto si può fare e Massimo per la spensieratezza e per il muso che ha sempre tenuto e sempre terrà quando gli si parla di cose che non ha voglia di ascoltare, ricordandomi che ogni tanto è meglio dimenticare.

Un grazie va inoltre a tutti quelli che qui non ho citato, molto probabilmente perché non ho trovato le parole per descrivere il sentimento che ci lega.

Un ringraziamento speciale va a Sara che ha saputo restarmi vicina anche se sono stato io il primo a decidere di voler andarle lontano. Non credo che sarebbe stato lo stesso senza di lei.

Infine, un ringraziamento va alla mia famiglia che mi ha sostenuto, emotivamente ed economicamente, in particolar modo durante lo svolgimento di questa tesi. A loro ed a Sara, è dedicata questa tesi.

Bibliography

[1] I. H. Abbott and A. E. Von Doenhoff. *Theory of Wing Sections*. Dover Pubblications, Inc., 1958.

[2] M. M. Alam, M. Moriya, and H. Sakamoto. Aerodynamic characteristics of two side-by-side circular cylinders and application of wavelet analysis on the switching phenomenon. *Journal of Fluids and Structures*, 18:325–346, 2003a.

[3] B. Andersson, R. Andersson, H. Hakansson, M. Mortensen, R. Sudiyo, B. vanWachem, and L. Hellström. *Computational Fluid Dynamics for Engineers*. Cambridge University Press, 2012.

[4] ANSYS, Inc, Southpointe 275 Technology Drive Canonsburg, PA 15317. *ANSYS FLUENT Theory Guide*, November 2011.

[5] ANSYS, Inc, Southpointe 275 Technology Drive Canonsburg, PA 15317. *ANSYS FLUENT User's Guide*, November 2011.

[6] J. Blazek. *Computational Fluid Dynamicas: Principles and Applications*. Elsevier, 2005.

[7] Horst Bleckmann. *The Behaviour of Telost Fishes*. Springer US, 1986.

[8] Q. Bone and N. B. Marshall. *Biology of Fishes*. Blackie, 1982.

[9] Q. Bone, N. B. Marshall, and J.H.S. Balxter. *Biology of Fishes*. Blackie Academic and Professional, 1995.

[10] W. Cresswell. Flocking is an effective anti-predation strategy in redshanks, *Tringa totanus*. *Animal Behaviour*, 47:433–442, 1994.

[11] Peter A. Dewey, Daniel B. Quinn, Birgitt M. Boschitsch, and Alexander J. Smits. Propulsicve performance of unsteady tandem hydrofoils in a side-by-side configuration. *Physic of Fluids*, 26, 2014.

[12] J. Godin, L.J. Classon, and M.V. Abrahams. Group vigilance and shoal size in a small characin fish. *Behavior*, 104:245–254, 1988.

[13] C.K. Hemelrijk, D.A.P. Reid, H. Hildrenbrandt, and J.T. Padding. The increased efficiency of fish swimming in a school. *Fish and Fisheries*, 2014.

[14] E. Hori. Experiments on flow around a pair of parallel circular cylinders. *In: Proceedings of the Ninth Japan National COngress for Applied Mechanics*, Paper III-11:231–234, 1959.

[15] J. M. Jeschke and R. Tollrian. Prey swarming: which predators become confused and why? *Animal*, 74:387–393, 2007.

[16] W.P. Jones and B.E. Launder. The prediction of laminarization with a two-equation model of turbulence. *Int. J. Heat Mass Transfer*, 15:301–314, 1972.

[17] W.P. Jones and B.E. Launder. The calculation of low-reynolds-number phenomena with a two-equation model of turbulence. *I. Jou. Heat Mass Transfer*, 16:1119 – 1130, 1973.

[18] Jens Krause and Graeme. D. Ruxton. *Living in groups*. Oxford University Press, 2002.

[19] B.E. Launder and B.I. Sharma. Application of the energy-dissipation model of turbulence to the calculation of flow near a spinning disc. *Lett. Heat Mass Transfer*, 1:131–138, 1974.

[20] J.C. Liao. A review of fish swimming mechanics and behaviour in altered flows. *Philosophical Transactions of the Royal Society B*, 362:1973–1993, 2007.

[21] S. Murakami and A. Mochida. On turbulent vortex shedding flow past 2d square cylinder predicted by cdf. *Journal of Wind Engineering and Industrial Aerodynamics*, 54/55:191–211, 1995.

[22] B. L. Partridge and T. J. Pitcher. The sensory basis of fish school: Relative roles of lateral line and vision. *J. Comp Physiol. A*, 135:315–325, 1980.

[23] B.L. Partridge. The effect of school size on the structure and dynamics of minnow schools. *Anima Behaviour*, 28:68–&, 1980.

[24] B.L. Partridge and T.J. Pitcher. Evidence against a hydrodynamic function for fish schools. *Nature*, 279:418–419, 1979.

[25] S. B. Pope. *Turbulent Flows*. Cambridge University Press, 2000.

[26] D. B. Quinn, K.W. Moored, P. A. Dewey, and A. J. Smits. Unsteady propulsion near a solid boundary. *Journal of Fluid Mechanics*, 742:152–170, 2014.

[27] O. Reynolds. On the dynamical theory of incompressible viscous fluids and the determination of the criterion. *Philosophical Transactions of the Royal Society of London. A*, 186:123–164, 1895.

[28] D. Sumner. Two circular cylinders in cross-flow: A review. *Journal of Fluids and Structures*, 26:849–899, 2010.

[29] D.J. Tritton. *Physcal Fluid Dynamics*. Oxford University Press, 1988.

[30] D. Weish. Hydromechanics of fish schooling. *Nature*, 241:290 – 291, 1973.

[31] V. Yakhot and L.M. Smith. The renormalization group, the epsilon-expansion and derivation of turbulence models. *Journal of Scientific Computing*, 7:35 – 62, 1992.

[32] M.M. Zdravkivich and D.L. Pridden. Interference between two circular cylinders; series of unexpected discontinuities. *Journal of Industrial Aerodynamics*, 2:255–270, 1977.